



저작자표시-비영리-변경금지 2.0 대한민국

이용자는 아래의 조건을 따르는 경우에 한하여 자유롭게

- 이 저작물을 복제, 배포, 전송, 전시, 공연 및 방송할 수 있습니다.

다음과 같은 조건을 따라야 합니다:



저작자표시. 귀하는 원저작자를 표시하여야 합니다.



비영리. 귀하는 이 저작물을 영리 목적으로 이용할 수 없습니다.



변경금지. 귀하는 이 저작물을 개작, 변형 또는 가공할 수 없습니다.

- 귀하는, 이 저작물의 재이용이나 배포의 경우, 이 저작물에 적용된 이용허락조건을 명확하게 나타내어야 합니다.
- 저작권자로부터 별도의 허가를 받으면 이러한 조건들은 적용되지 않습니다.

저작권법에 따른 이용자의 권리는 위의 내용에 의하여 영향을 받지 않습니다.

이것은 [이용허락규약\(Legal Code\)](#)을 이해하기 쉽게 요약한 것입니다.

[Disclaimer](#)

공학박사 학위논문

**Pore Structures in Components of
Polymer Electrolyte Membrane Fuel Cells
and Water Electrolysis**

고분자 전해질 막 연료전지와 수전해
구성요소의 기공 구조 연구

2019 년 8 월

서울대학교 대학원
공과대학 화학생물공학부
에너지환경화학융합기술전공
박지은

Abstract

**Pore Structures in Components of
Polymer Electrolyte Membrane Fuel Cells
and Water Electrolysis**

Ji Eun Park

School of Chemical and Biological Engineering Chemical
Convergence for Energy & Environment
The Graduate School
Seoul National University

Hydrogen is attracting attention as an alternative energy source as it has high energy density and is environmentally friendly source without CO₂ emission. It is used as a fuel for fuel cells, generating electricity. Fuel cells are energy conversion devices that directly convert chemical energy to electrical energy using hydrogen and oxygen gases. Among various types of fuel cells, polymer electrolyte membrane fuel cells (PEMFCs) have widely developed due to its high efficiency and low operating temperature. In addition, hydrogen can be produced by water electrolysis. While alkaline water electrolysis has been widely used, polymer electrolyte membrane water electrolysis with proton-exchange membrane (PEM) or anion-exchange membrane (AEM) has been considered as promising water electrolysis owing to high efficiency and high purity hydrogen production.

The development of pore structure in components is crucial for improving performance of practical electrochemical devices such as fuel cell and water electrolysis. While the catalytic activity of electrocatalysts has been sharply

enhanced by extensive research, their practical performance has not captured the performance obtained in half-cell test. This is why the pore structure in components needs to be investigated to exhibit high practical performance by preparing the porous components that are suitable for electrocatalysts to participate in oxygen reduction reaction (ORR) or oxygen evolution reaction (OER).

Chapter 1 briefly introduces the fuel cells and water electrolysis. The features, components, and performance of fuel cell are introduced. Also, the types, features, performance, and recent literature of water electrolysis are addressed.

In chapter 2, porous flow field was applied in PEMFCs to improve the mass transport of reactants and products. Flow field is an important component that supplies reactants into catalyst layer and removes the generated water. Metal foam has been considered as porous flow field due to its structural characteristics. However, few studies on investigation of its microstructures have been reported. Various kinds of copper-foam were applied and examined to attain the optimal structure that exhibits high performance. The PEMFCs with optimized metal-foam showed 2-fold performance enhancement compared with that with conventional flow field, which is the highest performance reported to date despite operation with an ambient pressure. It is attributed to the internally generated pressure in copper-foam as well as enhanced mass transport.

In chapter 3, porous electrode with inverse-opal structure was proposed as anode in PEMWE to enhance the utilization of IrO_2 catalyst, thereby reducing the loading. In PEMWE, a high catalyst loading is used to exhibit high performance, leading to high PEMWE cost. To reduce catalyst loading, porous structure is applied in anode. Inverse-opal structure is a three-dimensionally ordered and interconnected porous structure. Due to its large surface area, inverse-opal membrane-electrode assembly (MEA) exhibited higher performance than conventional MEA.

Furthermore, inverse-opal MEA showed the highest mass activity as catalyst loading was ultra-low. This is because inverse-opal structure resulted in enhancement of catalyst utilization.

In chapter 4, the MEA parameters and operating conditions for AEMWE was optimized to achieve high performance. Unlike PEMWE consisting of standard proton exchange membrane (PEM) (Nafion), a few studies regarding AEMWE have been reported as standard anion exchange membrane (AEM) do not exist. Also, few studies investigating the MEA of AEMWE have been reported. Therefore, the development of highly efficient MEA in AEMWE is important for enhancing cell performance. The optimization results showed that the AEMWE performance exhibited the highest performance among other research reported in literature.

In chapter 5, graphitic carbon nitride-carbon nanofiber (g-CN-CNF) composite was applied as OER electrocatalyst for anode in AEMWE to form porous electrode. The use of carbon nanofiber resulted in preparation of porous electrode by enlarging secondary pores. g-CN-CNF catalyst is the composite mixing g-CN, which consists of N and C, and CNF. While n-doped carbon materials have been reported to have OER activity, it is the first research to apply carbeneous materials on practical AEMWE. g-CN-CNF exhibited high OER activity in half-cell test due to its high content of pyridinic nitrogen. Also, AEMWE with g-CN-CNF catalyst showed outstanding practical performance. This is owing to the formation of large secondary pores in electrode.

Keywords: Polymer Electrolyte Membrane Fuel Cells, Proton Exchange Membrane Water electrolysis, Anion Exchange Membrane Water Electrolysis, Porous structure

Student number: 2016-30224

Contents

Abstract	i
Contents	iv
List of Tables	vii
List of Figures	ix
Chapter 1. Introduction	1
1.1. General Introduction to Polymer Electrolyte Membrane Fuel Cells.....	1
1.2. General Introduction to Polymer Electrolyte Membrane Water Electrolysis.....	6
1.3. Aim of This Thesis.....	12
1.4. References	16
Chapter 2. Optimization of Copper-foam Micro-structures as Flow Field for Polymer Electrolyte Membrane Fuel Cells.....	22
2.1. Introduction	22
2.2. Experimental Section.....	24
2.3. Results and Discussion.....	28
2.4. Conclusions.....	56
2.5. References.....	57

Chapter 3. Ultra-Low Loading of IrO₂ with an Inverse-Opal Structure in a Proton Exchange Membrane Water Electrolysis.....63

3.1. Introduction.....	63
3.2. Experimental Section.....	67
3.3. Results and Discussion.....	70
3.4. Conclusions.....	97
3.5. References.....	98

Chapter 4. Development of Membrane-electrode Assembly for High-performance Anion Exchange Membrane Water Electrolysis.....103

4.1. Introduction.....	103
4.2. Experimental Section.....	107
4.3. Results and Discussion.....	110
4.4. Conclusions.....	134
4.5. References.....	135

Chapter 5. Graphitic carbon nitride-carbon nanofiber as oxygen evolution reaction catalyst in anion-exchange membrane water electrolyzer.....139

5.1. Introduction.....	139
------------------------	-----

5.2. Experimental Section.....	142
5.3. Results and Discussion.....	145
5.4. Conclusions.....	168
5.5. References.....	169
국문 초록 (Abstract in Korean)	174
List of Publications (SCI)	177

List of Tables

Chaper 1

-

Chaper 2

Table 2.1. Specific resistance ($m\Omega\cdot cm$) and contact angle ($^{\circ}$) of copper-foam and conventional flow field.....29

Table 2.2. Copper-foam parameters.....31

Table 2.3. Porosity of compressed copper-foams (250 μm) and pressure generated in copper-foam flow field MEAs.....34

Table 2.4. Operating condition of the references shown in the performance comparison (Fig. 2.11b).....47

Chaper 3

Table 3.1 The summary of catalyst loading, cell performance, mass activity of some reported IrO_2 catalyst in PEMWE.....96

Chaper 4

Table 4.1 Porosity of MEA with different ionomer contents measured by using mercury porosimetry.....121

Table 4.2 The summary of materials, components, cell operations, and performance of AEMWE reported in literature.....131

Chaper 5

Table 5.1 Summary of nitrogen properties, binding energy, content of g-CN-CNF-

T materials.....	155
Table 5.2 Summary of nitrogen properties, binding energy, content of g-CN-CNF- N wt materials.....	159

List of Figures

Chaper 1

Figure 1.1 Schematic diagram of polymer electrolyte membrane fuel cells (PEMFCs).....	3
Figure 1.2 Typical I-V curve of polymer electrolyte membrane fuel cells (PEMFCs).....	4
Figure 1.3 Schematic diagram of proton exchange membrane water electrolyzer. Adapted from Ref 30 (<i>J. Power Soc.</i> 2017, 366 , 33-35).....	8
Figure 1.4 Schematic diagram of anion exchange membrane water electrolyzer.....	9
Figure 1.5 The comparison in performance of three water electrolysis (alkaline water electrolysis, PEMWE, and AEMWE). Adapted from Ref 37 (<i>Meeting Abstracts</i> 2015, MA2015-01 , 1489).....	11
Figure 1.6 Comparison of catalytic activity obtained at liquid electrolyte and practical device of various platinum-based catalysts. Adapted from Ref 54(<i>Science</i> 354 , 1378-1379 (2016)).....	13
Figure 1.7 Brief summary of this thesis.....	14

Chaper 2

Figure 2.1 Schematic diagrams of the layer structure of the copper-foam flow field MEA and conventional MEA.....	25
Figure 2.2 Photographs of six different copper-foams (Cu 1-6).....	30
Figure 2.3. Effect of copper foam thickness on the cell performance and microstructure. (a) Polarization and power density curves of three MEAs with different thicknesses (1 mm, 500 μm , and 200 μm) of copper foam (Cu 1). (b)	

Porosity (red data) and pressure generated (blue data) in copper foams with different thicknesses.....	33
Figure 2.4. Microstructural characterization of the copper-foams. SEM images of samples Cu 1–4 (a–d) before and (e–h) after compression. (i) Schematic diagrams of the corresponding area densities of samples Cu 1–4.....	36
Figure 2.5 Effect of copper-foam area density on the cell performance. (a) Polarization and power density curves for four MEAs with different area densities of copper-foam (Cu 1, 2, 3, and 4). (b) Ohmic resistance ($m\Omega$) obtained at 0.6 V using EIS (red data) and the sum of charge transfer and mass transport resistance ($m\Omega$) obtained at 0.4 V using EIS (blue data) for the copper-foams (Cu 1, 2, 3, and 4).....	37
Figure 2.6. (a) Equivalent circuit model and Nyquist plots of copper-foam MEAs with the different area densities (Cu 1-4). (b) 0.8 V, (c) 0.6 V, (d) 0.4 V.....	38
Figure 2.7 SEM images of (a-c) pristine Cu 3, 5, and 6 and (d-f) compressed Cu 3, 5, and 6. The scale bar is 250 μm	40
Figure 2.8 Effect of copper-foam pore size on the cell performance. (a) Polarization and power density curves of the three MEAs with different copper-foam pore sizes (Cu 3, 5, and 6). (b) Charge transfer resistance ($m\Omega$) obtained at 0.8 V using EIS (red data) and the sum of charge transfer and mass transport resistance ($m\Omega$) obtained at 2.0 $\text{A}\cdot\text{cm}^{-2}$ using EIS (blue data) for copper-foams (Cu 3, 5, and 6).....	41
Figure 2.9 Nyquist plots of copper-foam MEAs with the different pore sizes (Cu 3, 5, 6). (a) 0.8 V, (b) 0.6 V, (c) 0.4 V, (d) 2.0 $\text{A}\cdot\text{cm}^{-2}$	42
Figure 2.10 Comparison of the performance of copper-foam and conventional flow field MEAs. (a) Voltage as a function of current density. (b) Cyclic voltammetry curves. (c–e) Nyquist plots obtained at (c) 0.8 V, (d) 0.6 V, and (e) 0.4 V.....	43
Figure 2.11 Performance of optimized copper-foam flow field MEA. (a) Voltage as a function of current density of optimized copper-foam flow field MEA. (b) The	

comparison of current density at 0.6 V and maximum power density exhibited in this study and those reported in literature ^{11,24-28} (Solid: ambient pressure, Open: back pressure).....	46
Figure 2.12 Stability test of copper-foam flow field MEA for 8 h.....	48
Figure 2.13 Comparison of the performance of three different flow fields (copper foam, micro flow field, and conventional flow field). (a) Photographs of the three flow fields. (b) Voltage as a function of current density at ambient pressure. (c) Voltage as a function of current density at ambient pressure (copper foam MEA), and with a back pressure of 1.8 bar (micro flow field MEA and conventional MEA).....	52
Figure 2.14 CO poisoning test of copper-foam flow field MEA and conventional flow field MEA. (a) Schematic diagram of CO poisoning test and (b) normalized voltage profile of copper-foam flow field MEA and conventional flow field MEA during CO poisoning test.....	54
Figure 2.15 Normalized voltage profile of copper-foam MEA (ambient pressure) and conventional MEA (1.8 bar back pressure).....	56

Chaper 3

Figure 3.1 Schematic diagram of the single-cell of inverse-opal MEA.....	66
Figure 3.2 Photographs of each step in the decal-transfer method for inverse-opal MEA.....	71
Figure 3.3 FE-SEM images of each step in the decal-transfer method: (a) self-assembled PS beads as template, (b) infiltration of IrO ₂ by using pulse electrodeposition, and (c) inverse-opal electrode. The scale bar is 1 μm.....	72
Figure 3.4 Polarization curves of conventional MEA before and after nitric acid treatment.....	73

Figure 3.5 FE-SEM images of inverse-opal electrode obtained with different current of (a) 5, (b) 10, (c), 20, and (d) 30 mA. The scale bar is 5 μm and 1 μm , respectively.....	75
Figure 3.6 Voltage curves of electrodes obtained with different current of (a) 5, (b) 10, (c), 20, and (d) 30 mA.....	76
Figure 3.7 FE-SEM images of inverse-opal electrode with variations in the total number of cycles (a) 80 k, (b) 120 k, (c) 140 k, and (d) 160 k cycles. The applied current is 10 mA. The scale bar is 5 μm	77
Figure 3.8. FE-SEM images of several inverse-opal electrodes obtained with the optimal ED conditions. The scale bar is 1 μm	79
Figure 3.9 TEM images of inverse-opal electrode.....	80
Figure 3.10 XRD patterns of FTO, Ni-FTO, and inverse-opal electrode.....	82
Figure 3.11 Ir 4f XPS spectra of IrO_2 inverse-opal electrode.....	83
Figure 3.12 Cyclic voltammetry of inverse-opal MEA with different total cycles (80k, 120k, 140k, and 160k cycles).....	84
Figure 3.13 (a) Polarisation curves of inverse-opal MEAs with differences in the total number of cycles (80 k, 120 k, 140 k, and 160 k cycles).....	86
Figure 3.14 The performance changes of inverse-opal MEAs as a function of catalyst loading.....	87
Figure 3.15 (a) PEMWE performance, (b) Nyquist plot at 1.6 V, (c) cyclic voltammetry, and (d) measured amount of generated hydrogen in the inverse-opal MEA and conventional MEA. The catalyst loading is $0.02 \text{ mg}\cdot\text{cm}^{-2}$	88
Figure 3.16 Stability test results of the inverse-opal MEA and conventional MEA in the (a) low-voltage (1.6 V) and (b) high-voltage (1.9 V) regions over a time period spanning 1200 s.....	90
Figure 3.17 PEMWE performance (solid) and estimated performance by measured amount of generated hydrogen (open) of inverse-opal MEA and conventional MEA. The catalyst loading was $0.02 \text{ mg}\cdot\text{cm}^{-2}$	92

Figure 3.18. FE-SEM images of (a-c) inverse-opal electrode and (d-f) conventional electrode: (a, d) cross-sectional view, and top view (b, e) before stability test and (c, f) after stability test.....	93
Figure 3.19 Comparison of (a) cell performances (current density at 1.6 V) and (b) mass activities at 1.6 V achieved in the study and those reported in extant studies. 2,4-7,39,40	95

Chaper 4

Figure 4.1 Schematic diagram of single-cell components in AEMWE.....	108
Figure 4.2 (a) Polarization curves and (b) Nyquist plots for AEMWE single cells with different fabrication processes: CCS without and with hot-pressing, and CCM at 50 °C. Nyquist plots were evaluated at 1.9 V. The feed condition was 1.0 KOH solution in both electrodes with flow rate of 1 ml·min ⁻¹	111
Figure 4.3 Polarization curves of AEMWEs prepared with different hot pressing conditions (no, 30, 50, 70, and 90 °C) of CCS method.....	112
Figure 4.4 Polarization curves of AEMWE single cells with different fabrication processes: CCS without and with hot-pressing, and CCM.....	113
Figure 4.5 Photographs of thicknesses of two MEAs with different fabrication methods: (a) CCM and (b) CCS.....	115
Figure 4.6 (a) Polarization curves for AEMWEs operated with different reactant feed methods (1–4), and (b) cell performance of AEMWEs with different reactant flow rates (1 M KOH) fed into both sides of electrode (1, 2.5, 5, and 10 ml·min ⁻¹) at 50 °C.....	116
Figure 4.7 (a) Polarization curves and (b) Nyquist plots for AEMWEs operated at different cell temperatures (50, 60, and 70 °C). Nyquist plots were evaluated at constant voltage of 1.9 V. The feed condition was 1.0 KOH solution in both electrodes with flow rate of 2.5 ml·min ⁻¹	119

Figure 4.8. (a) Polarization curves and (b) Nyquist plots for AEMWEs with different ionomer contents (10, 20, and 30 wt. %) at 50 °C, and (c) FE-SEM images of MEAs fabricated using different ionomer contents. The feed condition was 1.0 KOH solution in both electrodes with flow rate of 1 ml·min ⁻¹	120
Figure 4.9 Total resistance with different (a) Ti-GDLs (The C-GDL used was 270 μm) and (b) C-GDLs. (The Ti-GDL used was 250 μm) in N ₂ /N ₂ atmosphere.....	123
Figure 4.10 Polarization curves for single cells with different thickness of (a) Ti-GDLs and (b) C-GDLs at 50 °C. The feed condition was 1.0 KOH solution in both electrodes with flow rate of 1 ml·min ⁻¹	125
Figure 4.11 (a) Equivalent circuit model and Nyquist plots of AEMWEs with different (b) Ti-GDLs and (c) C-GDLs.....	126
Figure 4.12 Polarization curves for AEMWEs with different IrO ₂ catalyst loadings (1.0, 2.0, 4.0, and 6.0 mg·cm ⁻²) in anode at 50 °C. Cathode catalyst loading was 40 wt% with 0.4 mg·cm ⁻² . The feed condition was 1.0 KOH solution in both electrodes with flow rate of 1 ml·min ⁻¹	127
Figure 4.13 SEM cross section images of MEAs with different anode catalyst loadings of (a) 1 (b) 2 (c) 4 and (d) 6 mg·cm ⁻² . The scale bar represents 5 μm....	129
Figure 4.14 (a) Polarization curves for AEMWEs with optimized MEA fabrication method, operating conditions, and MEA parameters at 70 °C. The feed condition was 1.0 KOH solution in both electrodes with flow rate of 2.5 ml·min ⁻¹ . (b) Comparison of cell performance achieved in this study and those reported in literature. ^{6-11,13,21}	130
Figure 4.15 Comparison of cell performance in AEMWE and PEMWE with same MEA parameters and operating conditions.....	133

Chaper 5

Figure 5.1 (a) Schematic diagram showing the preparation of the g-CN-CNF catalyst.....	146
Figure 5.2 (a-b) SEM images, (c) FT-IR spectra, and (d) TGA spectra of the synthesized g-CN.....	147
Figure 5.3 (a) nitrogen adsorption isotherms and (b) pore size distribution of g-CN, g-CN-CNF-800, and CNF.....	148
Figure 5.4 (a) XRD patterns of g-CN, g-CN-CNF-T and CNF materials. (b) Raman spectra of g-CN-CNF-T and CNF materials. N 1s XPS spectra of (c) g-CN-CNF-noHT, (d) g-CN-CNF-700, (e) g-CN-CNF-800, and (f) g-CN-CNF-900.....	149
Figure 5.5 (a,b) SEM images, (c) TEM image, and (d–g) EDX elemental mapping of g-CN-CNF-800 electrocatalyst.....	151
Figure 5.6 XPS survey spectra of g-CN-CNF-T materials.....	152
Figure 5.7 C 1s XPS spectra of g-CN-CNF-T materials ((a): g-CN-CNF-no, (b): g-CN-CNF-700, (c) g-CN-CNF-800, and (d) g-CN-CNF-900).....	153
Figure 5.8 XPS survey spectra of g-CN-CNF-Nwt materials.....	156
Figure 5.9 XPS spectra of g-CN-CNF-Nwt materials: (a) C 1s and (b) N 1s of g-CN-CNF-30wt, (c) C 1s and (d) N 1s of g-CN-CNF-50wt, (e) C 1s and (f) N 1s of g-CN-CNF-70wt.....	157
Figure 5.10 (a) Nitrogen adsorption isotherms and (b) pore size distributions of g-CN-CNF-N wt materials.....	160
Figure 5.11 (a) Linear sweep voltammogram curves of (a) g-CN-CNF-T materials and (b) g-CN-CNF-Nwt materials for OER at a scanning rate of 10 mV/s with iR correction.....	161
Figure 5.12 (a) Schematic diagram of AEMWE single cell with g-CN-CNF-800 as the anode catalyst. (b) Polarization curves obtained for AEMWE with different anode catalyst loadings. (c) Cell performance of AEMWE with g-CN-CNF-800 and commercial IrO ₂ . (d) The comparison of cell performances (current densities at 1.9 V) reported in literature and in this work (full symbols: non-noble metals as	

OER catalysts, open symbols: carbon-based material as OER catalyst).....	163
Figure 5.13 Nyquist plots of AEMWE with g-CN-CNF-800 and IrO ₂ electro-catalyst obtained at 1.9 V.....	165
Figure 5.14 Pore size distributions of catalyst layers with g-CN-CNF-800 and IrO ₂ measured by mercury porosimetry.....	166
Figure 5.15 SEM images of MEA of AEMFCs: top view of catalyst layer of (a) g-CN-CNF-800 and (b) Pt/C. Cross-section view of MEA with (c) g-CN-CNF-800 and (d) Pt/C.....	167

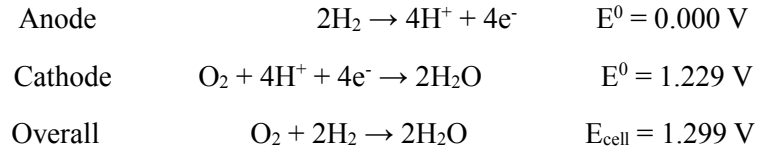
Chapter 1. Introduction

Numerous studies have been conducted on the development of hydrogen energy due to the global warming and the limited reserves of fossil fuels. Hydrogen exhibits the highest energy density and is an environmentally friendly source.¹⁻³ It is used as a fuel in fuel cells, generating electricity. Fuel cells are energy conversion devices converting chemical energy to electricity. Hydrogen can be produced by water electrolysis splitting water.

1.1. General Introduction to Polymer Electrolyte Membrane Fuel Cells

Fuel cells are power sources that directly convert chemical energy to electrical energy using hydrogen and oxygen gases. Fuel cells are classified according to the electrolyte: phosphoric fuel cells (PAFCs), solid oxide fuel cells (SOFCs), polymer electrolyte membrane fuel cells (PEMFCs), and anion exchange membrane fuel cells (AEMFCs). PEMFCs, which are the fuel cells with polymer electrolyte membrane (PEM), has been widely developed and commercialized due to their advantages such as high power density, low operating temperature and zero emission.^{4,5}

PEMFCs are operated as following electrochemical reactions. At anode, hydrogen is oxidized, generating the protons and electrons. The generated protons migrate into cathode through PEM. The electrons are moved to cathode through external circuit. At cathode, the oxygen is reduced with the protons and electrons, leading to the formation of water. The formed water is removed from catalyst layer to flow field.^{5,6}



Single cell of PEMFCs consists of membrane, electrodes (anode and cathode), gas diffusion layer (GDL), and flow fields in bipolar plates, as illustrated in Figure 1.1. Reactants (hydrogen and oxygen) are supplied through flow fields. They are transferred from the flow fields to the electrode via the GDL. Also, the generated water in cathode is transferred from cathode to flow field through the GDL.

While PEMFCs have many advantages, it has still drawbacks to be solved such as its low performance, poor durability and high cost. To improve these drawbacks, the performance enhancement is currently regarded as the major challenge.⁷⁻¹³ For the high performance of the PEMFCs, it is important to have a high voltage at the high current density.

To enhance cell performance, three overpotentials need to be reduced, i.e. activation, ohmic, and concentration overpotentials. While the theoretical voltage of PEMFCs is 1.23 V, the actual operating voltage decreases due to these three overpotentials, as shown in Figure 1.2. Firstly, the activation overpotential, which is dominant in low current density region, is associated with the catalyst kinetics, which is affected by the Gibbs free energy of the catalyst, the operation temperature, and reactant concentration.^{14,15} Also, the ohmic overpotential is related to electron and ion transport.^{16,17} Finally, the concentration overpotential occurs due to the mass transport of reactants and products.¹⁸ When operating under high current densities, the concentration overpotential dominates cell performance

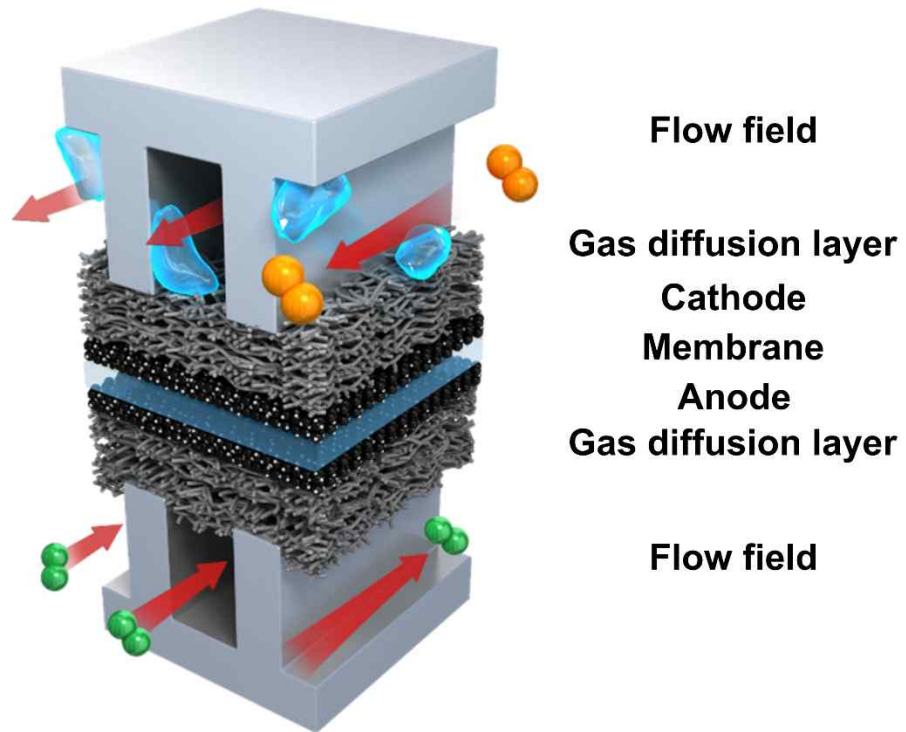


Figure 1.1 Schematic diagram of polymer electrolyte membrane fuel cells (PEMFCs).

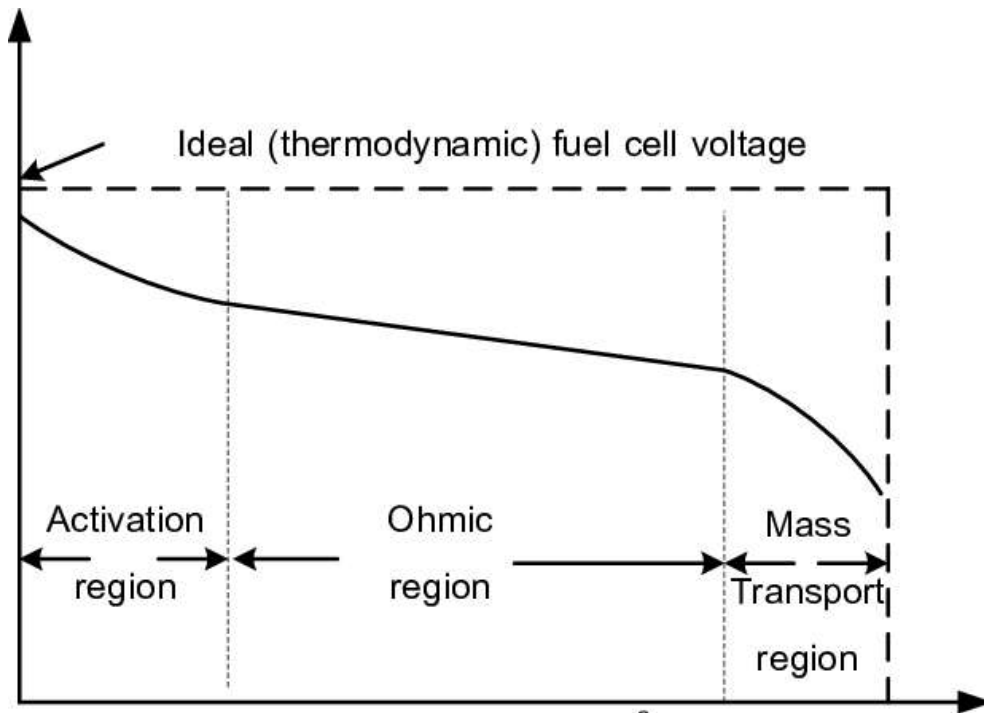


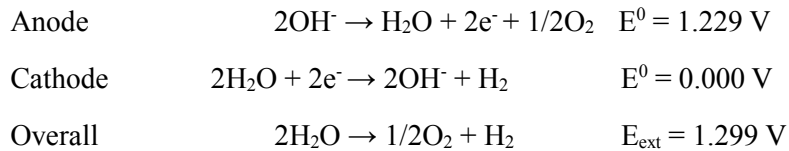
Figure 1.2 Typical I-V curve of polymer electrolyte membrane fuel cells (PEMFCs).

and inhibits achieving high performance PEMFCs. The improvement of mass transport can overcome the concentration overvoltage.

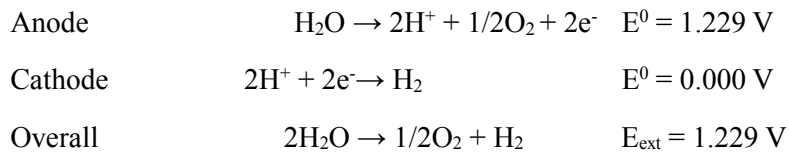
1.2. General Introduction to Polymer Electrolyte Membrane Water Electrolysis

Hydrogen can be produced renewably using a variety of methods such as steam reforming,^{19,20} photoproduction,²¹ and water electrolysis.^{22,23} Among these methods, water electrolysis has attracted much attention because it leads to high efficiency and the high-purity hydrogen production.^{22,23} When the electricity is applied to water electrolysis, water is splitted into oxygen (anode) and hydrogen (cathode) gases using the following chemical reaction. Depending on the types of electrolyte, i.e. alkaline and acidic, the water electrolysis is operated using a different mechanism.

<Alkaline>



<Acidic>



Water electrolysis can be classified according to the type of electrolyte used in the device: alkaline water electrolysis and polymer electrolyte membrane water electrolysis such as proton exchange membrane water electrolysis (PEMWE) and anion exchange membrane water electrosis (AEMWE). Two main water electrolysis, i.e. alkaline water electrolysis and PEMWE are currently used.

AEMWE have also been developed as candidate to improve the disadvantages of two major water electrolysis methods.^{24,25}

Alkaline water electrolysis corresponds to water electrolysis with a liquid alkaline electrolyte, which has long been commercialized.^{26,27} In alkaline water electrolysis, non-noble metals (Co, Cu, and Ni) were used as oxygen evolution reaction (OER) catalysts, thereby reducing the cost of water electrolysis. Additionally, it exhibits advantages of simplicity and safety. However, the use of liquid electrolyte can lead to leakage and sensitivity to CO₂, resulting in poor stability.²⁸

PEMWE was developed in order to overcome the disadvantages of alkaline water electrolysis. Specifically, it is the water electrolysis wherein a polymer electrolyte membrane is used as an electrolyte, as shown in Figure 1.3.²⁹ It is composed of a membrane with a thickness in the range of 20 – 100 μm, resulting in low ohmic resistance and a high performance.^{30,31} Additionally, it generates hydrogen with high-purity owing to the use of the solid membrane.³² Nevertheless, the commercialization of PEMWE is limited due to the high cost of catalyst.³³ As the PEMWE is operated in acidic media, novel metal catalysts including iridium- and ruthenium-based materials that exhibit activity for OER are commercially used as catalysts in the anode. Thus, the catalyst loading needs to be reduced to decrease the PEMWE cost.

AEMWE, that is, water electrolysis using an anion-exchange membrane (AEM), has been developed as an alternative to improve the drawbacks of alkaline water electrolysis and PEMWE in recent years.^{34,35} (Figure 1.4) AEMWE is performed in alkaline medium using non-platinum group metal (PGM) catalysts such as Ni-, Co-, and Cu-based materials as the OER catalyst, leading to cost reductions. Furthermore, like PEMWE, AEMWE produces high-purity hydrogen due to the presence of solid electrolyte. However, AEMWE shows lower

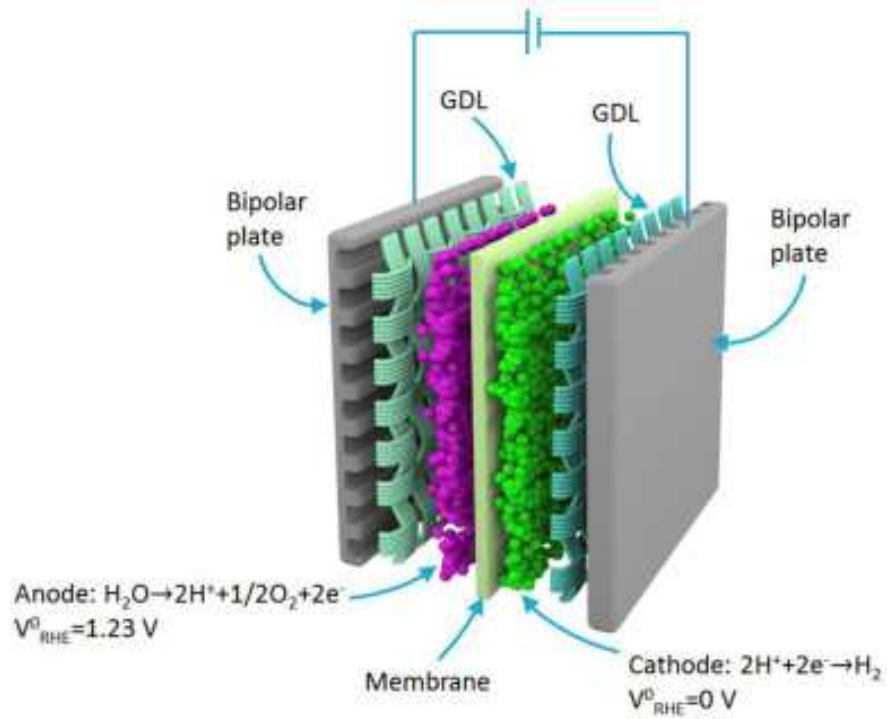


Figure 1.3 Schematic diagram of proton exchange membrane water electrolyzer.
 Adapted from Ref 30 (*J. Power Soc.* 2017, **366**, 33-35)

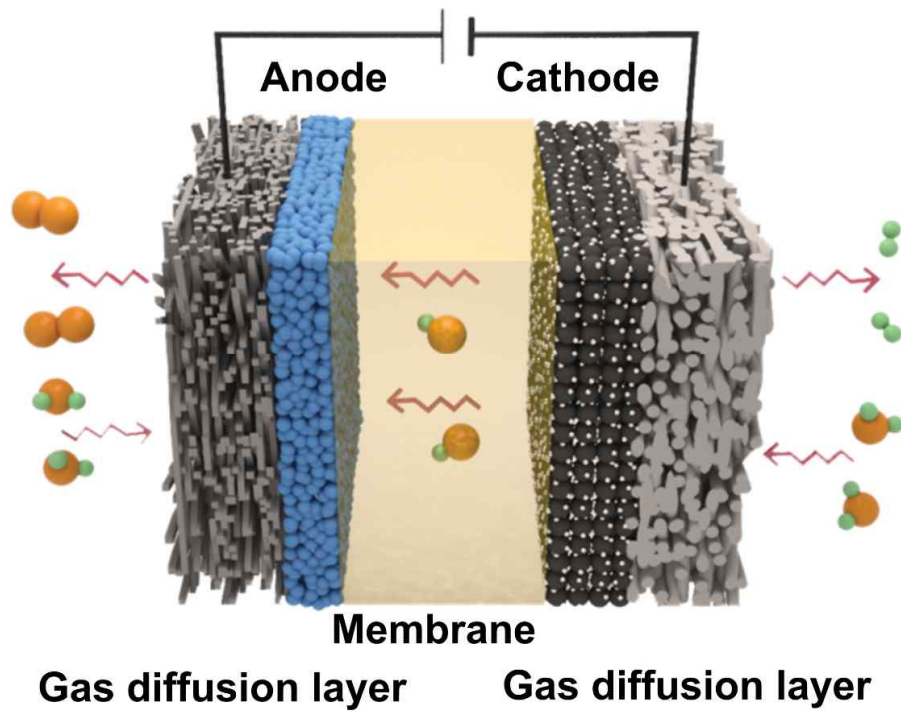


Figure 1.4 Schematic diagram of anion exchange membrane water electrolyzer.

performance and durability compared to other water electrolysis methods. Also, few studies investigating AEM and anion-exchange ionomers as well as the membrane-electrode assembly (MEA) of AEMWE have been reported. Therefore, the development of highly efficient MEA in AEMWE is important for enhancing cell performance.

Figure 1.5 presents the comparison in performance of three water electrolysis mentioned above.³⁶ Alkaline water electrolysis shows the lowest performance due to the presence of liquid electrolyte, leading to large ohmic resistance. On the other hand, PEMWE exhibits the highest performance among the developed water electrolysis. This is because the Nafion membrane, which is employed as electrolyte, has been widely commercialized and exhibits high conductivity of protons and good stability. Also, the use of noble catalyst such as Ir, Ru, Pt-based catalyst leads to high cell performance. Despite its high performance, high cost of these materials has been still problems to be solved. Finally, the performance of AEMWE is higher than that of alkaline water electrolysis and lower than that of PEMWE. Although the membrane is also used in AEMWE, the anion exchange membrane, which is under development, still shows poor ionic conductivity and stability. Thus, the AEMWE exhibits lower performance compared to PEMWE. Further development of anion exchange membrane can be expected to enhance performance of AEMWE.

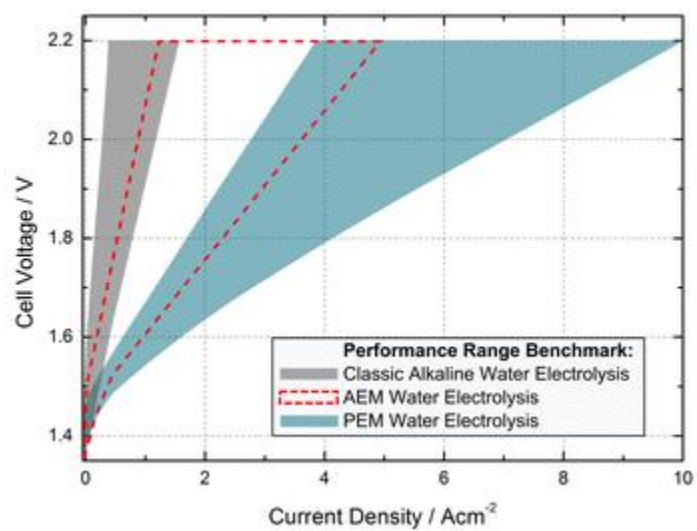


Figure 1.5 The comparison in performance of three water electrolysis (alkaline water electrolysis, PEMWE, and AEMWE). Adapted from Ref 37 (*Meeting Abstracts* 2015, MA2015-01, 1489)

1.3. Aim of this thesis

All electrochemical devices mentioned above are operated through oxygen electrocatalysis including ORR and OER. ORR plays a key role in determining the performance of fuel cells.¹⁰⁻¹² By contrast, the oxygen evolution reaction (OER) is the core process in water electrolyzers.^{30,31} The kinetics of oxygen electrocatalysis are sluggish, leading to low catalytic activity and thereby low performance of practical devices. Therefore, research on oxygen electrocatalyst has been widely developed.³⁷⁻⁴⁰

Figure 1.6 presents the comparison of ORR catalytic activity obtained in half-cell test and full-cell test (fuel cells) reported in literature.⁴¹ While the catalytic activity of ORR electrocatalysts has been sharply enhanced, their real fuel cell (full cell) performance has not captured the performance obtained in half-cell test. In addition to fuel cells, the water electrolysis exhibits the same phenomena. Few studies on practical application of OER or bifunctional catalyst have been reported although various research on these catalysts has been developed. These phenomena are ascribed to the insufficient investigation of membrane-electrode assembly in fuel cell and water electrolysis.

The development of pore structure in components, i.e. catalyst, catalyst layer, gas diffusion layer, and flow field, is crucial for improving the performance of practical electrochemical devices. For example, for fuel cells, the mass transport of reactant and product affects largely the cell performance.⁴²⁻⁴³ The pore structure in flow field needs to be examined to improve the mass transport, leading to the enhanced cell performance.⁴⁴ In case of water electrolysis, the performance can be increased by enhancing the utilization of catalyst or improving the mass transport.⁴⁵⁻⁴⁶ The introduction of pore structure in catalyst layer offers the increased surface area and pathway of reactant and product.⁴⁷⁻⁴⁸

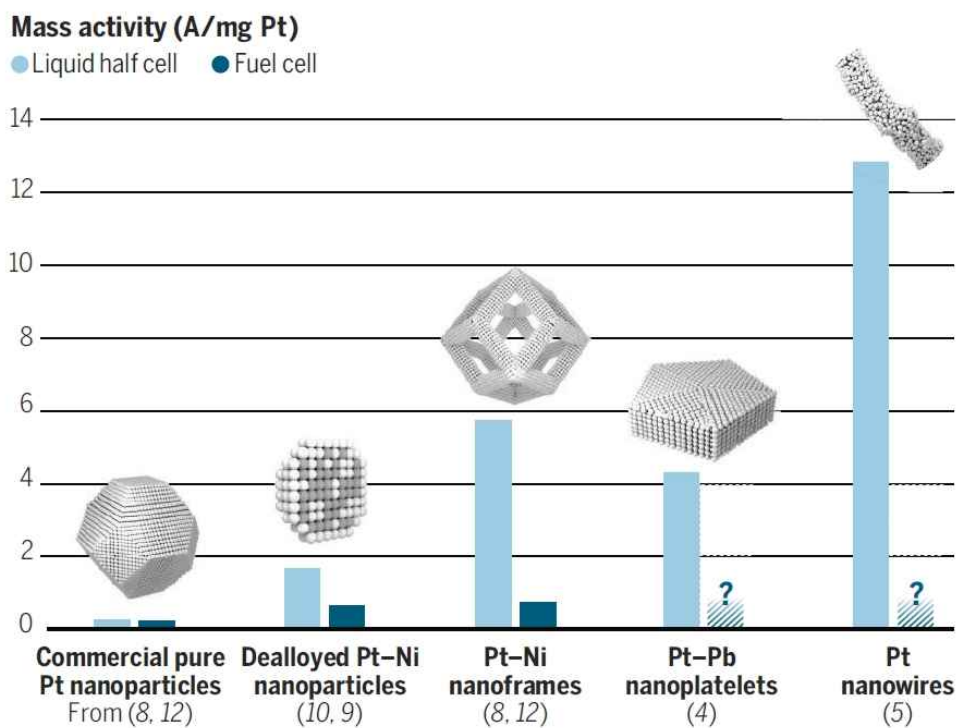


Figure 1.6 Comparison of ORR catalytic activity obtained at liquid electrolyte and practical device of various platinum-based catalysts. Adapted from Ref 54 (*Science* 2016, **354**, 1378-1379)

The main theme of this thesis is to investigate the effect of pore structure on components of PEMFCs, PEMWE and AEMWE, as presented in Figure 1.7. To achieve high fuel cell performance, the microstructure of metal-foam as flow field are investigated. Also, the porous electrode with interconnected and ordered macropores is prepared as anode in polymer-exchange membrane water electrolysis to enhance the utilization of catalyst. In addition, the graphitic carbon nitride-carbon nanofiber catalyst is synthesized as OER catalyst, and applied in anion-exchange membrane water electrolysis. When it is prepared in electrode, larger secondary pores resulted in the enhanced mass transport and ionic transport.

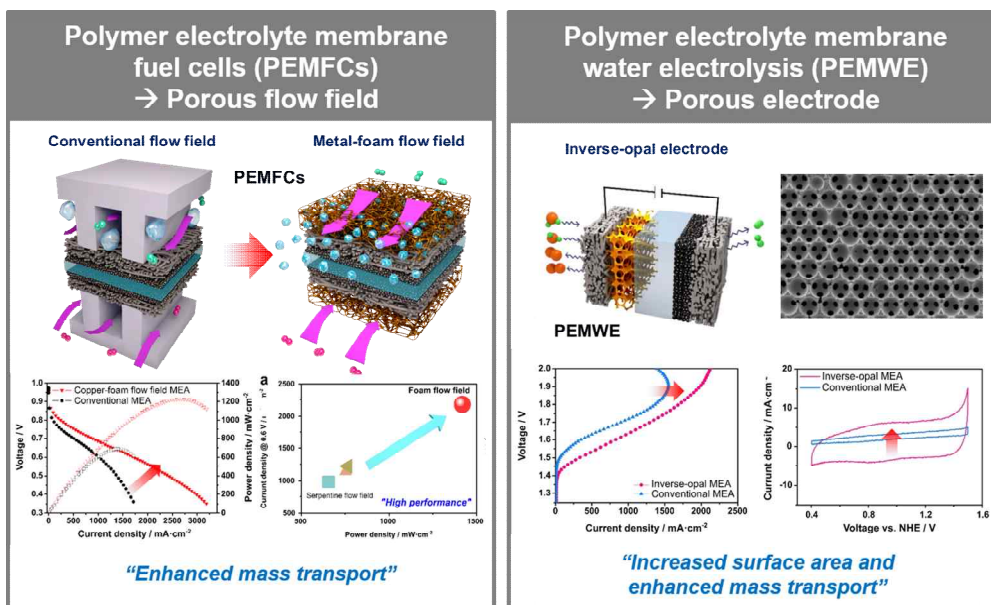


Figure 1.7 Brief summary of this thesis

1.3. References

1. S. Dutta, A review on production, storage of hydrogen and its utilization as an energy resource, *J. Ind. Eng. Chem.* 2014, **20**, 1148-1156.
2. J. A. Turner, A realizable renewable energy future, *Science* 1999, **285**, 687-689.
3. J. A. Turner, Sustainable hydrogen production, *Science* 2004, **305**, 972-974.
4. Y. Wang, K. S. Chen, J. Mishler, S. C. Cho, X. C. Adroher, A review of polymer electrolyte membrane fuel cells: Technology, applications, and needs on fundamental research, *Appl. Energy* 2011, **88**, 981-1007.
5. H. Zhang, P. K. Shen, Recent development of polymer electrolyte membranes for fuel cells, *Chem. Rev.* 2012, **112**, 2780-2832.
6. S. Litster, G. McLean, PEM fuel cell electrodes, *J. Power Soc.* 2004, **130**, 61-76.
7. D. E. Curtin, R. D. Lousenberg, T. J. Henry, P. C. Tangeman and M. E. Tisack, Advanced materials for improved PEMFC performance and life, *J. Power Soc.* 2004, **131**, 41-48.
8. N. Rajalakshmi, H. Ryu, M. M. Shaijumon and S. Ramaprabhu, Performance of polymer electrolyte membrane fuel cells with carbon nanotubes as oxygen reduction catalyst support material, *J. Power Soc.* 2005, **140**, 250-257.
9. L. Xiong and A. Manthiram, High performance membrane-electrode assemblies with ultra-low Pt loading for proton exchange membrane fuel cells, *Electrochim. Acta*, 2005, **50**, 3200-3204.
10. M. Michel, A. Taylor, R. Sekol, P. Podsiadlo, P. Ho, N. Kotov and L. Thompson, High-performance nanostructured membrane electrode

- assemblies for fuel cells made by layer-by-layer assembly of carbon nanocolloids, *Adv. Mater.*, 2007, **19**, 3859-3864.
11. O. H. Kim, Y. H. Cho, T. Y. Jeon, J. W. Kim, Y. H. Cho and Y. E. Sung, Realization of both high-performance and enhanced durability of fuel cells: Pt-exoskeleton structure electrocatalysts, *ACS applied materials & interfaces*, 2015, **7**, 14053-14063.
 12. S. M. Kim, C.-Y. Ahn, Y.-H. Cho, S. Kim, W. Hwang, S. Jang, S. Shin, G. Lee, Y.-E. Sung and M. Choi, High-performance fuel cell with stretched catalyst-coated membrane: one-step formation of cracked electrode, *Scientific Reports*, 2016, **6**, 26503.
 13. A. Kongkanand, N. P. Subramanian, Y. Yu, Z. Liu, H. Igarashi and D. A. Muller, Achieving high-power PEM fuel cell performance with an ultralow-Pt-content core-shell catalyst, *ACS Catalysis*, 2016, **6**, 1578-1583.
 14. Ryan P. O'Hayre, Suk-won Cha, Whitney G. Colella and F. B. Prinz, *Fuel Cell Fundamentals*, Wiley, New York, 2008.
 15. M. V. Williams, H. R. Kunz, J. M. Fenton, Analysis of polarization curves to evaluate polarization sources in hydrogen/air PEM fuel cells, *J. Electrochem. Soc.*, 2005, **152**, A635-A644.
 16. T. Mennola, M. Mikkola, M. Noponen, T. Hottinen and P. Lund, Measurement of ohmic voltage losses in individual cells of a PEMFC stack, *J. Power Sources*, 2002, **112**, 261-272.
 17. J. M. Sierra, S. J. Pathiyamattom and S. Gamboa, Study of activation losses and ohmic resistance in a PEM fuel cell using computational fluid dynamics, *ECS Transactions*, 2009, **20**, 395-405.
 18. O.-H. Kim, Y.-H. Cho, S. H. Kang, H.-Y. Park, M. Kim, J. W. Lim, D. Y. Chung, M. J. Lee, H. Choe, Y.-E. Sung, Ordered macroporous

platinum electrode and enhanced mass transfer in fuel cells using inverse opal structure, *Nature Commun.*, 2013, **4**, 2473.

19. A. Haryanto, S. Fernando, N. Murali, S. Adhikari, Current status of hydrogen production techniques by steam reforming of ethanol: A review, *Energy & Fuels* 2005, **19**, 2098-2106.
20. J. Dufour, D. P. Serrano, J. L. Gálvez, J. Moreno, A. González, Hydrogen production from fossil fuels: Life cycle assessment of technologies with low greenhouse gas emissions, *Energy & Fuels* 2011, **25**, 2194-2202.
21. D. I. Arnon, M. Losada, M. Nozaki, K. Tagawa, Photoproduction of hydrogen, photofixation of nitrogen and a unified concept of photosynthesis, *Nature* 1961, **190**, 601.
22. K. Zeng, D. Zhang, Recent progress in alkaline water electrolysis for hydrogen production and applications, *Prog. Energy Combust. Sci.* 2010, **36**, 307-326.
23. C. Lamy, From hydrogen production by water electrolysis to its utilization in a PEM fuel cell or in a SO fuel cell: Some considerations on the energy efficiencies, *Int. J. Hydrogen Energy* 2016, **41**, 15415-15425.
24. M. K. Cho, A. Lim, S. Y. Lee, H.-J. Kim, S. J. Yoo, Y.-E. Sung, H. S. Park, J. H. Jang, A review on membranes and catalysts for anion exchange membrane water electrolysis single cells, *J. Electrochem. Sci. Technol.* 2017, **8**, 183-196.
25. I. Vincent, D. Bessarabov, Low cost hydrogen production by anion exchange membrane electrolysis: A review, *Renew. Sust. Energy Rev.* 2018, **81**, 1690-1704.
26. K. Zeng, D. Zhang, Recent progress in alkaline water electrolysis for hydrogen production and applications, *Prog. Energy Combust. Sci.* 2010, **36**, 307-326.

27. S. Marini, P. Salvi, P. Nelli, R. Pesenti, M. Villa, M. Berrettoni, G. Zangari, Y. Kiros, Advanced alkaline water electrolysis, *Electrochim. Acta* 2012, **82**, 384-391.
28. S. Marini, P. Salvi, P. Nelli, R. Pesenti, M. Villa, M. Berrettoni, G. Zangari, Y. Kiros, Advanced alkaline water electrolysis, *Electrochimica Acta* 2012, **82**, 384-391.
29. Q. Feng, X.-Z. Yuan, G. Liu, B. Wei, Z. Zhang, H. Li, H. Wang, A review of proton exchange membrane water electrolysis on degradation mechanisms and mitigation strategies, *J. Power Soc.* 2017, **366**, 33-35.
30. M. Carmo, D. L. Fritz, J. Mergel, D. Stolten, A comprehensive review on PEM water electrolysis, *Int. J. Hydrogen Energy* 2013, **38**, 4901-4934.
31. A. H. Abdol Rahim, A. S. Tijani, S. K. Kamarudin, S. Hanapi, An overview of polymer electrolyte membrane electrolyzer for hydrogen production: Modeling and mass transport, *J. Power Sources* 2016, **309**, 56-65.
32. P. Millet, F. Andolfatto, R. Durand, Design and performance of a solid polymer electrolyte water electrolyzer, *Int. J. Hydrogen Energy* 1996, **21**, 87-93.
33. S. Siracusano, V. Baglio, N. Van Dijk, L. Merlo, A.S. Aricò, Enhanced performance and durability of low catalyst loading PEM water electrolyser based on a short-side chain perfluorosulfonic ionomer, *Applied Energy* 2017, **192**, 477-489.
34. M. K. Cho, A. Lim, S. Y. Lee, H.-J. Kim, S. J. Yoo, Y.-E. Sung, H. S. Park, J. H. Jang, A review on membranes and catalysts for anion exchange membrane water electrolysis single cells, *J. Electrochem. Sci. Technol.* 2017, **8**, 183-196.

35. I. Vincent, D. Bessarabov, Low cost hydrogen production by anion exchange membrane electrolysis: A review, *Renew. Sus. Energy Rev.* 2018, **81**, 1690-1704.
36. M. Carmo, D. L. Fritz, W. Maier, D. Stolten, (Invited) Alkaline water electrolysis vs. PEM water electrolysis – exploring their full performance. *Meeting Abstracts 2015*, **MA2015-01**, 1489.
37. H. N. Nong, L. Gna, E. Willinger, D. Teschner, P. Strasser, IrOx core-shell nanocatalysts for cost- and energy-efficient electrochemical water splitting, *Chem. Sci.* 2014, **5**, 2955-2963.
38. X. Huang, Z. Zhao, L. Cao, Y. Chen, E. Zhu, Z. Ling, M. Li, A. Yan, A. Zettl, Y. M. Wang, X. Duan, T. Mueller, Y. Huang, High-performance transition metal-doped Pt₃Ni octahedral for oxygen reduction reaction, *Science* 2015, **348**, 1230-1234.
39. J. Shui, M. Wang, F. Du, L. Dai, N-doped carbon nanomaterials are durable catalysts for oxygen reduction reaction in acidic fuel cells, *Science* 2015, **1**, e1400129.
40. M. Chauhan, K. P. Reddy, C. S. Gopinath, S. Deka, Copper cobalt sulfide nanosheets realizing a promising electrocatalytic oxygen evolution reaction, *ACS Catal.* 2017, **7**, 5871-5879.
41. I. E. L. Stephens, J. Rossmeisl, I. Chorkendorff, Toward sustainable fuel cells, *Science* 2016, **354**, 1378-1379.
42. Y. W. Rho, S. Srinivasan, Y. T. Kho, Mass transport phenomena in proton exchange membrane fuel cells using O₂/He, O₂/Ar, and O₂/N₂ mixtures II. Theoretical Analysis, *J. Electrochem. Soc.* 1994, **114**, 2089-2096.

43. J. Benziger, E. Kimball, R. Mejia-Ariza, I. Kevrekidis, Oxygen mass transport limitations at the cathode of polymer electrolyte membrane fuel cells, *AIChE J.* 2010, **57**, 2505-2517.
44. D. K. Shin, J. H. Yoo, D. G. Kang, M. S. Kim, Effect of cell size in metal foam inserted to the air channel of polymer electrolyte membrane fuel cell for high performance, *Renew. Energy* 2018, **115**, 663-675.
45. B. G. Pollet, The use of power ultrasound for the production of PEMFC and PEMWE catalysts and low-Pt loading and high-performing electrodes, *Catal.* 2019, **9**, 246.
46. S. Siracusano, V. Baglio, N. V. Dijk, L. Merlo, A. S. Arico, Enhanced performance and durability of low catalyst loading in PEM water electrolyser based on a short-side chain perfluorosulfonic ionomer, *Appl. Energy* 2017, **192**, 477-489.
47. H.-S. Oh, H. N. Nong, T. Reier, M. Gliech, P. Strasser, Oxide-supported Ir nanodendrites with high activity and durability for the oxygen evolution reaction in acid PEM water electrolyzers, *Chem. Sci.* 2015, **6**, 3321-3328.
48. J. O. Majasan, F. Lacoviello, P. R. Shearing, D. J. Brett, Effect of microstructure of porous transport layer on performance in polymer electrolyte membrane water electrolyser, *Energy Procedia* 2018, **151**, 111-119.

Chapter 2. Optimization of copper-foam microstructures as flow field for polymer electrolyte membrane fuel cells

2.1. Introduction

To improve the mass transport of PEMFCs, the flow field of bipolar plates is important components, and various kinds of flow fields¹⁻¹³ have been reported to improve mass transport leading to enhancing cell performance. Recently, porous materials, i.e. metallic powder,¹⁰ coils,⁷ mesh,¹¹ and foam,^{4,12,13} have been applied as flow fields and have shown enhanced mass transport. Among them, metal foams are considered to be an important subject as alternative materials to channel and rib flow field structures. Reddy et al.² initially proposed metal foam as a flow field and demonstrated a Ni-Cr structure. Tseng et al.¹³ developed nickel foam coated with polytetrafluoroethylene (PTFE) to increase the hydrophobicity, and achieved high performance (1.87 A·cm⁻² at 0.6 V). Metal foam is hence a good candidate for achieving high performance as it can promote electrochemical reactions with the catalyst by enhancing the mass transport of reactants and products.

As flow field parameters play an important role in the mass transport of the reactants and products,^{2,8} many studies concerning the flow field configuration have been reported. Zhang et al.⁹ examined the effect of channel depth and width on cell performance and observed that these factors affected the pressure drop and under-rib convection in the channel, respectively. They reported the narrow and shallow flow field improved mass transport of oxygen and water, caused by

increased pressure drop. In addition, Karan et al.¹⁴ modelled the effect of the flow field parameters on the reaction distribution and concluded that the channel/rib width ratio affects the cell performance as the channel dimensions determine the oxygen transport behavior, while the rib dimensions affect electron transport. Hence, a step toward achieving the highest performance fuel cell would be to inspect the flow field structure. Likewise, when metal foam is applied as a flow field, it is expected that the structural parameters, i.e. thickness, area density, and pore size, can affect the cell performance; therefore, the cell performance can be increased by optimizing the foam microstructure. However, few studies on regarding optimization of foam structures for flow fields of PEMFCs have been found in the literature.^{4,15}

In this work, we used copper-foam as flow field and optimized their microstructure to determine the optimal flow field design. Copper-foam is a relatively inexpensive material, can be prepared with various structures, and has previously been shown to be a promising candidate as a flow field. Here, the effect of the foam structure (thickness, area density, and pore size) on the flow field performance was experimentally examined. In addition, a copper-foam flow field MEA with a higher catalyst loading and smaller membrane thickness was proposed to achieve outstanding high performance (current density $> 2.0 \text{ A}\cdot\text{cm}^{-2}$ at 0.6 V) and mechanisms behind the enhancement of the cell performance were investigated. Furthermore, we proposed carbon monoxide (CO) poisoning test in single cell to examine the reactant utilization of flow field and evaluated its effect of copper-foam.

2.2. Experimental section

2.2.1. Preparation of copper-foam flow field MEA

The copper-foam flow field MEA and conventional MEA (Figure 2.1) contained a CCM and GDL, while the conventional MEA comprised a serpentine flow field that has been widely used due to its excellent water removal and the copper-foam flow field MEA consisted of a compressed copper-foam flow field. To prepare the copper-foam flow field, the copper-foam was compressed using hot-pressing equipment (HMM-04, Hansung Systems, Inc., Korea) under ambient temperature to prepare samples with different thicknesses. The compressed copper-foams were placed on the bipolar plates without channels and ribs, followed by an in-house method of porous flow field.

Six samples of copper-foam were applied as the flow field of bipolar plates to investigate the optimized copper-foam structure, as shown in Figure 2.2. To characterize the effect of the foam microstructure on the cell performance, two groups of samples were prepared with different area densities (Cu 1, 2, 3 and 4) and pore sizes (Cu 3, 5 and 6). Table 2.1 presents the parameters of copper-foams.

The procedures for fabricating the CCMs, as reported in our previous studies,^{16,17} were used for MEA preparation. The catalyst slurry was made by dispersing the catalyst in a solution of 2-propanol (Sigma Aldrich, USA) and Nafion perfluorinated resin (Sigma Aldrich, USA) under sonication. Carbon-supported Pt catalyst (40 wt. %, Johnson Matthey) was used as the anode and cathode catalysts. Nafion 212 (Dupont, USA) was used as the proton exchange membrane; before fabrication, the membrane was cleaned with 1 M hydrogen peroxide (Daejung Chemicals & Metals Co., Ltd., Korea) at 80 °C for 1 h, and then rinsed with deionized water for 1 h. Next, the membrane was immersed in 0.5 M sulfonic acid (Samchun Chemical, Korea) at 80 °C for 1 h for protonation, and rinsed deionized water. Then, the prepared catalyst ink was sprayed directly onto

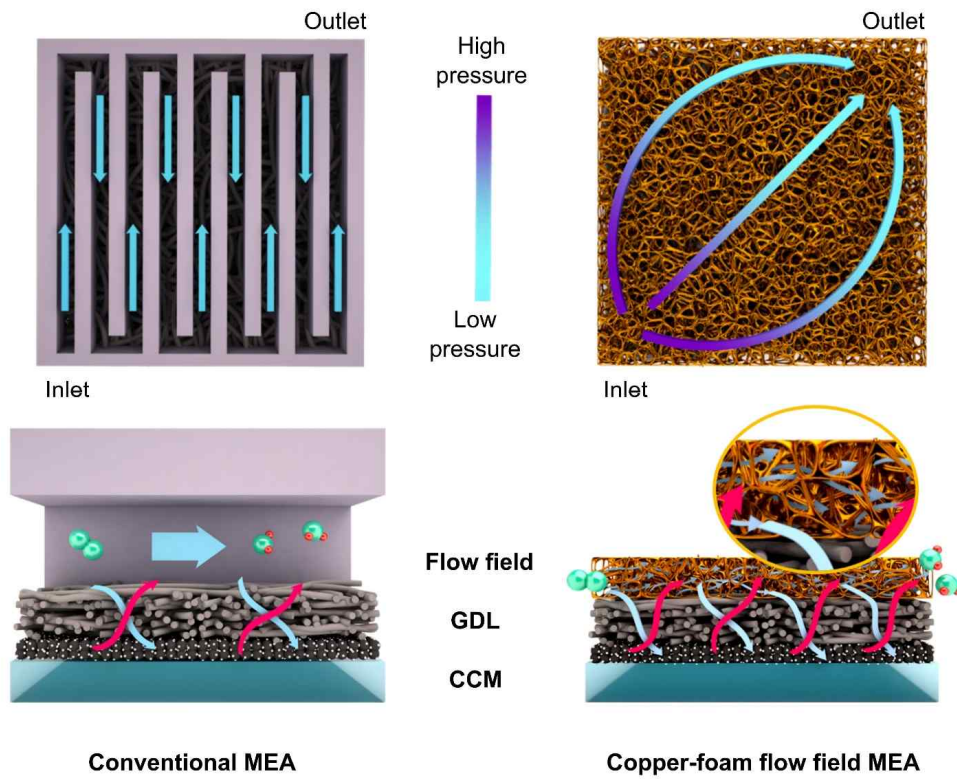


Figure 2.1. Schematic diagrams of the layer structure of the copper-foam flow field MEA and conventional MEA.

the membrane. The catalyst loading was $0.2 \text{ mg}_{\text{Pt}} \cdot \text{cm}^{-2}$. After drying the CCM at room temperature, the GDL was attached to both sides of the CCM.

2.2.2. Physical characterization of the copper-foam

Field-emission scanning electron microscopy (FE-SEM; Carl Zeiss SUPRA 55VP) was used to observe the in-plane and through-plane pore morphology of the copper-foams. The porosity of the copper-foams was measured by mercury intrusion porosimetry (AutoPore IV 9500, Micromeritics, USA). The electrical resistance of the copper-foams was obtained by measuring the sheet resistance (CMT-SR1000N, Gobizkorea, Korea). To compare the hydrophobicity of copper-foam and the conventional flow field, their contact angles were measured using a contact-angle analyzer (Phoenix 300, Surface Electro Optics, Korea).

2.2.3. Electrochemical characterization of copper-foam flow field MEA

In order to evaluate the MEA performance, single-cell polarization curves were obtained using a PEMFC test station (CNL Energy) with an active area of 5 cm^2 and a constant cell temperature of $70 \text{ }^\circ\text{C}$. Hydrogen and air were supplied to the anode and cathode, respectively, and the relative humidity (RH) of the reactants was 100%. The tests were performed at ambient pressure. EIS (IM-6, Zahner-Elektrik GmbH & Co. KG, Germany) was used to measure the resistances of the single-cells under the same operating conditions. The EIS method is a diagnostic tool to separate the activation, ohmic, and concentration resistances under PEMFC operating conditions.¹⁸ The EIS measurements were performed at 0.8, 0.6, and 0.4 V with 5 mV amplitude over the frequency range of 100 kHz to 100 mHz. CV was used to obtain the ECSA of the cathode catalyst layer at a constant cell temperature of $30 \text{ }^\circ\text{C}$. Hydrogen and nitrogen were fed to the anode and cathode, respectively. The voltage sweep range was 0.05 to 1.2 V and the scan rate was $100 \text{ mV} \cdot \text{s}^{-1}$.

CO poisoning test in single-cell was used to examine the effect of the flow field design on reactant utilization. Two kinds of fuel were supplied for anode: (1) pure hydrogen and (2) 100 ppm CO balanced hydrogen. The flow rate was 50 ml·min⁻¹ for anode. The oxygen was supplied for cathode. Before CO poisoning test, single- cell was applied at constant current of 100 mA·cm⁻² supplying pure hydrogen into the anode for 10 min. Then, CO balanced hydrogen gas was injected in anode and voltage change was measured for 6 h while maintaining the current.

2.3. Results and Discussion

2.3.1. Physical property of copper-foam

Copper-foam is a three-dimensionally porous material that has large interconnected pores (100–1500 μm), high porosity, and high electrical conductivity. Table 2.1 compares the physical properties of copper-foam and a conventional (graphite) flow field. Copper has been a typical conductive material used for wire coil for excellent electrical conductivity, and it was confirmed that copper-foam structure also has high electric conductivity. The specific resistance of the copper-foam was smaller than that of the conventional flow field, indicating a higher electrical conductivity. In addition, the contact angles of copper-foam and the conventional flow field were 114.7° and 58.7° , respectively. The large contact angle of the copper-foam means that the material has high hydrophobicity.¹⁹ Thus, copper-foam can be applied as a flow field without additional hydrophobic treatment process, which enhanced water removal. Figure 2.2 and Table 2.2 presents the photographs and parameters of six different copper-foams used in this study.

2.3.2. Effect of copper-foam thickness

The channel depth of flow fields is regarded as an important parameter for cell performance.^{9,20,21} The thickness of the copper-foam is associated with the channel depth of the flow fields and hence, three types of MEA with different copper-foam thicknesses were prepared and the effect of foam thickness was compared to conventional flow with a depth of 1.0 mm fields (serpentine flow field). Most studies of metal foam flow fields^{4,13} performed experiments with single-cells with a foam thickness similar to that of conventional channel depths. Therefore, we used thin copper-foam (< 1 mm) for the flow fields for cell testing as

Table 2.1. Specific resistance ($\text{m}\Omega\cdot\text{cm}$) and contact angle ($^\circ$) of copper-foam and conventional flow field.

	Copper-foam	Conventional flow field (Graphite)
Specific resistance ($\text{m}\Omega\cdot\text{cm}$)	0.05	1
Contact angle ($^\circ$)	114.7	58.7

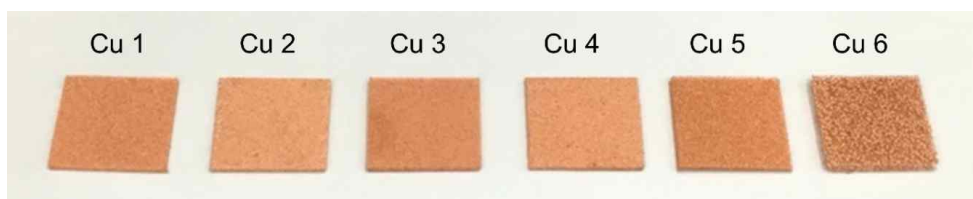


Figure 2.2. Photographs of six different copper-foams (Cu 1-6).

Table 2.2. Copper-foam parameters.

Samples	Cu 1	Cu 2	Cu 3	Cu 4	Cu 5	Cu 6
Pore size (μm)	450	450	450	450	580	1200
Area density ($\text{g}\cdot\text{m}^{-2}$)	600	800	1000	1400	1000	1000

Zhang et al.⁹ reported that shallower channels increased the pressure drop, promoting water removal.

Figure 2.3 shows the polarization and power density curves of the three MEAs using Cu 1 (pore size of 450 μm and area density of 600 $\text{g}\cdot\text{m}^{-2}$) with different copper-foam thicknesses (1 mm, 500, and 250 μm). As the thickness of the copper-foam decreased, the cell performance was enhanced over the measured current density range. In addition, we found that the MEA with the thinner copper-foams (250 and 500 μm) generated internal pressure in the flow field (measured using a system built in-house, as shown in Table 2.3 and Figure 2.3b). When the flow rate was constant, the reduced thickness resulted in a decrease in the volume flow of the reactant, leading to increased internal pressure. The generated pressure in the copper-foams reduced the activation overpotential and increased cell performance without requiring back pressure regulation.^{22,23} However, copper-foam with thickness of less than 250 μm can result in the blockage of in-plane pores owing to compression, exhibiting the reduced performance. Also, internal pressure becomes larger than the supply pressure, so that it becomes hard to supply the reactant. Therefore, the cell performance of copper-foam flow field MEAs was enhanced as the thickness decreased; as we have seen, since the optimum thickness was found to be 250 μm , the following experiments in this paper were conducted using a 250 μm foam.

2.3.3. Effect of area density of copper-foam

The conventional flow field in a bipolar plate transports reactants and generated water through the channel and provides an electrical connection through the ribs. To minimize the ohmic resistance of the copper-foam flow field MEA, the ribs should have a low intrinsic electrical conductivity and large contact area between the gas diffusion layer (GDL) and flow field. Nevertheless, as the ribs

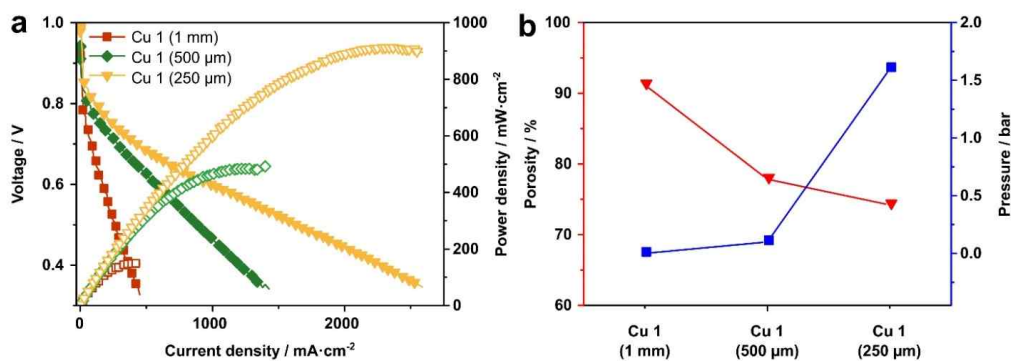


Figure 2.3. Effect of copper foam thickness on the cell performance and microstructure. (a) Polarization and power density curves of three MEAs with different thicknesses (1 mm, 500 μm, and 200 μm) of copper foam (Cu 1). **(b)** Porosity (red data) and pressure generated (blue data) in copper foams with different thicknesses.

Table 2.3 Porosity of compressed copper-foams (250 μm) and pressure generated in copper-foam flow field MEAs.

	Cu 1	Cu 2	Cu 3	Cu 4	Cu 5	Cu 6
Porosity	74.2	56.2	50.1	41.3	55.3	59.6
Pressure (bar)	1.6	2.1	2.4	3.2	1.2	0.45

have a large contact area, the channels occupy a relatively small portion of the flow field, leading to restricted mass transport of the reactant and product. Therefore, the channel-rib ratio must be optimized to achieve a trade-off between the ohmic and mass transport resistances. In the copper-foam, the area density (mass per unit area) can be considered as the channel-rib ratio of the flow field. Figure 2.4 presents scanning electron microscope (SEM) images and a schematic diagram of the copper-foams with different area densities. Both pristine (Figure 2.4a–d) and compressed (Figure 2.4e–h) copper-foams showed through-plane pores and the rib size increased with increasing area density. A higher area density of copper-foam resulted in a lower channel-rib ratio of the conventional flow field, as shown in Figure 2.4i.

To observe the effect of area density on the polarization characteristics, four copper-foams with different area densities of 600 (Cu 1), 800 (Cu 2), 1000 (Cu 3), and 1400 (Cu 4) $\text{g}\cdot\text{m}^{-2}$, respectively, but the same pore size of 450 μm and thickness of 250 μm , were prepared (Table 2.1). Figure 2.5a compares the cell performance of the four different copper-foam flow field MEAs. The area density of copper-foam increased from 600 to 1000 $\text{g}\cdot\text{m}^{-2}$ result in an increase of cell performance. As the area density increased, the contact area (rib) between the GDL and flow field increased, resulting in improved electron transport and decreased ohmic overpotential (Figure 2.5b and Figure 2.6). Also, as shown in Table 2.3, the increased area density led to increased pressure. It affected the activation overpotential, enhancing cell performance (Figure 2.6a). However, as mentioned above, the cell performance and area density of copper-foam did not constantly show a linear relation between them. Although the internal pressure increased, increasing the area density from 1000 to 1400 $\text{g}\cdot\text{m}^{-2}$ resulted in decreased cell performance; the reduction in the channel area hindered mass transport of the

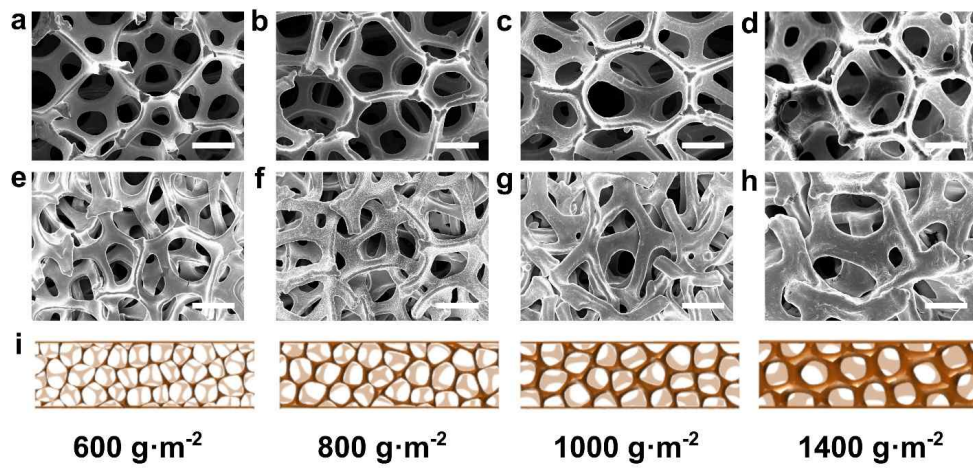


Figure 2.4. Microstructural characterization of the copper-foams. SEM images of samples Cu 1–4 (**a–d**) before and (**e–h**) after compression. (**i**) Schematic diagrams of the corresponding area densities of samples Cu 1–4.

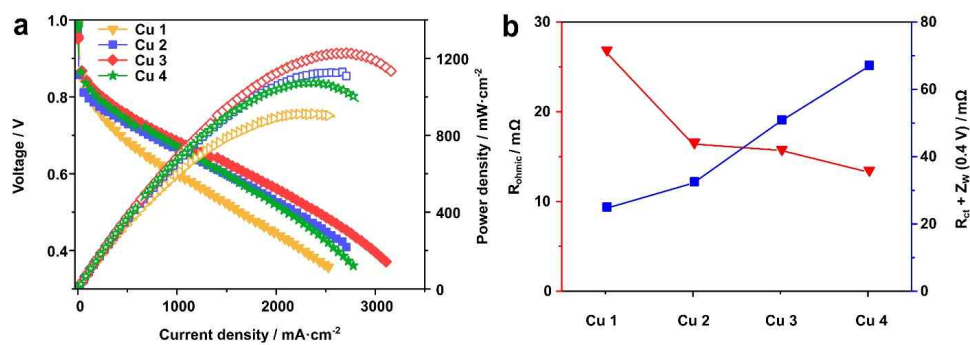


Figure 2.5. Effect of copper-foam area density on the cell performance. (a) Polarization and power density curves for four MEAs with different area densities of copper-foam (Cu 1, 2, 3, and 4). (b) Ohmic resistance ($m\Omega$) obtained at 0.6 V using EIS (red data) and the sum of charge transfer and mass transport resistance ($m\Omega$) obtained at 0.4 V using EIS (blue data) for the copper-foams (Cu 1, 2, 3, and 4).

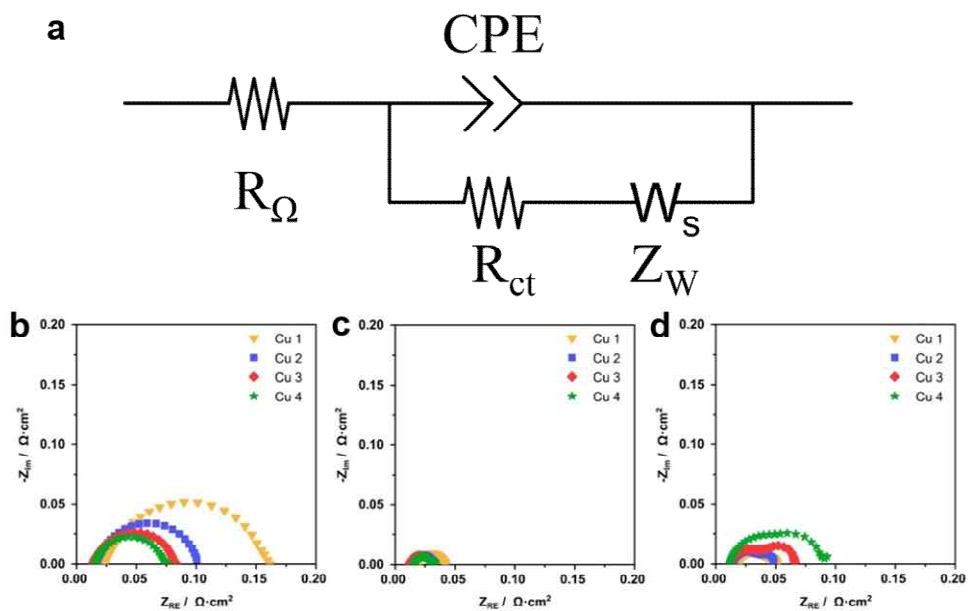


Figure 2.6. (a) Equivalent circuit model and Nyquist plots of copper-foam MEAs with the different area densities (Cu 1-4). (b) 0.8 V, (c) 0.6 V, (d) 0.4 V.

reactant and product resulting in higher mass transport resistance (Figure 2.5b and Figure 2.6c). Although the ohmic resistance of MEAs using Cu 4 was smaller than that of the other MEAs, the increased mass transport resistance was the major factor affecting cell performance. Therefore, an area density of $1000 \text{ g}\cdot\text{m}^{-2}$ (Cu 3) was considered optimal value.

2.3.4. Effect of pore size of copper-foam

The effect of the pore size of copper-foams was investigated for samples with the optimized area density of $1000 \text{ g}\cdot\text{m}^{-2}$. The pore sizes of three samples were 450 (Cu 3), 580 (Cu 5), and $1200 \mu\text{m}$ (Cu 6), respectively (Table 2.1), where their pore morphology is shown in Figure 2.7. After compressing the foam plates to $250 \mu\text{m}$, through-plane pores were still observed. Figure 2.8a shows the cell performance of MEAs with different pore sizes. As the area density of the three MEAs was equal, the ohmic resistances were constant, eliminating the effect of the ohmic overpotential (Figure 2.9b). As shown in Figure 2.8a, the cell performance decreased with increasing pore size due to increased charge-transfer resistance (Figure 2.9a) caused by reduced internal pressure (Table 2.3) and mass transport resistance (Figure 2.8b and Figure 2.9d). As the pore size of the foam is large, the internal surface area is reduced. And the reduction of internal surface area leads to a decrease in the form drag, thereby reducing pressure change.

2.3.5. Optimized cell performance of copper-foam flow field MEAs

Sample Cu 3 was considered to have the optimal structure as it exhibited the highest cell performance. Figure 2.10 compares cell performance of this sample and a conventional flow field MEA. Except the flow field, all cell components and operating condition of two MEAs were same. In the measured current density range, the performance of the copper-foam flow field MEA was higher than that of

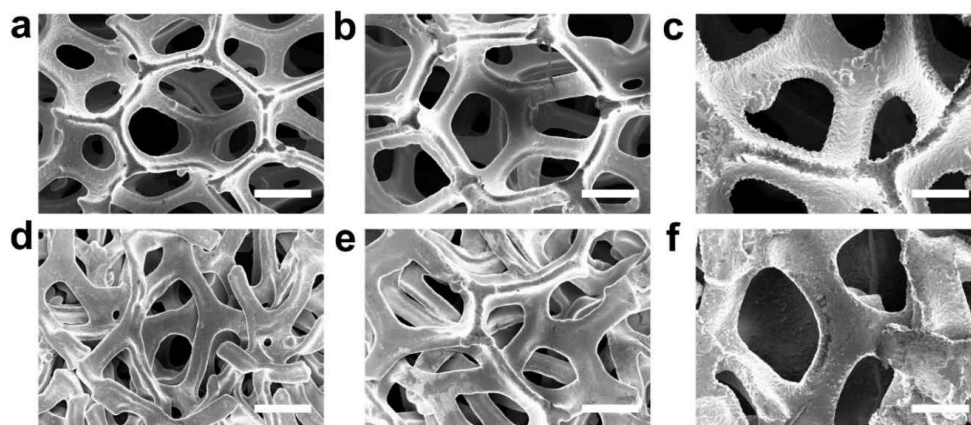


Figure 2.7. SEM images of (a-c) pristine Cu 3, 5, and 6 and (d-f) compressed Cu 3, 5, and 6. The scale bar is 250 μm .

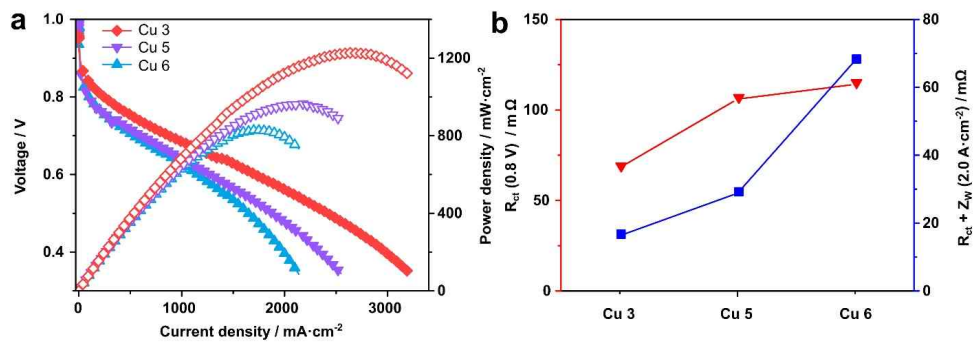


Figure 2.8. Effect of copper-foam pore size on the cell performance. (a) Polarization and power density curves of the three MEAs with different copper-foam pore sizes (Cu 3, 5, and 6). (b) Charge transfer resistance (mΩ) obtained at 0.8 V using EIS (red data) and the sum of charge transfer and mass transport resistance (mΩ) obtained at 2.0 A·cm⁻² using EIS (blue data) for copper-foams (Cu 3, 5, and 6).

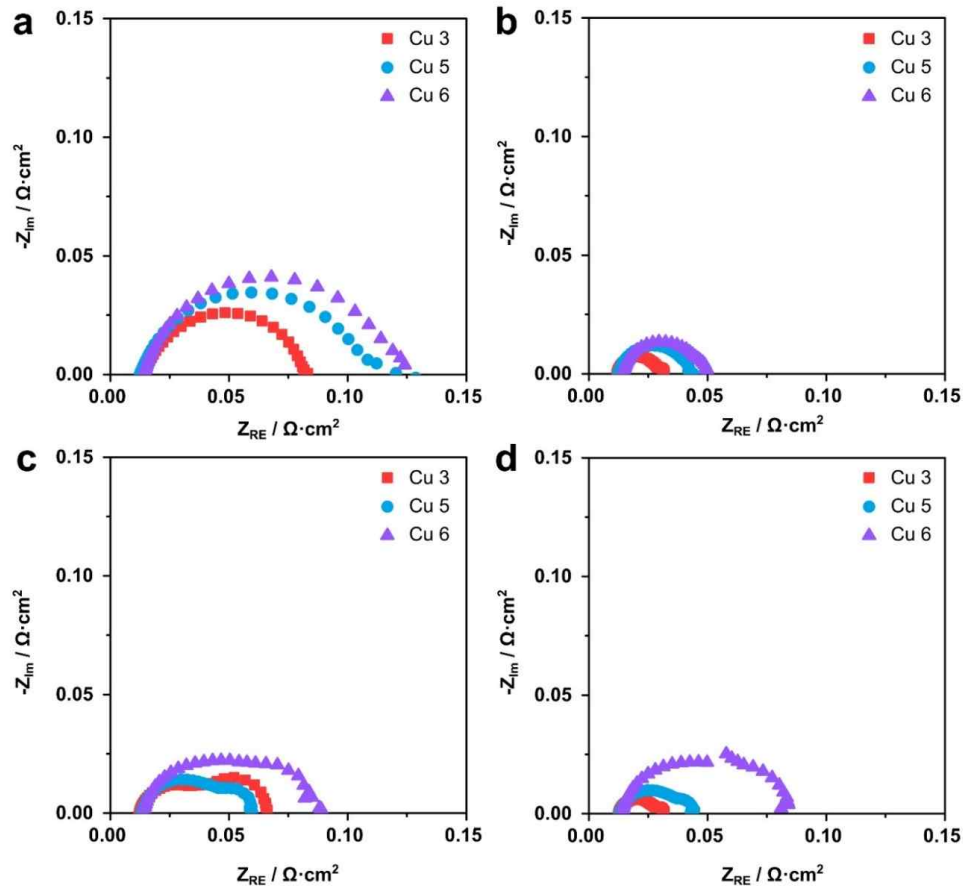


Figure 2.9. Nyquist plots of copper-foam MEAs with the different pore sizes (Cu 3, 5, 6). **(a)** 0.8 V, **(b)** 0.6 V, **(c)** 0.4 V, **(d)** 2.0 A·cm⁻².

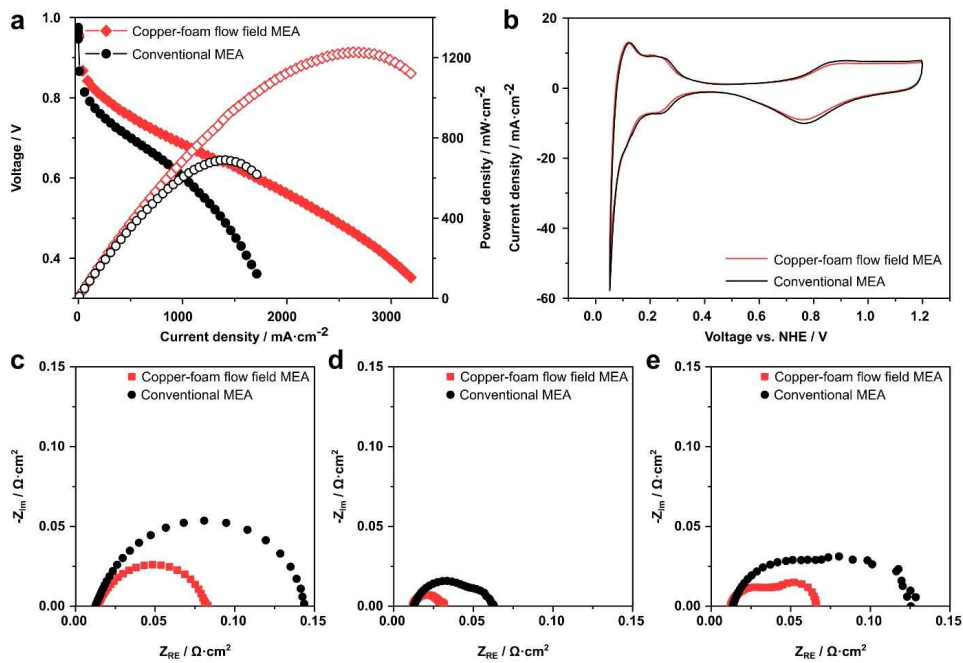


Figure 2.10. Comparison of the performance of copper-foam and conventional flow field MEAs. (a) Voltage as a function of current density. (b) Cyclic voltammetry curves. (c–e) Nyquist plots obtained at (c) 0.8 V, (d) 0.6 V, and (e) 0.4 V.

the conventional one. The current density values of the copper-foam flow field MEA at 0.8, 0.6, and 0.4 V was 0.25, 1.71, and 2.98 A·cm⁻², respectively, whereas those of the conventional flow field MEA were 0.09, 1.02, and 1.622 A·cm⁻², respectively. The power density of the copper-foam was 1.228 W·cm⁻², which was 178% higher than that of the conventional flow field MEA (0.689 W·cm⁻²). In addition, the total current density of the copper-foam was 3.188 A·cm⁻², which was 182% greater than that of conventional flow field MEA (1.752 A·cm⁻²). In addition, CV measurements were performed to examine the electrochemical surface area (ECSA) of the two MEAs (Figure 2.10b). The ECSA of the copper-foam flow field MEA was 45.45 m²·g⁻¹, which was approximately equal to that of the conventional flow field MEA (46.1 m²·g⁻¹). Hence, the enhanced cell performance was attributed only to the use of the copper-foam as the flow field.

To examine the effect of the activation, ohmic, and concentration overpotentials, EIS was used to measure the resistances of single-cells. Figure 2.10c–e shows Nyquist plots obtained at 0.8, 0.6, and 0.4 V. At high voltage (0.8 V), the charge-transfer resistance, calculated from the diameter of the semicircle, was attributed to the activation overpotential, i.e. catalyst kinetics, temperature, and reactant concentration. As shown in Figure 2.10c, the diameter of the semicircle of the copper-foam flow field MEA was smaller than that of the conventional flow field MEA, meaning that the former had a smaller activation overpotential. Generally, when the catalyst-coated membrane (CCM) and operation conditions are the same, the activation overpotential of MEA is constant. Although the two MEAs used the same CCM and were tested under the same operation conditions, the copper-foam flow field MEA had a smaller activation overpotential. This could have been due to the pressure generated in the copper-foam, as mentioned previously. In addition, we observed that the ohmic resistance was dominant at 0.6 V. Figure 2.10d shows that the ohmic resistance of the two MEAs was

approximately the same resulting from the similar contact areas of the GDL and flow field. In addition, the mass transport resistance of the copper-foam flow field MEA was smaller than that of the conventional flow field MEA (Figure 2.10e). In the low voltage region (0.4 V), which was affected mainly by mass transport, two arcs in the Nyquist plot were observed. A single arc at high frequencies represents the activation overpotential, which is consistent with the arc observed in the high voltage region. The low frequency arc is related to mass transport resistance. As shown in Figure 2.10e, the Nyquist plot showed a feature at 0.4 V containing two semicircles that were difficult to distinguish, representing the sum of the charge transfer and mass transport resistance. This combined arc of the copper-foam flow field MEA was smaller than that of conventional flow field MEA, indicating a smaller mass transport resistance. Therefore, the enhanced cell performance was attributed to decreased activation and mass transport resistance.

To optimize the performance of the copper-foam flow field MEA, the Pt catalyst loading was varied from 0.2 to 0.3 mg·cm⁻² and a thinner membrane (Nafion 211, Dupont, USA) was used to decrease ohmic overpotential. Figure 2.11a shows the cell performance of the optimized copper-foam flow field MEA which was evaluated under fully humidified H₂ and air at 70 °C and ambient pressure. The cell performance at 0.6 V was approximately 2.2 A·cm⁻², which to the best of our knowledge is the best performance reported to date for PEMFCs,^{11,24-28} despite the ambient pressure condition (Figure 2.11b and Table 2.4). In addition, durability tests were undertaken using load cycling from OCV to 0.35 V. Generally, it is expected that the copper is susceptible to corrosion under acidic conditions, leading to severe performance degradation.^{29,30} However, as shown in Figure 2.12, the optimized copper-foam flow field MEA exhibited superior stability with negligible performance overpotential after 8 h; hence, the

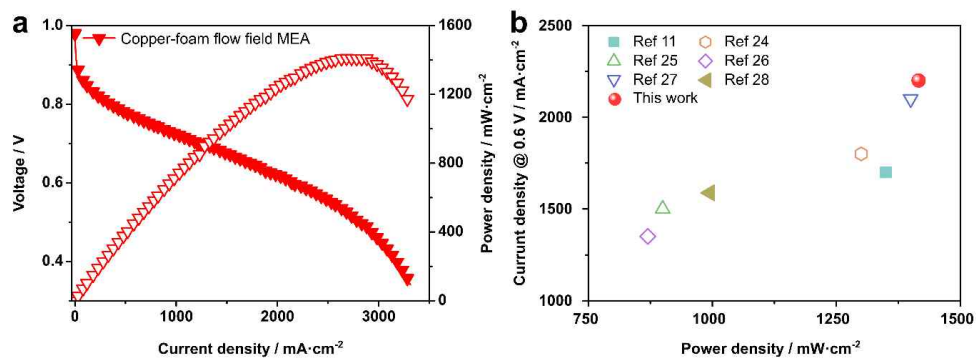


Figure 2.11. Performance of optimized copper-foam flow field MEA. (a) Voltage as a function of current density of optimized copper-foam flow field MEA. **(b)** The comparison of current density at 0.6 V and maximum power density exhibited in this study and those reported in literature^{11,24-28} (Solid: ambient pressure, Open: back pressure).

Table 2.4. Operating condition of the references shown in the performance comparison (Fig. 2.11b).

Ref. No.	Operation Temp. (°C)	Area (cm ²)	Relative humidity (%)	Back pressure (bar)	Membrane	Catalyst loading (mg _{Pt} ·cm ⁻²)
11	70	5	100/100	0	Nafion 211	0.4/0.4
24	80	5	100/100	1.5	Nafion 212	0.2/0.2
25	-	5	-	1.5	Nafion 212	0.12/0.12
26	80	5	100/100	1.5	Nafion 212	0.5/0.5
27	80	5	100/100	0.8	Nafion 211	0.2/0.2
28	75	1	100/100	0	Nafion 212	0.4/0.4

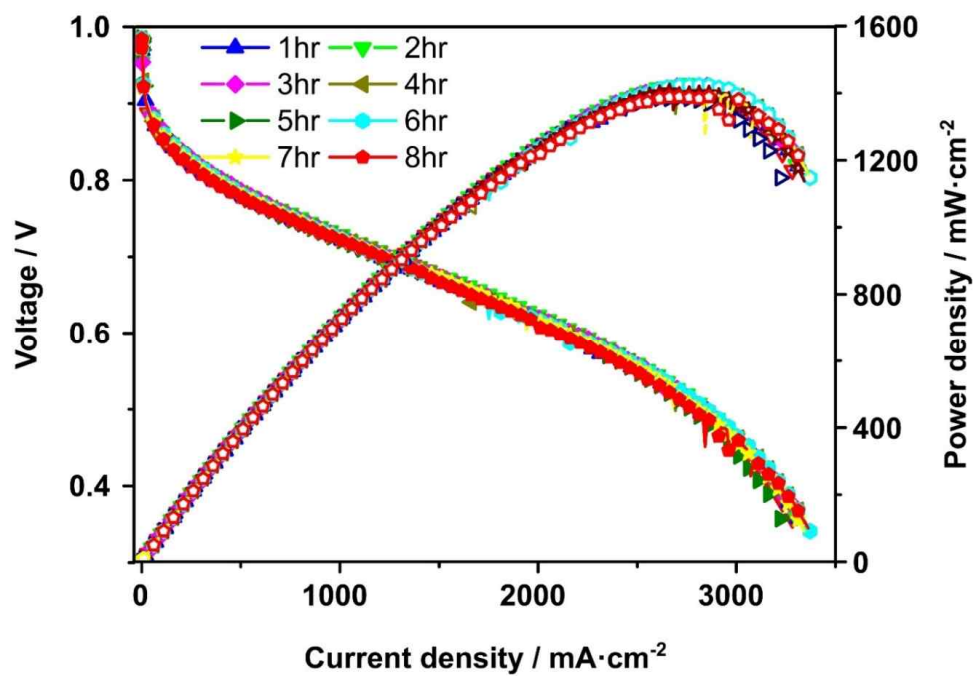


Figure 2.12. Stability test of copper-foam flow field MEA for 8 h.

corrosion of copper under operation conditions of the PEMFCs did not result in significant performance degradation.

2.3.6. Copper-foam flow field

We have shown that the use of copper-foam as a flow field resulted in the increased cell performance compared to conventional flow field. The increase in performance is due to pressure and it was attributed to form drag in the porous structure, which occurs due to a pressure difference across an obstacle and dominates over frictional drag in the copper-foam with more bluff bodies and increased metal density,³¹⁻³⁵ as shown in Figure 2.1. Additionally, when the thickness of the copper-foam was decreased, the pressure increased according to the following Forchheimer-extended Darcy equation,^{32,34} which describes the pressure change in a porous media with form drag.³⁴

$$\frac{\Delta p}{L} = \frac{\mu}{K}v + \rho Cv^2 \quad (1)$$

where Δp is the pressure drop, L is the length of the porous medium, K is permeability, C is the form drag coefficient, and v is the Darcian velocity, which is calculated by dividing the volumetric flow rate by the cross-sectional area. As the volumetric flow rate was constant, the decreased thickness of the copper-foam resulted in a reduced cross-sectional area, leading to increased Darcian velocity and a corresponding pressure drop. In addition, the decreased porosity of the copper-foam after compression resulted in decreased permeability and increased pressure drop.³⁵ Previous studies of metal foam flow fields for PEMFCs did not observe this phenomenon as thicker and highly porous metal foams were used than in this study.

The performance increase by pressure drop is related to two main factors. Firstly, the pressure generated in the copper-foams increased the thermodynamic and kinetic of electrochemical reaction in catalyst, leading to the decreased

activation overpotential. The following equation shows the activation overpotential for pressure.

$$E = E^0 - \frac{RT}{2F} \ln \frac{1}{pH_2 (pO_2)^{\frac{1}{2}}} \quad (2)$$

$$j = j_0 \left(\frac{C_R}{C_R^0} e^{\alpha n F \eta_{ct} / RT} - \frac{C_P}{C_P^0} e^{-(1-\alpha) n F \eta_{ct} / RT} \right) \quad (3)$$

$$j_0 = n F k^0 C_R \quad (4)$$

where E^0 is the standard potential of reaction, E is the potential of reference, electromotive force, R is the gas constant, T is the temperature, F is the Faraday constant, pH_2 is the pressure of hydrogen, pO_2 is the pressure of oxygen, j is the current density, j_0 is the exchange current density, C_R is the surface concentration of reactant, C_R^0 is the bulk concentration of reactant, C_P is the surface concentration of product, C_P^0 is the bulk concentration of reactant, η_{ct} is the charge-transfer overpotential, α is the transfer coefficient, n is the number of electrons involved in an electrode reaction, k^0 is the standard rate constant. Thermodynamically, the increase in voltage as pressure increases can be explained by the Nernst equation. For the kinetic, the influence of pressure can be described by the Butler-Volmer equation. The activation overpotential depends on the exchange current density and the reactant concentration. As the exchange current density and the reactant concentration increases, the activation overpotential rises. At constant temperature, exchange current density is increased as the concentration of reactant increases. Thus, self-generated pressure in copper-foam reduced activation overpotential.

Secondly, the self-generated pressure in copper-foam flow field enhanced the mass transport of the reactant and water, leading to increased utilization of the reactant and hence, cell performance.

$$\eta_{mt} = \left(1 + \frac{1}{\alpha}\right) \frac{RT}{nF} \ln\left(\frac{j_l}{j_l - j}\right) \quad (5)$$

$$j_l = nFD \frac{x_{O_2} P}{t RT} \quad (6)$$

$$d\eta_{mt} = \left(1 + \frac{1}{\alpha}\right) \frac{RT}{nF} \frac{-j}{j_l - j} \frac{dP}{P} \quad (7)$$

where η_{mt} is the mass-transfer overpotential, j_l is the limit current density, j is the current density, x_{O_2} is the mole fraction of O_2 , P is the pressure, t is the electrode diffusion layer thickness, D is the diffusion coefficient of oxygen, and at constant temperature, mass-transfer overpotential decreases with increasing pressure. The improved water removal is the result of the increased pressure in the copper-foam. The pressure drop between the inlet and outlet is crucial for the water management in the channel of conventional flow fields³⁶⁻³⁸ and is also relevant for the copper-foam flow field.

In addition, the foam structure, which has much narrower channel and rib features than conventional flow field, is a suitable design for enhancing mass transport. To examine the effect of the flow field design, three MEAs were prepared and evaluated: a copper-foam flow field MEA, a conventional flow field MEA, and a micro flow field MEA where the widths of the channels and ribs were narrower than that of the conventional flow field MEA (Figure 2.13a). Figure 2.13b shows the performance of the three MEAs operated under ambient pressure. The copper-foam flow field MEA exhibited a much higher performance for all current densities compared to the other MEAs as it showed a lower activation overpotential due to the self-generated pressure. In addition, the performance of the micro flow field MEA was higher than that of the conventional flow field MEA at high current densities due to the narrower channel/rib width. To investigate the effect of the copper-foam on mass transport by eliminating the difference in

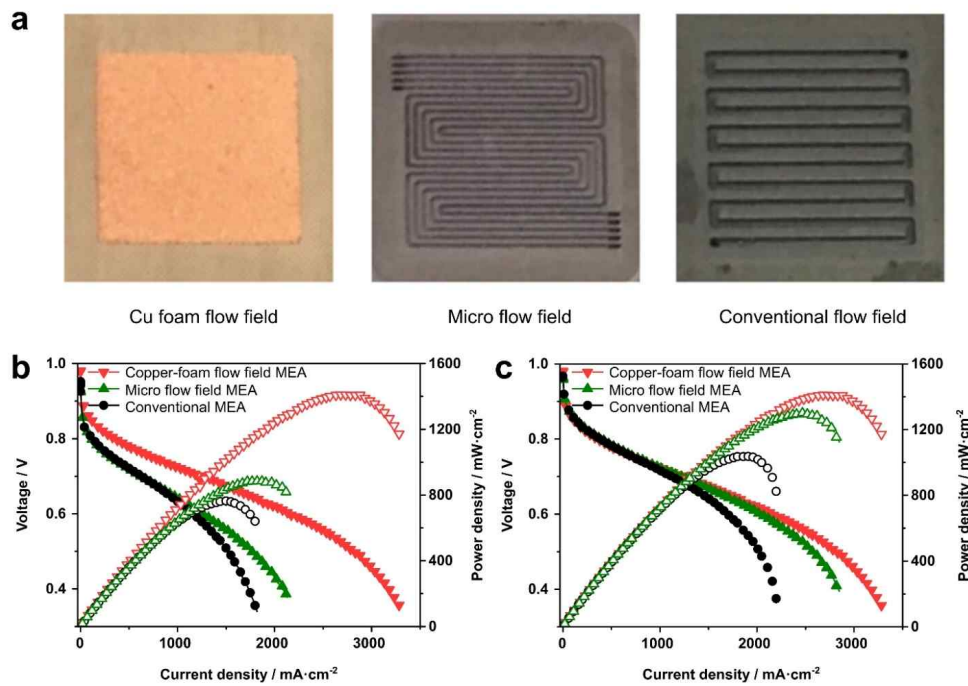


Figure 2.13. Comparison of the performance of three different flow fields (copper foam, micro flow field, and conventional flow field). (a) Photographs of the three flow fields. (b) Voltage as a function of current density at ambient pressure. (c) Voltage as a function of current density at ambient pressure (copper foam MEA), and with a back pressure of 1.8 bar (micro flow field MEA and conventional MEA).

activation overpotential, it was compared to the two other MEAs operated under a back pressure of 1.8 bar (Figure 2.13c). The copper-foam flow field MEA exhibited the highest performance among the three MEAs although it was tested at ambient pressure. In the low voltage region where the mass transport overpotential is dominant, the performance was enhanced (copper-foam flow field MEA > micro flow field MEA > conventional flow field MEA). When the activation overpotential effect was eliminated, the copper-foam flow field MEA exhibited the lowest mass transport overpotential due to the narrower channel/rib widths. As shown in Figure 2.13a, the copper-foam flow field MEA had the smallest channel and rib widths, followed by the micro flow field flow field MEA and conventional flow field MEA. Zhang et al.⁹ stated that narrower channel/rib widths resulted in larger under-rib convection and more efficient water removal; this is consistent with the polarization curves of the three MEAs. In addition to the pressure effect, the better performance of the copper-foam was attributed to under-rib convection, which could increase concentration of the reactant and remove generated water droplets. Therefore, the synergistic effect of self-generated pressure and the microstructure of the copper-foam led to improved reactant utilization, thereby maximizing electrochemical reactions with the catalyst and enhancing cell performance.

2.3.7. CO poisoning test of copper-foam flow field MEAs

Generally, CO has been considered as pollutant in fuel cell as CO is adsorbed on the surface of Pt catalyst and thereby blocking the site where the electrochemical reaction occurs.³⁹ In other words, when CO gas is supplied to single-cell, the cell performance can be decreased due to the CO poisoning. In this work, we applied CO poisoning test in single-cell to evaluate the capability of reactant utilization in flow fields. When CO is supplied to flow field with same

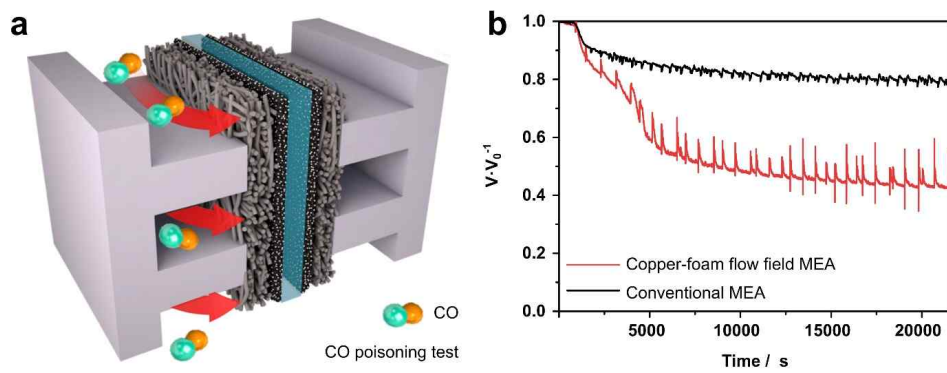


Figure 2.14. CO poisoning test of copper-foam flow field MEA and conventional flow field MEA. (a) Schematic diagram of CO poisoning test and **(b)** normalized voltage profile of copper-foam flow field MEA and conventional flow field MEA during CO poisoning test.

flow rate, the degree of decrease in cell performance depends on the amount of CO particles transported in catalyst layer. The effect of reactant utilization in flow field was examined by comparing the performance reduction. It is expected that CO poisoning results exhibits the rapid decrease in cell performance when using the flow field which has enhanced utilization of reactant. Figure 2.14 presents the schematic diagram and result of CO poisoning test. As illustrated in Figure 2.14a, CO with flow rate of 100 ppm was supplied in anode of two MEAs (copper-foam flow field MEA and conventional flow field MEA). Figure 2.14b shows the normalized voltage change in copper-foam flow field MEA and conventional flow field MEA. In both cases, the cell voltage was decreased after the CO gas was supplied. However, the CO poisoning test showed the performance reduction in copper-foam flow field MEA (57%) was higher than that in conventional flow field MEA (22%). This result indicates that copper-foam flow field enhanced the utilization of reactant, leading to the more reactant transported in catalyst layer. To confirm the effect of self-generated pressure in copper-foam, the conventional flow field MEA with 1.8 bar back pressure was also conducted using CO poisoning test. As shown Figure 2.15, the conventional flow field MEA operated with 1.8 bar back pressure exhibited similar performance reduction compared to copper-foam flow field MEA. That is, the self-generated pressure caused by microstructure of copper-foam resulted in improved reactant utilization, exhibiting outstanding performance.

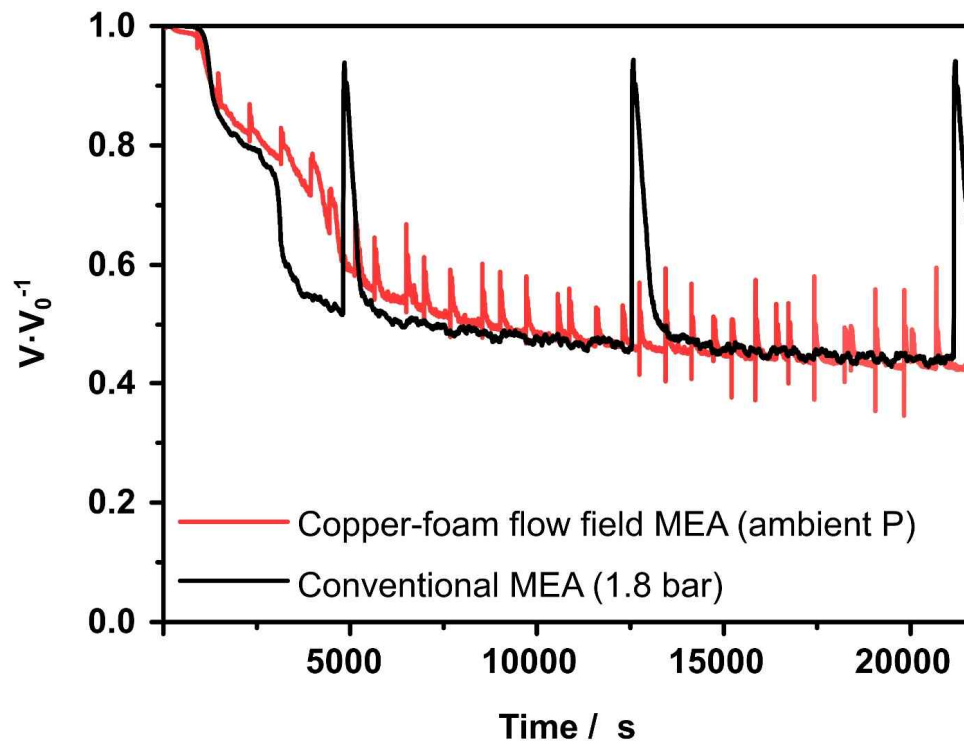


Figure 2.15. Normalized voltage profile of copper-foam MEA (ambient pressure) and conventional MEA (1.8 bar back pressure).

2.4. Conclusions

In this work, we developed copper-foam flow field MEAs and optimized the structure of the copper-foam flow field. The thickness, area density, and pore size of the copper-foam significantly affected the cell performance and the optimal structure was determined using single-cell tests, resulting in a high current density of $2.2 \text{ A}\cdot\text{cm}^{-2}$ at 0.6 V . This is the highest performance reported in the field to date. Also, CO poisoning test showed that the copper-foam flow field MEA exhibited higher performance reduction compared to conventional flow field MEA, indicating the increased utilization of reactant. It was attributed to self-generated pressure in the compressed copper-foam caused by force drag. In addition, self-generated pressure increased the kinetic of electrochemical reaction and enhanced the reactant utilization. Furthermore, the copper-foam flow field evenly distributed the reactants and effectively removed water, leading to decreased concentration overpotential due to its structural characteristic. Therefore, the use of a copper-foam flow field is considered to have great potential for achieving high performance PEMFCs by optimizing the electrochemical reactions conditions with the catalyst and maximizing the fuel cell performance.

2.5. References

1. A. Kumar and R. G. Reddy, Materials and design development for bipolar/end plates in fuel cells, *J. Power Sources*, 2004, **129**, 62-67.
2. X. Li and I. Sabir, Review of bipolar plates in PEM fuel cells: flow-field designs, *Int. J. Hydrogen Energy*, 2005, **30**, 359-371.
3. Y. Wang, Porous-media flow fields for polymer electrolyte fuel cells I. low humidity operation, *J. Electrochem. Soc.*, 2009, **156**, B1124.
4. B.-T. Tsai, C.-J. Tseng, Z.-S. Liu, C.-H. Wang, C.-I. Lee, C.-C. Yang and S.-K. Lo, Effects of flow field design on the performance of a PEM fuel cell with metal foam as the flow distributor, *Int. J. Hydrogen Energy*, 2012, **37**, 13060-13066.
5. P. Trogadas, J. I. S. Cho, T. P. Neville, J. Marquis, B. Wu, D. J. L. Brett, M.-O. Coppens, A lung-inspired approach to scalable and robust fuel cell design, *Energy Environ. Sci.*, 2018, **11**, 136-143.
6. T. Kariya, T. Hirono, H. Funakubo and T. Shudo, Effects of the porous structures in the porous flow field type separators on fuel cell performances, *Int. J. Hydrogen Energy*, 2014, **39**, 15072-15080.
7. S. Tanaka and T. Shudo, Significant performance improvement in terms of reduced cathode flooding in polymer electrolyte fuel cell using a stainless-steel microcoil gas flow field, *J. Power Sources*, 2014, **248**, 524-532.
8. B. H. Lim, E. H. Majlan, W. R. W. Daud, T. Husaini and M. I. Rosli, Effects of flow field design on water management and reactant distribution in PEMFC: a review, *Ionics*, 2016, **22**, 301-316.
9. C. Wang, Q. Zhang, S. Shen, X. Yan, F. Zhu, X. Cheng and J. Zhang, The respective effect of under-rib convection and pressure drop of flow fields on the performance of PEM fuel cells, *Sci. Rep.*, 2017, **7**, 43447.

10. A. K. Srouji, L. J. Zheng, R. Dross, A. Turhan and M. M. Mench, Performance and mass transport in open metallic element architecture fuel cells at ultra-high current density, *J. Power Sources*, 2012, **218**, 341-347.
11. S. Tanaka and T. Shudo, Corrugated mesh flow channel and novel microporous layers for reducing flooding and resistance in gas diffusion layer-less polymer electrolyte fuel cells, *J. Power Sources*, 2014, **268**, 183-193.
12. A. Kumar and R. G. Reddy, Modeling of polymer electrolyte membrane fuel cell with metal foam in the flow-field of the bipolar/end plates, *J. Power Sources*, 2003, **114**, 54-62.
13. C.-J. Tseng, B. T. Tsai, Z.-S. Liu, T.-C. Cheng, W.-C. Chang and S.-K. Lo, A PEM fuel cell with metal foam as flow distributor, *Energy Convers. Manage.*, 2012, **62**, 14-21.
14. W. Sun, B. A. Peppley and K. Karan, Modeling the influence of GDL and flow-field plate parameters on the reaction distribution in the PEMFC cathode catalyst layer, *J. Power Sources*, 2005, **144**, 42-53.
15. D. K. Shin, J. H. Yoo, D. G. Kang and M. S. Kim, Effect of cell size in metal foam inserted to the air channel of polymer electrolyte membrane fuel cell for high performance, *Renewable Energy*, 2018, **115**, 663-675.
16. H. Choi, O. H. Kim, M. Kim, H. Choe, Y. H. Cho and Y. E. Sung, Next-generation polymer-electrolyte-membrane fuel cells using titanium foam as gas diffusion layer, *ACS applied materials & interfaces*, 2014, **6**, 7665-7671.
17. J. E. Park, J. Lim, S. Kim, I. Choi, C.-Y. Ahn, W. Hwang, M. S. Lim, Y.-H. Cho, Y.-E. Sung, Enhancement of mass transport in fuel cells

- using three-dimensional graphene foam as flow field, *Electrochim. Acta*, 2018, **265**, 488-496.
18. P. M. Gomadam and J. W. Weidner, Analysis of electrochemical impedance spectroscopy in proton exchange membrane fuel cells, *International Journal of Energy Research*, 2005, **29**, 1133-1151.
 19. D. Daffonchio, J. Thaveesri and W. Verstraete, Contact angle measurement and cell hydrophobicity of granular sludge from upflow anaerobic sludge bed reactors, *Applied and Environmental Microbiology*, 1995, **61**, 3676-3680.
 20. Y.-M. Ferng, A. Su and S.-M. Lu, Experiment and simulation investigations for effects of flow channel patterns on the PEMFC performance, *International Journal of Energy Research*, 2008, **32**, 12-23.
 21. M. Muthukumar, P. Karthikeyan, M. Vairavel, C. Loganathan, S. Praveenkumar, A. P. Senthil Kumar, Numerical studies on PEM fuel cell with different landing to channel width of flow channel, *Procedia Eng.*, 2014, **97**, 1534-1542.
 22. J. M. Sierra, P. J. Sebastian and S. A. Gamboa, Parametric study of a single cell PEM fuel cell, *ECS Transactions*, 2009, **17**, 315-323.
 23. T. V. Reshetenko, G. Bender, K. Bethune and R. Rocheleau, Systematic study of back pressure and anode stoichiometry effects on spatial PEMFC performance distribution, *Electrochim. Acta*, 2011, **56**, 8700-8710.
 24. O.-H. Kim, Y.-H. Cho, S. H. Kang, H.-Y. Park, M. Kim, J. W. Lim, D. Y. Chung, M. J. Lee, H. Choe, Y.-E. Sung, Ordered macroporous platinum electrode and enhanced mass transfer in fuel cells using inverse opal structure, *Nature Commun.*, 2013, **4**, 2473.

25. H. Cho, S. M. Kim, Y. S. Kang, J. Kim, S. Jang, M. Kim, H. Park, J. W. Bang, S. Seo, K.-Y. Suh, Y.-E. Sung, M. Choi, Multiplex lithography for multilevel multiscale architectures and its application to polymer electrolyte membrane fuel cell, *Nature Commun.*, 2015, **6**, 8484.
26. C. H. Park, S. Y. Lee, D. S. Hwang, D. W. Shin, D. H. Cho, K. H. Lee, T.-W. Kim, M. Lee, D.-S. Kim, C. M. Doherty, A. W. Thornton, A. J. Hill, M. D. Guiver, Y. M. Lee, Nanocrack-regulated self-humidifying membranes, *Nature*, 2016, **532**, 480-483.
27. J. Choi, J.-H. Jang, C.-W. Roh, S. Yang, J. Kim, J. Lim, S. J. Yoo, H. Lee, Gram-scale synthesis of highly active and durable octahedral PtNi nanoparticle catalysts for proton exchange membrane fuel cell, *Appl. Catal. B* 2018, **255**, 530-537.
28. Y. Jeon, Y. Ji, Y. I. Cho, C. Lee, D.-H. Park, Y.-G. Shul, Oxide-carbon nanofibrous composite support for a highly active and stable polymer electrolyte membrane fuel-cell catalyst, *ACS Nano*, 2018, **12**, 6819-6829.
29. S. Karimi, N. Fraser, B. Roberts and F. R. Foulkes, A review of metallic bipolar plates for proton exchange membrane fuel cells: materials and fabrication methods, *Advances in Materials Science and Engineering*, 2012, **22**, 828070.
30. W. Yuan, Y. Tang, X. Yang and Z. Wan, Porous metal materials for polymer electrolyte membrane fuel cells - A review, *Applied Energy*, 2012, **94**, 309-329.
31. P. Du Plessis, A. Montillet, J. Comiti and J. Legrand, Pressure drop prediction for flow through high porosity metallic foams, *Chem. Eng. Sci.*, 1994, **49**, 3545-3553.

32. K. Boomsma and D. Poulikakos, The effects of compression and pore size variations on the liquid flow characteristics in metal foams, *J. Fluids Eng.*, 2001, **124**, 263-272.
33. J. J. Hwang, G. J. Hwang, R. H. Yeh and C. H. Chao, Measurement of interstitial convective heat transfer and frictional drag for flow across metal foams, *J. Heat Transfer*, 2001, **124**, 120-129.
34. N. Dukhan, Correlations for the pressure drop for flow through metal foam, *Exp. Fluids*, 2006, **41**, 665-672.
35. Ö. Bağcı and N. Dukhan, Experimental hydrodynamics of high-porosity metal foam: effect of pore density, *Int. J. Heat Mass Transfer*, 2016, **103**, 879-885.
36. Y. Li, P. Pei, Z. Wu, H. Xu, D. Chen and S. Huang, Novel approach to determine cathode two-phase-flow pressure drop of proton exchange membrane fuel cell and its application on water management, *Applied Energy*, 2017, **190**, 713-724.
37. P. Pei, Y. Li, H. Xu and Z. Wu, A review on water fault diagnosis of PEMFC associated with the pressure drop, *Applied Energy*, 2016, **173**, 366-385.
38. Z. Lu, S. G. Kandlikar, C. Rath, M. Grimm, W. Domigan, A. D. White, M. Hardbarger, J. P. Owejan and T. A. Trabold, Water management studies in PEM fuel cells, part II: ex situ investigation of flow maldistribution, pressure drop and two-phase flow pattern in gas channels, *Int. J. Hydrogen Energy*, 2009, **34**, 3445-3456.
39. Z. Qi, C. He and A. Kaufman, Effect of CO in the anode fuel on the performance of PEM fuel cell cathode, *J. Power Sources*, 2002, **111**, 239-272.

Chapter 3. Ultra-Low Loading of IrO₂ with an Inverse-Opal Structure in a Polymer-Exchange Membrane Water Electrolysis

3.1. Introduction

A high loading (1.5–3.0 mg·cm⁻²) of the noble metal catalyst is used to achieve high PEMWE performance.¹⁻⁵ The studies included a conventional porous catalyst layer that was fabricated by using the spraying method of catalyst slurry including a catalyst and an ionomer. In contrast to the conventional catalyst layer formed by catalyst particles, the development of a new catalyst layer is crucial to improve the utilization of the catalyst. Slavhceva et al.⁶ applied sputtered iridium oxide (IrO₂) on carbon paper as an anode in PEMWE to decrease the loading of IrO₂. By magnetron sputtering, a thin film of IrO₂ on carbon paper was prepared, showing a performance of 300 mA·cm⁻² at 1.6 V. Its catalyst loading was 0.2 mg·cm⁻², which was significantly lower than that of the commercially used loading. Lee et al.⁷ proposed IrO₂ on carbon paper as an anode in PEMWE using the electrodeposition (ED) method. The electrode revealed high performance (1010 mA·cm⁻² at 1.6 V) and reduced metal loading (0.1 mg·cm⁻²), thereby exhibiting the highest mass activity reported to date. It was attributed to improvements in the catalytic utilization. However, the electrode structures are composed of IrO₂ film on a porous substrate (carbon paper), not a porous IrO₂ electrode. Thus, a new design of a catalyst layer with a porous IrO₂ electrode is proposed to improve the utilization of catalyst and maximize mass activity, leading to the reduction of

catalyst loading and thereby decreasing the PEMWE cost.

An inverse-opal structure is a structure that comprises ordered and interconnected pores.⁸ The structure is used in various applications including sensors,^{9,10} solar cells,¹¹⁻¹³ lithium-ion batteries,^{14,15} and fuel cells.^{16,17} In a previous study, an inverse-opal structure was applied in a cathode of polymer electrolyte membrane fuel cells (PEMFCs) to enhance the mass transport of the reactant and produced water.¹⁷ The platinum (Pt) inverse-opal was directly prepared on a gas diffusion layer (GDL). The PEMFC with an inverse-opal structure exhibited high performance due to structural characteristics including high porosity, catalyst utilization, and efficient mass transport. However, the fabrication method reported in the study reveals low reproducibility since the substrate used has a rough surface.

In order to increase the reproducibility of preparing the inverse-opal electrode, a flat substrate should be used. In the ED method, the uniform distance between working electrode (substrate) and counter electrode is essential to prepare a uniform electrode since it is associated with ohmic resistance, which in turn leads to the applied voltage. In other words, the flat surface of substrate maintains a constant distance. However, no component in the MEA of PEMFC is used as a flat substrate. Therefore, an external substrate should be added in the fabrication method by using the transfer method instead of the direct application. David et al.¹⁸ and Mihi et al.¹⁹ proposed a transfer method by using a sacrificing layer to transfer the inverse-opal electrode. The sacrificing layer easily separates the electrode to be obtained with substrate when it is removed by using an etchant. Unfortunately, the inverse-opal electrode used in the study is too thin to allow for direct transfer without the protective layer. In order to transfer the entire inverse-opal electrode on membrane, we applied the decal method that is commercially used to fabricate the MEA of fuel cells^{20,21} to the modified transfer method. The decal method is the MEA fabrication method that uses additional substrates, such as Teflon film, to

prepare the electrode, and this is followed by transferring the electrode on membrane by hot-pressing.²² Given the aforementioned method, we selected hot-pressing to attach the electrode to the membrane, and this improved the feasibility of transferring the complete inverse-opal electrode. Thus, the modified method is termed as ‘the decal-transfer method’. Overall, we proposed the decal-transfer method as a facile method to produce the inverse-opal MEA to overcome the disadvantages of the existing method.

In the study, we prepared IrO₂ inverse-opal MEA by using the decal-transfer method as opposed to direct fabrication in the PEMWE anode (Figure 3.1). The inverse-opal structure in anode provides high surface area due to high porosity, thereby increasing the utilization of catalyst. The IrO₂ inverse-opal electrode was fabricated by using pulse electrodeposition (ED). Furthermore, ED parameters, such as current and total number of cycles, were inspected to achieve the inverse-opal structure. Additionally, the decal-transfer method was first utilized to prepare inverse-opal MEA, thereby leading to the enhanced reproducibility of the process. In the inverse-opal MEA, ultra-low IrO₂ (0.001–0.03 mg·cm⁻²) was loaded by varying the total number of cycles of ED (80–160 k cycles). The inverse-opal MEA was evaluated by using a PEMWE single-cell test, electrochemical impedance spectroscopy (EIS), and a hydrogen flow meter. Additionally, the mass activity was calculated by using cell performance and loading of IrO₂ and compared with that in other studies reported to date.

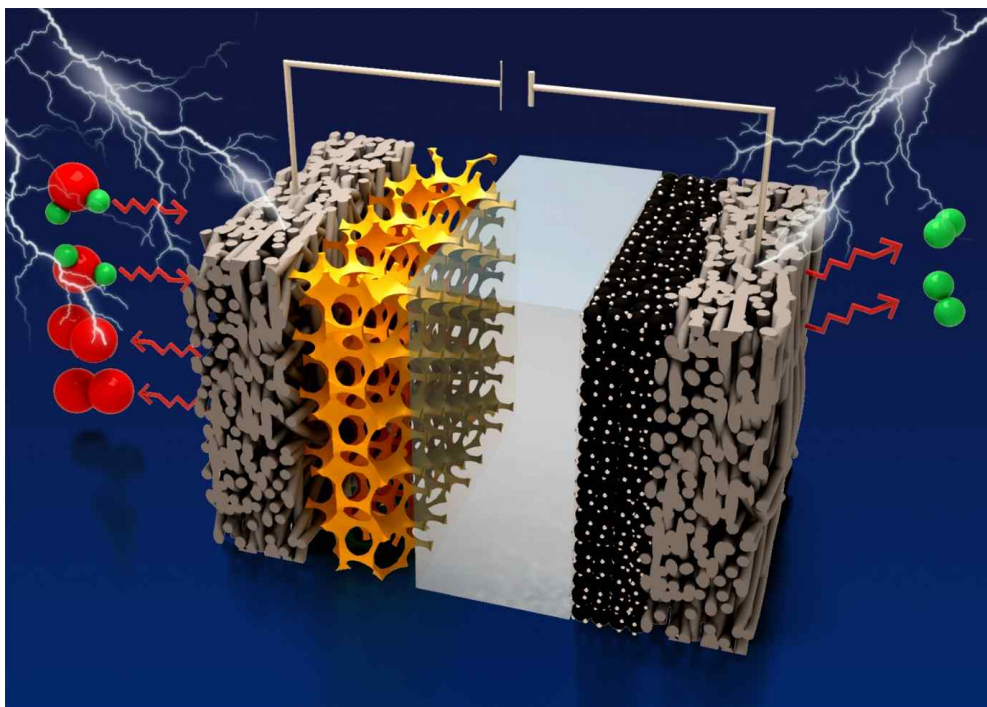


Figure 3.1. Schematic diagram of the single-cell of inverse-opal MEA.

3.2. Experimental section

3.2.1. Fabrication of IrO₂ inverse-opal electrode

Nickel (Ni) as the sacrificing layer was sputtered on fluorine-doped tin oxide (FTO) glass via the RF magnetron sputtering technique (150 W, 8 h). The sputtered substrate (Ni-FTO) was immersed in ethanol for 12 h to improve the adhesion between the polystyrene (PS) bead and substrate. The PS bead solution was prepared by using 2.0 g of PS suspension (Alfa Aesar Co., USA), 180 mg of 1 wt.% non-ionic surfactant solution (IGEPAL Co-30, Sigma Aldrich Co., USA), and 80 ml of distilled water. The treated substrates were soaked in the PS solution, and dried at 70 °C for 2 h to prepare the PS on substrate. In order to fabricate the IrO₂ inverse-opal electrode, PS on substrate was performed via the pulse ED method with a three-electrode cell. The PS on substrate, Pt mesh (Alfa Aesar, USA), and Ag/AgCl electrode were used as the working electrode, counter electrode, and reference electrode, respectively. The ED solution consisted of 10 mM iridium chloride hydrate, 100 mM potassium chloride, and distilled water. The ED condition corresponded to a current of 10 mA, on/off time of 50/300 ms, and total number of cycles corresponding to 140 k. Following the ED, the PS beads were removed by using toluene, thereby leading to the IrO₂ inverse-opal electrode.

3.2.2. Fabrication of inverse-opal MEA and conventional MEA

In order to transfer the inverse-opal electrode on membrane, the prepared electrode (anode) and membrane were attached by hot-pressing (120 °C, 1 MPa, 10 min). Nafion 212 (Dupont Co., USA) was used as the membrane. Following the hot-pressing, the attached electrode and membrane were immersed in 50 v. % nitric acid solution for 12 h to dissolve the sacrificing layer (Ni). Subsequently, the cathode catalyst layer was fabricated by using the spraying method. The catalyst slurry was prepared by using 40 wt% Pt/C (Johnson Matthey, UK), Nafion ionomer

(Dupont Co., USA) with content of 30 wt.%, isopropyl alcohol, and deionised water. The cathode catalyst loading corresponded to $0.4 \text{ mg}\cdot\text{cm}^{-2}$. The inverse-opal MEA was then prepared, as shown in Figure 3.1. Figure 3.1 presents the schematic of the inverse-opal MEA with the inverse-opal electrode as the anode catalyst layer, polymer electrolyte membrane, cathode catalyst layer, and the two gas diffusion layers (GDLs). In contrast, conventional MEA with a different anode catalyst layer was prepared using the spraying method. The catalyst layer consisted of IrO_2 (Alfa Aesar Co., USA), Nafion ionomer with a content of 10 wt.% of IrO_2 , isopropyl alcohol, and deionized water. The anode catalyst loading was $0.02 \text{ mg}\cdot\text{cm}^{-2}$. The geometric areas of two MEAs were equal to 5 cm^2 .

3.2.3. Physical characterizations

Field-emission scanning electron microscopy (FE-SEM; SUPRA 55VP, Carl Zeiss, Germany) was used to examine the morphology (top and cross-section views) of the electrodes. The shell thickness of inverse-opal electrodes was measured using transmission electron microscope (TEM; Tecnai F20 at KEPCO, USA). Additionally, X-ray diffraction (XRD) spectra of the samples were acquired by using an X-ray diffractometer (D/MAX-2500/PC, Rigaku Co., Japan). Furthermore, X-ray photoelectron spectroscopy (XPS) was conducted to analyse the composition of IrO_2 electrode. The IrO_2 loadings with respect to the total number of cycles were measured by inductively coupled plasma-mass spectroscopy (ICP-MS, NexION 350D, Perkin-Elmer, USA) installed at the National Center for Inter-university Research Facilities (NCIRF) at Seoul National University. The inverse-opal MEA was dissolved in aqua regia at $200 \text{ }^\circ\text{C}$ for 24 h to determine the IrO_2 loading using ICP-MS.

3.2.4. Electrochemical characterizations

The effect of inverse-opal electrodes obtained with respect to the total number of cycles was examined by using cyclic voltammetry (CV) in the 0.1 M HClO₄ solution from 0.4 to 1.25 V (vs. saturated calomel electrode (SCE)). Inverse-opal MEAs with different number of cycles corresponding to 80 k, 120 k, 140 k, and 160 k were denoted as 80k, 120k, 140k, and 160k. In order to measure the PEMWE performance, titanium and graphite bipolar plates were utilized as the anode and cathode current collector, respectively. A carbon-based GDL (JNTG40-A3, JNTG Co., KOREA) was applied as GDLs in both electrodes. The cell temperature was maintained at 90 °C. The reactants were preheated to 50 °C and supplied to the anode side with a flow rate of 1 ml·min⁻¹. The cell performance was evaluated via the voltage sweep method from 1.25 to 2.05 V at 2 mV·s⁻¹. The stability test was evaluated with the constant voltage method at 1.6 V and 1.9 V for a period of 1200 s using the same operating conditions. The CV of inverse-opal MEA and conventional MEA was evaluated with voltage ranging from – 0.05 to 1.5 V to compare the electrochemical surface area of two MEAs. Nitrogen and hydrogen were supplied to the anode and cathode, respectively. Furthermore, EIS (ZAHNER-Elektrik GmbH & Co. KG, Germany) was performed to examine the resistance of inverse-opal MEA at a constant voltage of 1.6 V with an amplitude of 50 mV. The frequency ranged from 100 MHz to 100 kHz. A customized flow meter was utilized to measure the flow rate of hydrogen generated in the cathode side.

3.3. Results and Discussion

3.3.1. Decal-transfer method

Figure 3.2 shows the photographs of preparing inverse-opal MEA by using the decal-transfer method. The decal transfer method was applied in PEMWE to increase reproducibility of fabrication of inverse-opal electrode by using the substrate that exhibits flat surface. The method consisted of four main steps as follows: (i) the fabrication of the inverse-opal electrode, (ii) the attachment of the electrode on the membrane by using hot-pressing, (iii) the removal of the sacrificing layer, and (iv) the fabrication of the cathode by spraying. Figure 3.3 presents the SEM images of each step in the decal-transfer method. First, the IrO₂ inverse-opal electrode was fabricated by pulse ED method. Ni-FTO was used as the substrate. In order to transfer the prepared electrode in membrane, the sacrificing layer (which is the layer removed by using etching solution^{23,24}) should be added in the substrate. Specifically, Ni is a suitable material that can be removed by using HNO₃ solution without damaging the membrane and IrO₂ electrode (Figure 3.4).²⁵ Polystyrene (PS) beads that were used as a template to construct macropores in the electrode were self-assembled in the Ni-sputtered substrate (Figure 3.3a). Subsequently, voids formed by the template were filled with IrO₂ catalyst by using pulse ED (Figure 3.3b), and this is discussed in following paragraph. Additionally, the template was removed by using toluene, thereby resulting in an inverse-opal electrode (Figure 3.3c). Second, the prepared electrode was transferred to the membrane to fabricate the inverse-opal MEA. In order to transfer the complete area of electrode, the inverse-opal electrode was attached to the membrane via hot-pressing at high temperature. Following the attachment, the sacrificing layer was removed by using the HNO₃ solution. By using the method, the electrode was easily separated on the substrate. Then, inverse-opal electrode was transferred on membrane preparing anode catalyst layer. Finally, the cathode catalyst layer was

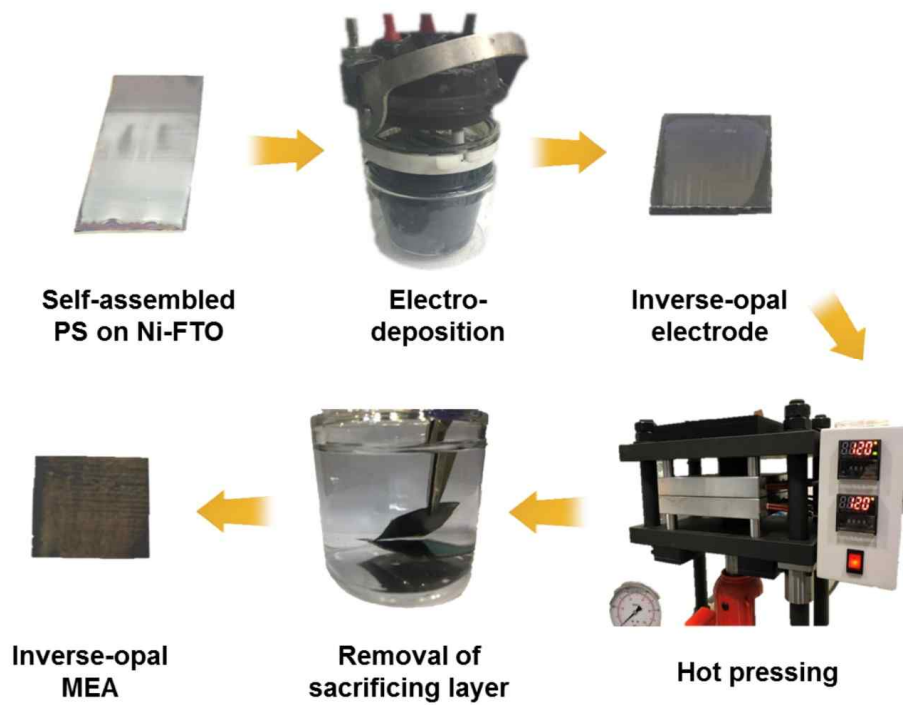


Figure 3.2. Photographs of each step in the decal-transfer method for inverse-opal MEA.

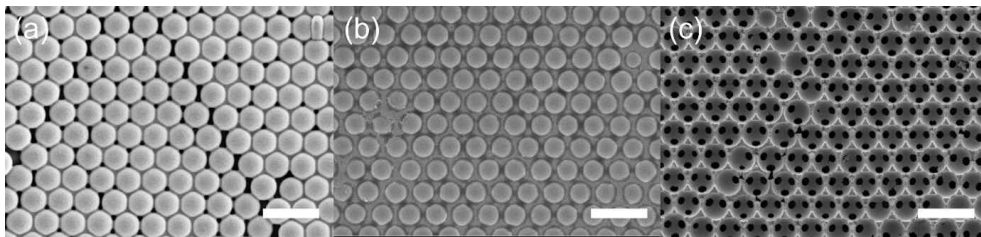


Figure 3.3. FE-SEM images of each step in the decal-transfer method: (a) self-assembled PS beads as template, (b) infiltration of IrO₂ by using pulse electrodeposition, and (c) inverse-opal electrode. The scale bar is 1 μm.

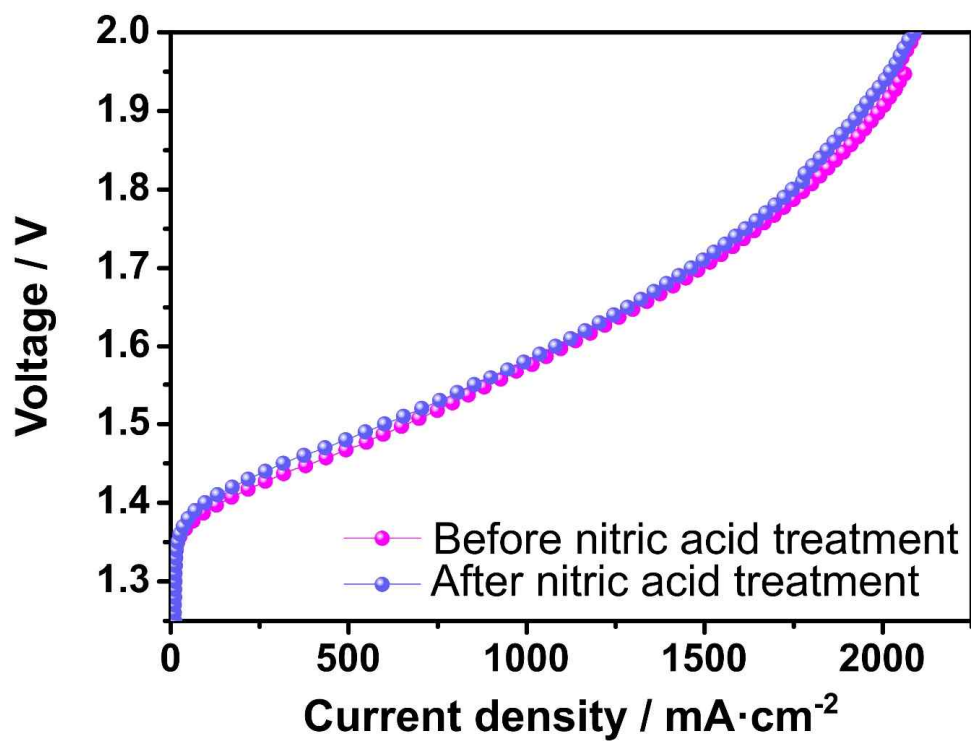


Figure 3.4. Polarization curves of conventional MEA before and after nitric acid treatment.

fabricated via spraying in other sides of the membrane, thereby resulting in the inverse-opal MEA.

3.3.2. Fabrication and characterization of IrO₂ inverse-opal electrode

The pulse ED method (which corresponds to the ED with on/off time) was applied to prepare the inverse-opal electrode. Introduction of the off time induced high uniformity of the electrode by supplying the precursor ions in the surface. To attain the inverse-opal electrode, the ED conditions (i.e. current and total number of cycles) were investigated. First, various applied currents were examined. In electrodeposition, the morphology of electrode varies with the applied current.^{26,27} It was important to determine the optimal current that can infiltrate the IrO₂ into the voids formed by self-assembled PS beads. Figure 3.5 shows the SEM images of inverse-opal electrodes with differences in the applied currents (5, 10, 20, and 30 mA). The electrodes exhibited different morphologies when they were prepared with variations in the applied currents, and this was attributed to the differences in the voltages applied in electrodes (Figure 3.6). It was proposed that the voltage curve achieved at the current of 10 mA was suitable to fabricate the inverse-opal electrode. Thus, the optimized current was determined as 10 mA.

Additionally, different total number of cycles (80 k, 120 k, 140 k, and 160 k cycles) were examined to obtain inverse-opal electrodes with different IrO₂ loadings. The total cycle was associated with the charge applied in electrode, and thereby the catalyst loading. That is, the catalyst loading increased with increases in the number of total cycles. As shown in Figure 3.7, all samples with different total number of cycles exhibited a porous structure. In the case of 80 k, a thin inverse-opal electrode (approximately 0.5 layer) was prepared. As the number of cycles increased from 80 k to 140 k, the complete inverse-opal electrode was formed via the infiltration of IrO₂ into the voids. Conversely, with respect to higher

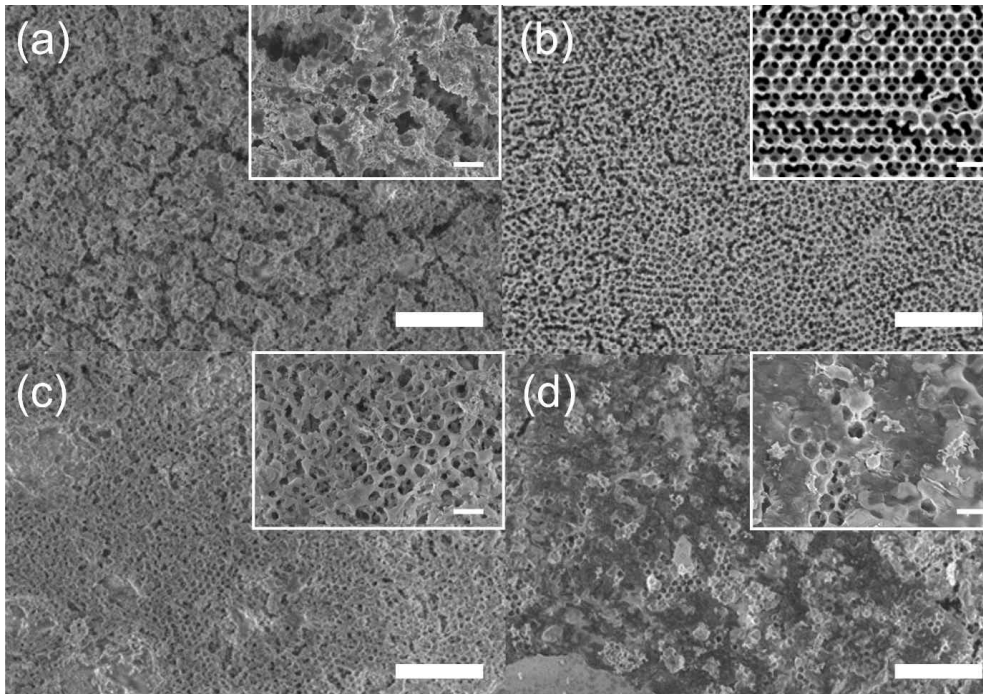


Figure 3.5. FE-SEM images of inverse-opal electrode obtained with different current of (a) 5, (b) 10, (c), 20, and (d) 30 mA. The scale bar is 5 μm and 1 μm , respectively.

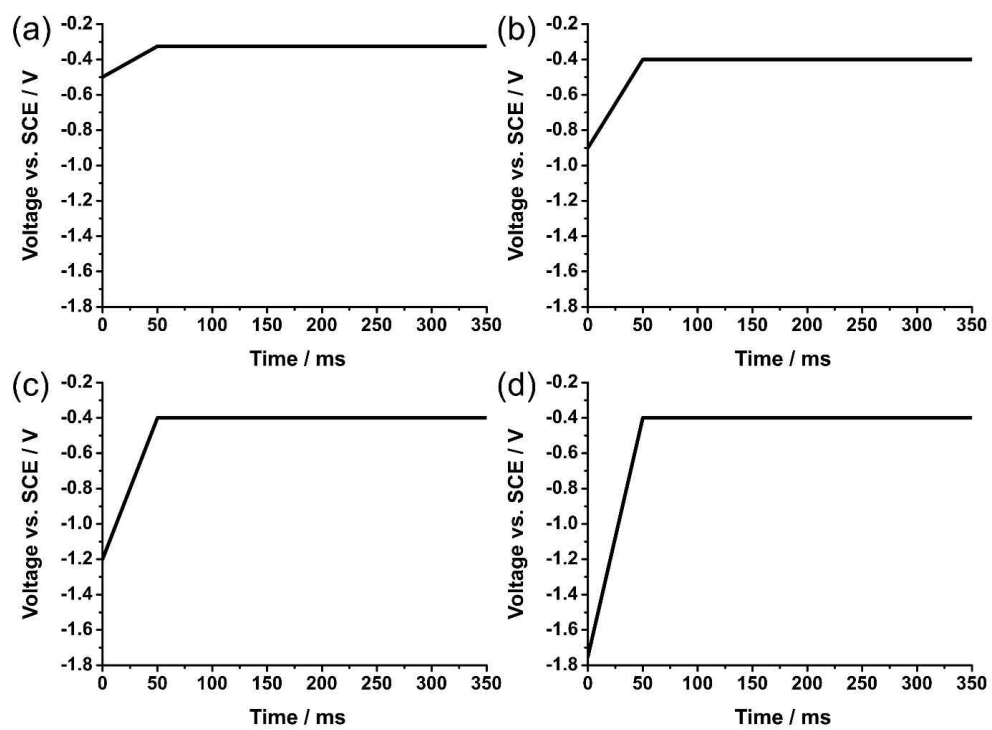


Figure 3.6. Voltage curves of electrodes obtained with different current of (a) 5, (b) 10, (c), 20, and (d) 30 mA.

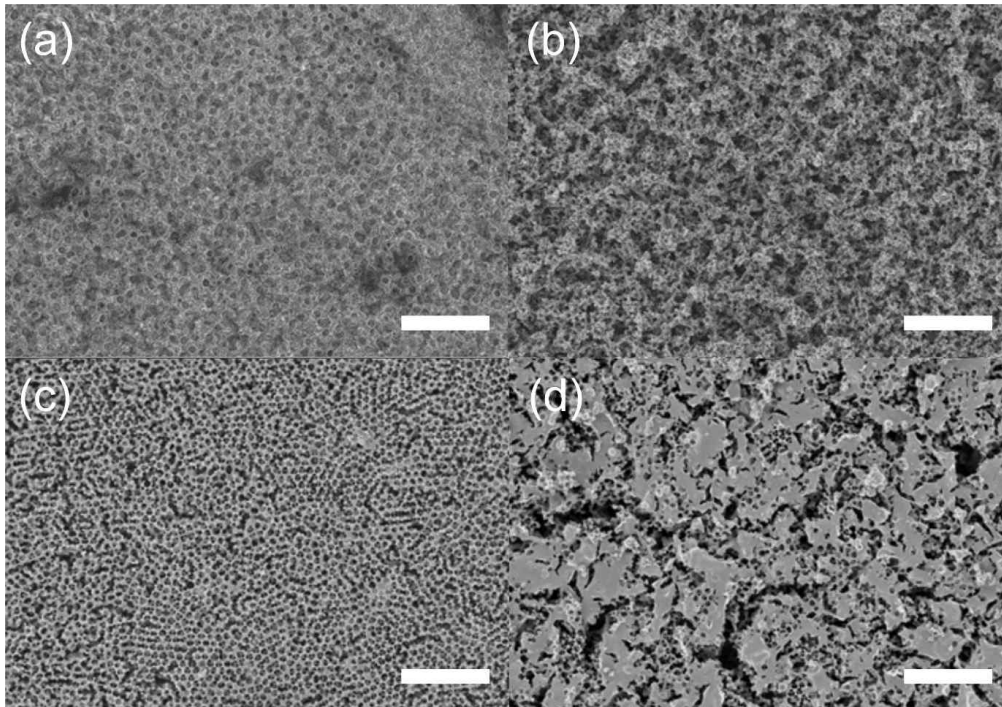


Figure 3.7. FE-SEM images of inverse-opal electrode with variations in the total number of cycles (a) 80 k, (b) 120 k, (c) 140 k, and (d) 160 k cycles. The applied current is 10 mA. The scale bar is 5 μm .

number of cycles corresponding to 160 k, the IrO₂ plate covered on inverse-opal electrode was observed due to the excessive amount of applied charge. Overall, the optimal number of total cycles to attain the electrode with the inverse-opal structure was found to be 140 k. Furthermore, several electrodes were fabricated for the reproducibility test of the fabrication method. As shown in Figure 3.8, the electrodes also exhibited the inverse-opal structure, thereby indicating that the decal-transfer method is reproducible in terms of preparing the inverse-opal electrode.

Figure 3.3c and Figure 3.9 respectively show the SEM and TEM images of the inverse-opal electrodes which are prepared with the use of optimized ED conditions (current of 10 mA and total cycle numbers of 140 k). The inverse-opal electrode had a three-dimensional ordered pore structure that consisted of macropores with diameters equal to 500 nm. The IrO₂ shell thickness was in the range of 10–30 nm, as shown in Figure 3.9b. Inverse-opal MEAs with different number of cycles corresponding to 80 k, 120 k, 140 k, and 160 k were denoted as 80k, 120k, 140k, and 160k. The catalyst loading of inverse-opal MEAs was confirmed by using ICP-MS. The IrO₂ loadings of inverse-opal MEA were 0.001, 0.01, 0.02, and 0.03 mg·cm⁻² with respect to the number of cycles corresponding to 80 k, 120 k, 140 k, and 160 k, respectively.

We compared the amount of IrO₂ measured using ICP-MS and the theoretically estimated value with the use of the void space and thickness of PS. We calculated the ratio between the empty and full spaces inside the inverse opal structure.¹⁷ It was assumed that the IrO₂ maintained a hexagonal close-packed structure (*hcp*) structure or as a face-centered cubic (*fcc*) structure with an atomic packing factor (APF) of 0.74. The theoretical IrO₂ mass in the inverse-opal electrode can be calculated as,

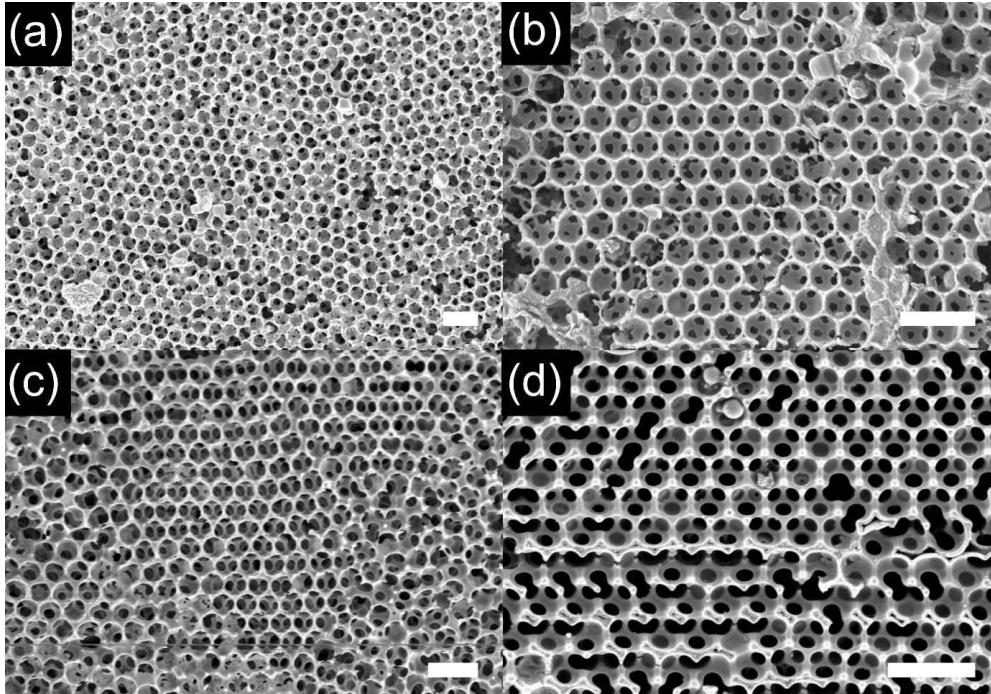


Figure 3.8. FE-SEM images of several inverse-opal electrodes obtained with the optimal ED conditions. The scale bar is 1 μm .

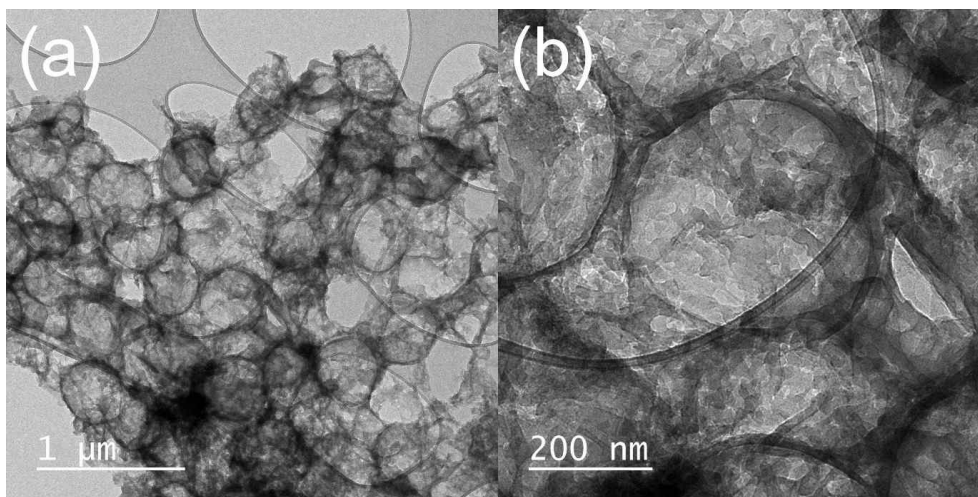


Figure 3.9. TEM images of inverse-opal electrode

$$\begin{aligned}
\text{Mass}_{\text{inverse-opal electrode}} &= \text{Volume}_{\text{total}} \times (1 - \text{APF}) \times \rho_{\text{IrO}_2} \\
&= \{5 \text{ cm}^2 \cdot 0.5 \text{ }\mu\text{m} \times (1 - 0.74)\} \times 11.66 \text{ g cm}^{-3} \\
&= 0.76 \text{ mg}
\end{aligned}$$

where ρ is the density of IrO₂. Therefore, if all the empty spaces between the PS spheres were filled with IrO₂, the amount of IrO₂ of the inverse-opal MEA was approximately 0.15 mg cm⁻², but the actual amount of IrO₂ was only approximately 0.02 mg cm⁻² according to the ICP-MS measurement. Thus, the ratio between the empty and full spaces inside the inverse opal structure is approximately equal to 13.33%, which is almost the equal to the corresponding ratio in the case of the Pt inverse-opal electrode (14.36%), as reported previously.¹⁷ The calculated surface ratio from the amount of IrO₂ measured and theoretically estimated from the density was approximately 13.33%.

XRD and XPS analyses were conducted to identify the composition of the prepared samples. Figure 3.10 shows the XRD spectra of each step in the decal-transfer method as follows: FTO, Ni-FTO, and the inverse-opal electrode. The XRD spectra confirm that Ni-FTO consists of Ni, thereby revealing the diffraction peaks of Ni (JCPDS 65-2865). Additionally, the inverse-opal electrode exhibited diffraction patterns indexing IrO₂, thus yielding peaks indexed to the (110) and (200) planes (JCPDS 15-0870). Also, the XPS spectra of the prepared inverse-opal electrode showed that the two peaks at approximately 62.2 and 65.5 eV were observed (Figure 3.11). The peaks were reported as 4f_{7/2} and 4f_{5/2}, respectively of IrO₂,^{7,28} thereby indicating that the IrO₂ electrode was well developed. The CV curves of inverse-opal electrode with different cycles corresponding to 80 k, 120 k, 140 k, and 160 k are shown in Figure 3.12. The curves exhibited a typical shape of IrO₂ materials.^{29,30} The charge capacity associated with the integration of CV is related to the electrochemical surface area (ECSA).²⁹ Thus, the peak intensity increased with increases in the total number of cycles from 80 k to 160 k, thereby

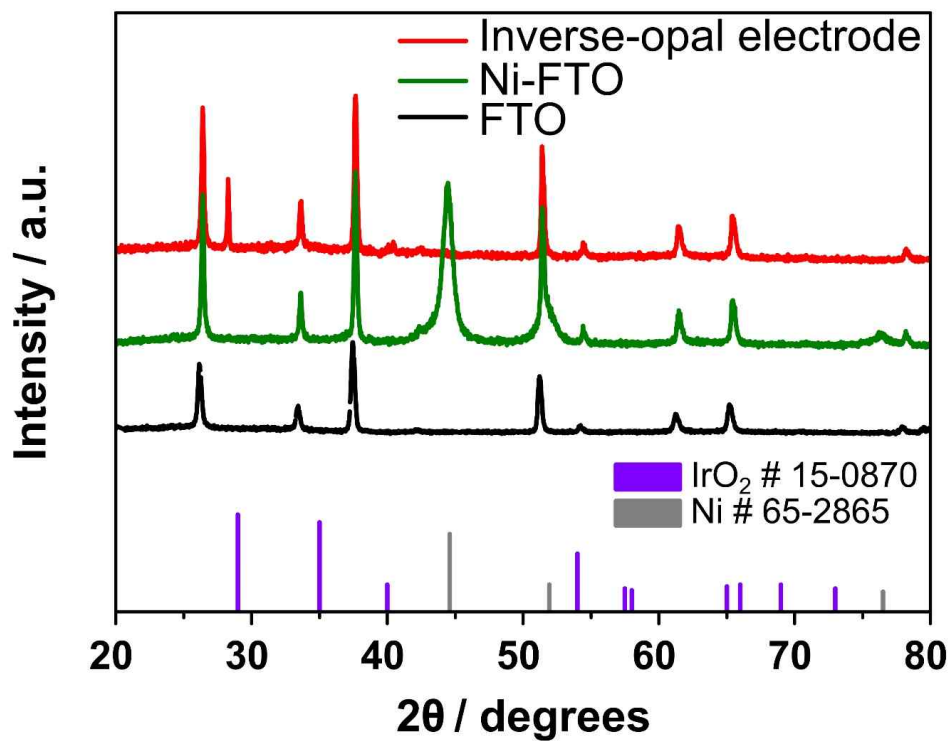


Figure 3.10. XRD patterns of FTO, Ni-FTO, and inverse-opal electrode.

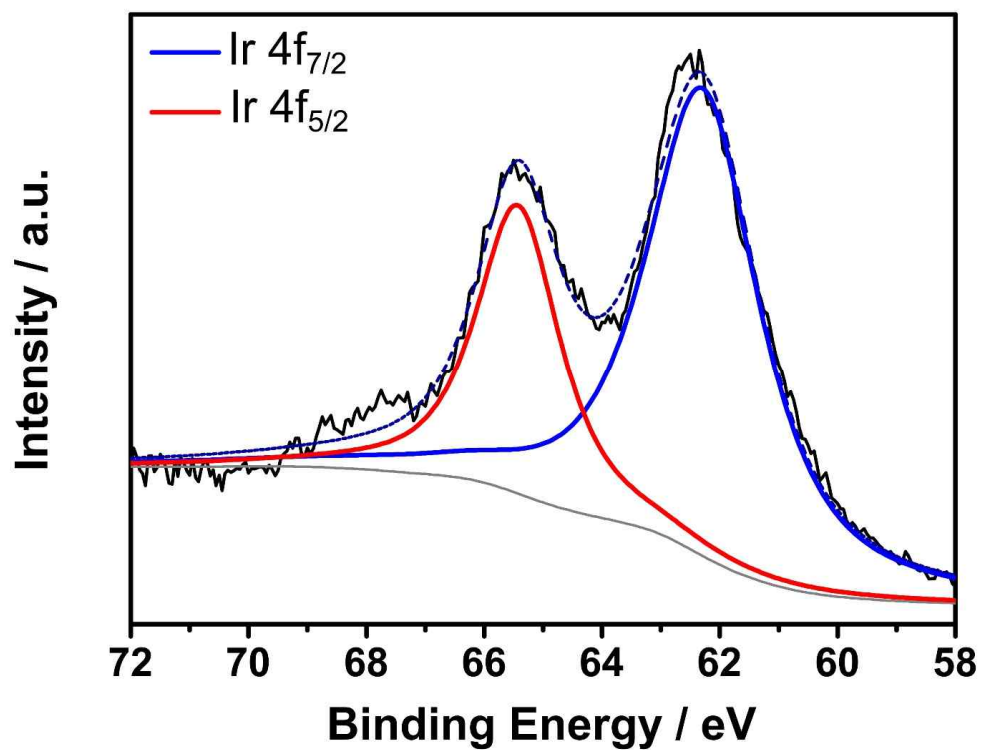


Figure 3.11. Ir 4f XPS spectra of IrO₂ inverse-opal electrode

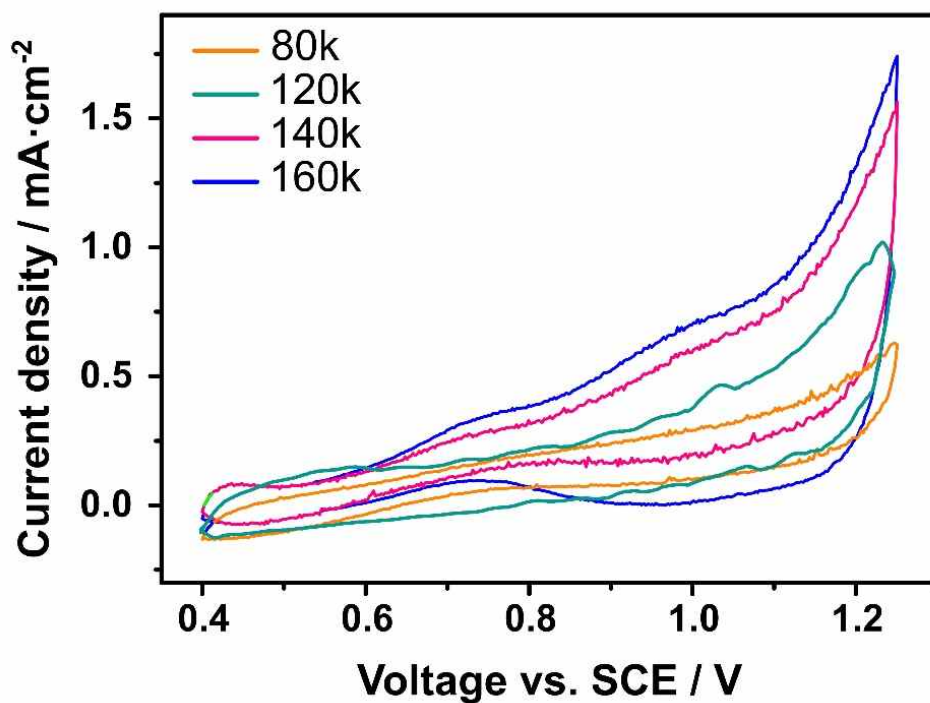


Figure 3.12. Cyclic voltammetry of inverse-opal MEA with different total cycles (80k, 120k, 140k, and 160k cycles)

confirming that the total number of cycles was related to the amount of IrO₂ loading.

3.3.3. Electrochemical characterizations of inverse-opal MEA

In order to achieve the optimal inverse-opal MEA, various MEAs were evaluated by using single cell test of PEMWE. Figure 3.13 and Figure 3.14 show the polarization curves of 80k, 120k, 140k, and 160k, and the comparison in cell performance of inverse-opal MEA. The 80k showed an extremely low performance because the IrO₂ loading is insufficient (0.001 mg·cm⁻²) as shown in Figure 3.7a. The performance rapidly increased with increases in the total number of cycles from 80 k to 140 k. It was attributed to increases in the number of active sites that resulted from the catalyst loading. Additionally, the cell performance at 1.6 V exhibited the highest value due to a fully formed inverse-opal structure. However, 160 k exhibited a performance lower than the number of cycles corresponding to 140 k. As shown in Figure 3.7d, a few covered IrO₂ films on inverse-opal electrode that exist between the catalyst layer and membrane partially block the generated proton transfer from the catalyst layer to the membrane. The phenomenon resulted in a relatively lower performance when compared to that for the number of cycles corresponding to 140 k. These results exhibited similar tendency with the study reported regarding inverse-opal electrode in alkaline electrolysis reported previously.³¹ In addition to alkaline water electrolysis, higher catalyst loading (surface area) yielded a limited cell performance enhancement owing to the blockage of proton and mass transfer. Thus, the optimal number of total cycles required to attain a high performance corresponded to 140 k.

To investigate the effect of electrode structure on cell performance, the inverse-opal MEA (140k) and conventional MEA were evaluated with same catalyst loading of 0.02 mg·cm⁻². Figure 3.15a shows the PEMWE performance of

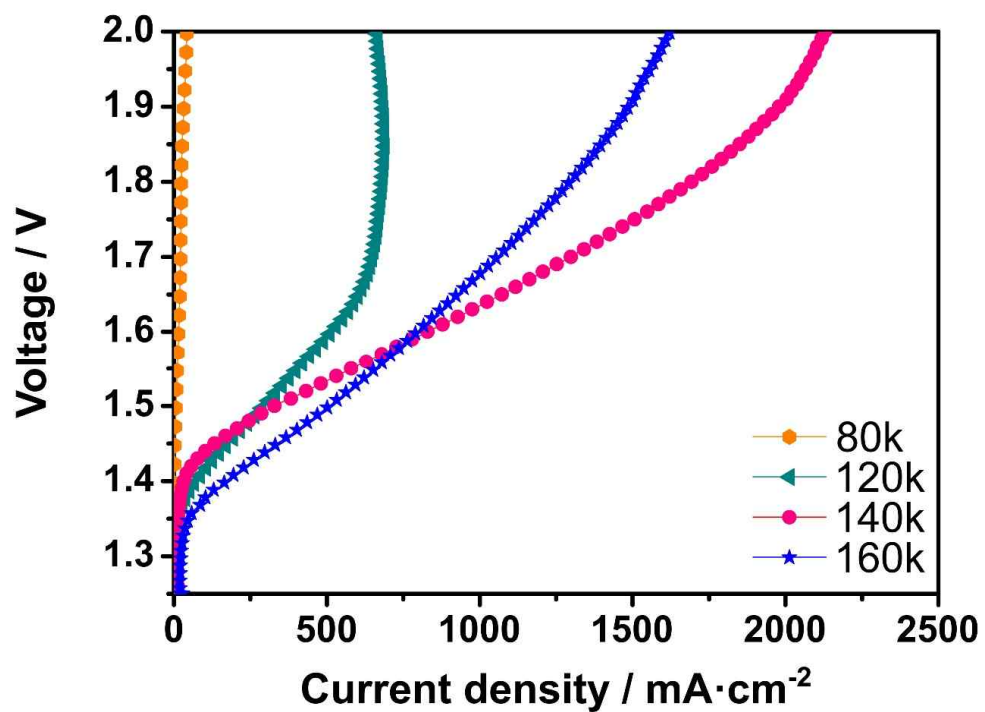


Figure 3.13. (a) Polarisation curves of inverse-opal MEAs with differences in the total number of cycles (80 k, 120 k, 140 k, and 160 k cycles).

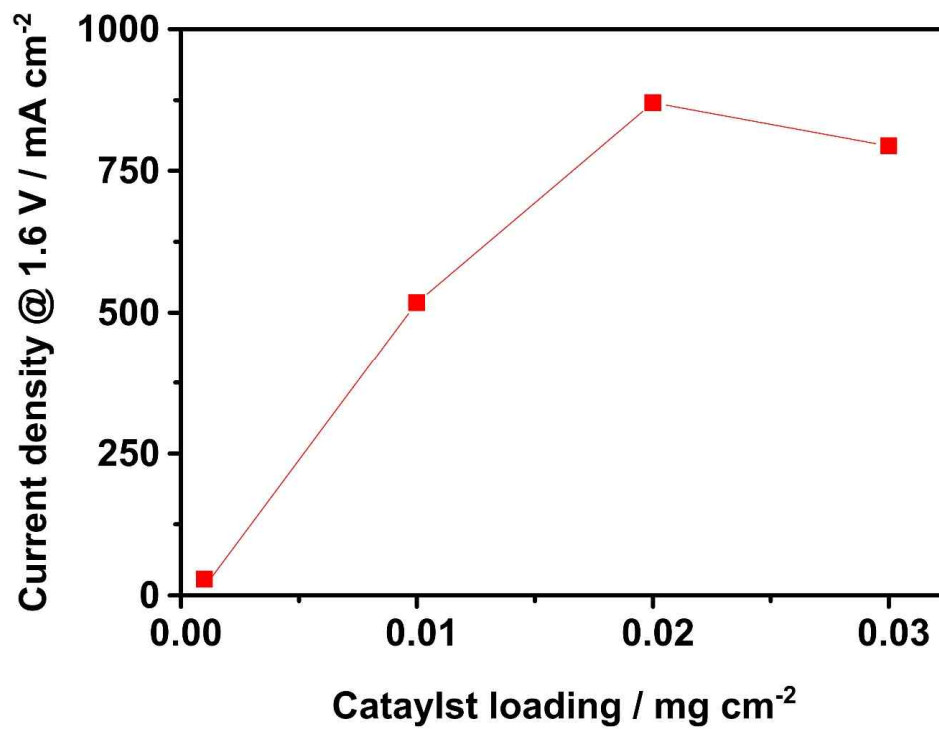


Figure 3.14. The performance changes of inverse-opal MEAs as a function of catalyst loading.

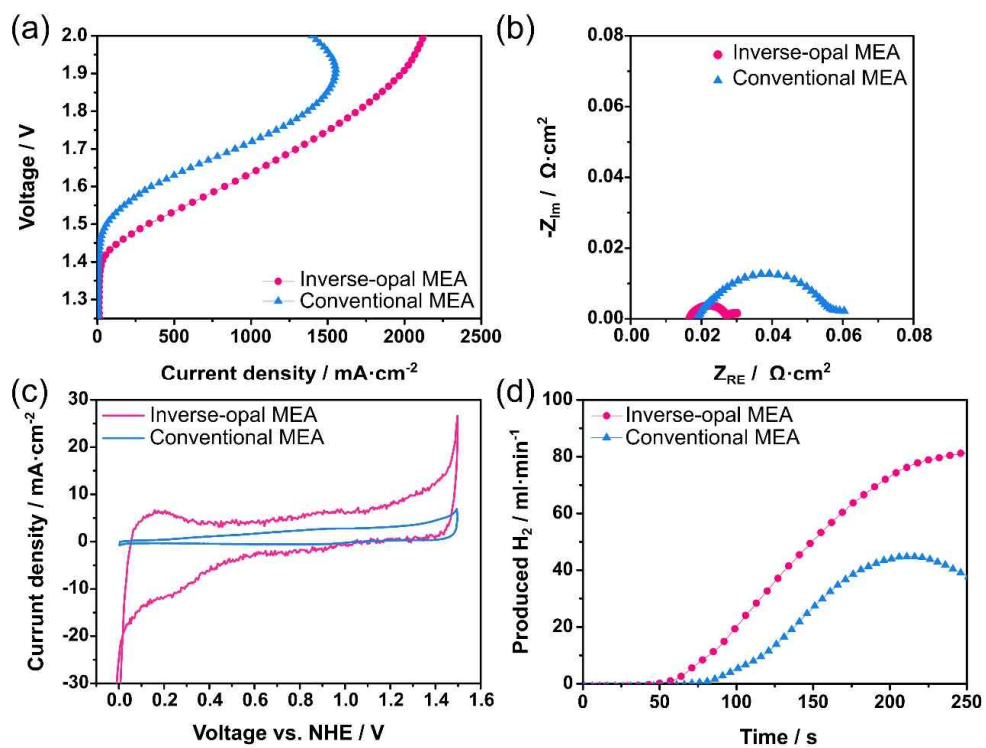


Figure 3.15. (a) PEMWE performance, (b) Nyquist plot at 1.6 V, (c) cyclic voltammetry, and (d) measured amount of generated hydrogen in the inverse-opal MEA and conventional MEA. The catalyst loading is 0.02 mg·cm⁻²

inverse-opal MEA and conventional MEA. The current density at 1.6 V of inverse-opal MEA was $870 \text{ mA}\cdot\text{cm}^{-2}$, and this was 2.5 times that of conventional MEA ($350 \text{ mA}\cdot\text{cm}^{-2}$). Additionally, the mass activity (which is the current density per catalyst loading) at 1.6 V of inverse-opal MEA was $43.5 \text{ A}\cdot\text{mg}^{-1}$. While the current density of conventional MEA decreased in the high-voltage region, reduction of performance was not observed in the inverse-opal MEA. This was attributed to the enhanced mass transport of the reactants and products. In the high-voltage region, the gases produced in the catalyst layer can cover the active area of the IrO_2 catalyst, and can thus lead to the reduction of the amount of the active area, and to a decrease in the performance. In contrast, the performance of the inverse-opal MEA did not decrease in the high-voltage region despite the fact that the same catalyst loading was used.

Additionally, the stability tests of the inverse-opal and conventional MEA were evaluated in low- (1.6 V) and high-voltage (1.9 V) regions. Figure 3.16 presents the current density of the two MEAs at the constant voltages of (a) 1.6 V and (b) 1.9 V for a period of 1200 s. As shown in Figure 3.16, conventional MEA elicits low stability with a significant current density loss. Conversely, inverse-opal MEA exhibits a stable performance at the low- and high-voltage regions despite its ultra-low loading of 0.02 mg cm^{-2} . This is attributed to its structural characteristics. Unlike the conventional electrode which consists of IrO_2 particles, the three-dimensional network IrO_2 structure in inverse-opal electrode is shown to be highly stable with the use of the PEMWE operating conditions.

In addition, as shown in Nyquist plots of two MEAs performed using EIS (Figure 3.15b), the inverse-opal MEA exhibits lower ohmic resistance (which corresponds to the high-frequency intercept in x-axis) when compared to that of conventional MEA. This indicates that the inverse-opal structure enhances the electron transfer due to its ordered and interconnected pores.^{32,33} This was also

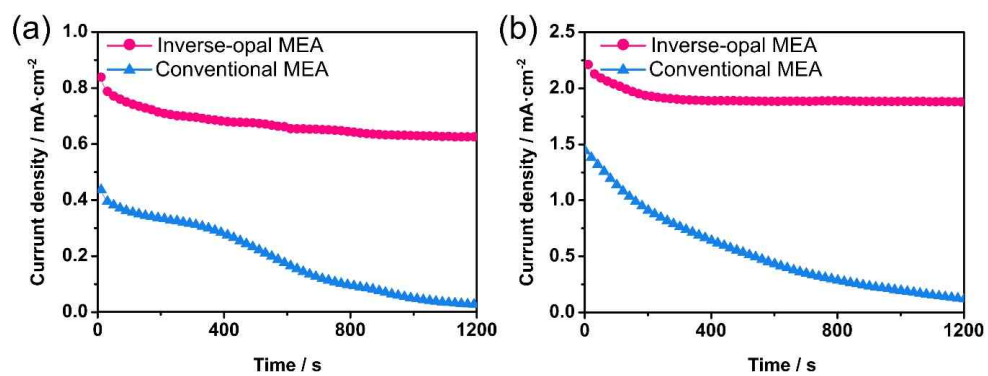


Figure 3.16. Stability test results of the inverse-opal MEA and conventional MEA in the (a) low-voltage (1.6 V) and (b) high-voltage (1.9 V) regions over a time period spanning 1200 s.

attributed to the direct fabrication of the inverse-opal electrode on the membrane.^{34,35} Furthermore, the charge-transfer resistance (which is the diameter of the semicircle) of inverse-opal MEA was smaller than that of conventional MEA. In contrast to the conventional MEA including micro- or meso-pores, the inverse-opal MEA exhibited macro-pores with a diameter of 500 nm, thereby leading to the efficient supply reactant to active sites of the catalyst. Additionally, Figure 3.15c shows the CV curves of inverse-opal MEA and conventional MEA. For iridium oxide materials, the ECSA cannot be measured using CV due to the ineffective hydrogen underpotential deposition and carbon monoxide oxidation.^{36,37} However, L. A da Silva et al.³⁷ reported that the voltammetric charge is proportional to the surface area. That is, ECSA of two MEAs can be estimated by comparing the voltammetric charge, which is the integration of CV.³⁸ Thus, the enhancement of the estimated ECSA of the catalyst that is confirmed by CV improved the utilization of the catalyst. Finally, Figure 3.15d presents the measured amount of generated hydrogen of two MEAs by using a flow-meter. The amount of produced hydrogen in the inverse-opal MEA exceeded that in conventional MEA, which was consistent with the results for a PEMWE single cell. Furthermore, the estimated cell performance that was calculated by using the measured amount of hydrogen was approximately similar to that in the real PEMWE performance (Figure 3.17). Therefore, the inverse-opal structure enhanced the cell performance since it improved electron transfer, efficient supply of the reactant, and surface area of the catalyst.

Figure 3.18 shows the SEM images of inverse-opal MEA and conventional MEA when prepared with the same loading of $0.02 \text{ mg}\cdot\text{cm}^{-2}$. As shown in Figure 3.18a and d, the thickness of inverse-opal MEA and conventional MEA were approximately 500 nm and 100 nm, respectively. This indicated that porous structure in inverse-opal MEA enhanced the surface area of catalyst. Additionally,

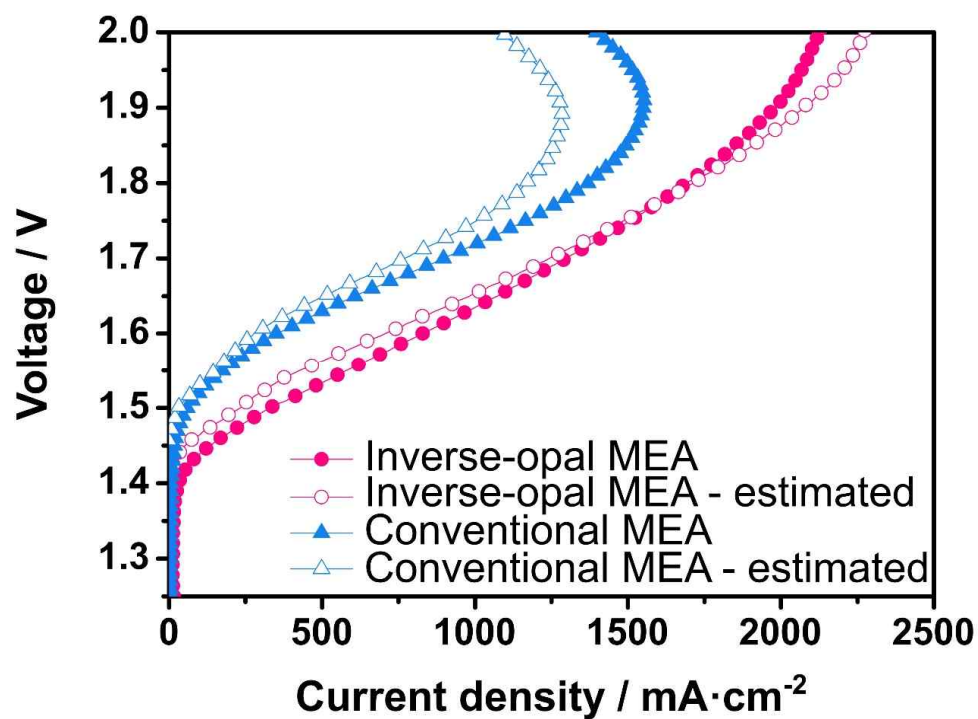


Figure 3.17. PEMWE performance (solid) and estimated performance by measured amount of generated hydrogen (open) of inverse-opal MEA and conventional MEA. The catalyst loading was 0.02 mg·cm⁻²

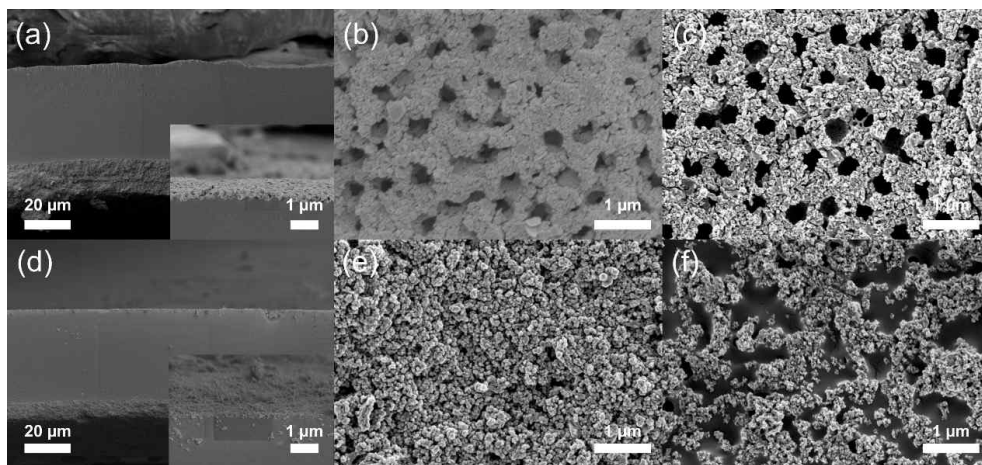


Figure 3.18. FE-SEM images of (a-c) inverse-opal electrode and (d-f) conventional electrode: (a, d) cross-sectional view, and top view (b, e) before stability test and (c, f) after stability test.

the larger pores (500 nm) in catalyst layer of inverse-opal MEA were formed when compared to that in the conventional MEA (10-50 nm). The pores with a diameter of 500 nm in inverse-opal MEA led to improvements in the efficient supply of reactant and removal of product, and surface area. Moreover, the inverse-opal electrode before and after the stability test showed similar morphologies, as shown in Figure 3.18b and c.

Figure 3.19 and Table 3.1 present a comparison of cell performances and mass activities achieved in the study and that reported in extant studies including the IrO₂ catalyst in the anode.^{2,4-7,39,40} In contrast to previous studies that examine the IrO₂ catalyst, the loading of the inverse-opal MEA was ultra-low (0.02 mg·cm⁻²). In addition, the performance at 1.6 V was 870 mA·cm⁻², which was higher than or comparable to that in other studies (Figure 3.19a). Furthermore, the mass activity of inverse-opal MEA is the highest as shown in Figure 3.19b. This indicates that the inverse-opal electrode design exhibited high PEMWE performance despite its ultra-low loading, which was due to the enhanced utilization of the IrO₂ catalyst.

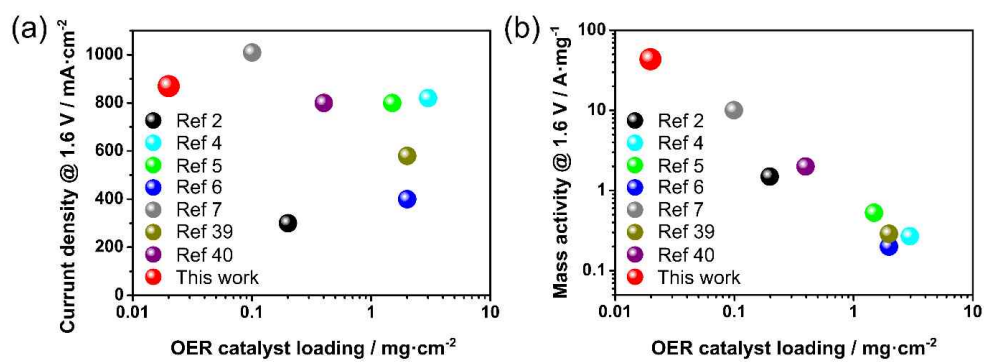


Figure 3.19. Comparison of (a) cell performances (current density at 1.6 V) and (b) mass activities at 1.6 V achieved in the study and those reported in extant studies.^{2,4-7,39,40}

Table 3.1. The summary of catalyst loading, cell performance, mass activity of some reported IrO₂ catalyst in PEMWE

Catalyst	Catalyst loading (mg·cm ⁻²)	Cell performance at 1.6 V (A·cm ⁻²)	Mass activity at 1.6 V (A·mg ⁻¹)	Reference
IrO ₂ inverse-opal	0.02	0.87	43.5	This study
Sputtered IrO ₂ film	0.2	0.3	1.5	Electrochim. Acta, 2007, 52, 3889
IrO ₂ prepared by chemical reduction	3	0.82	0.27	Int. J. Hydrogen Energy, 2008, 33, 4955
IrO ₂ with zeolite template	1.5	0.8	0.53	ChemSuschem, 2012, 5, 858
Antimony doped tin oxide supported IrO ₂	2	0.4	0.2	J. Power Soc. 2014, 269, 451
Electrodeposited IrO ₂ electrode	0.1	1.01	10.1	Appl. Catal. B, 2015, 179, 285
Combustion synthesized IrO ₂	2	0.58	0.29	J. Mater. Chem. A, 2017, 5, 4774
Nano-sized IrO ₂	0.4	0.8	2	J. Power Soc. 2017, 366, 105

3.4. Conclusions

In this study, the IrO₂ inverse-opal MEA was proposed in PEMWE to reduce the catalyst loading, and thereby enhancing the utilization of the catalyst. The inverse-opal MEA was easily fabricated with high reproducibility by using the decal-transfer method that combines transfer method with the decal method. The ED parameters including the applied current and total cycle were investigated to optimize the inverse-opal structure. Although the catalyst loading was ultra-low (0.02 mg·cm⁻²), the inverse-opal MEA exhibited an excellent performance of 870 mA·cm⁻² at 1.6 V, and this was 2.5 times that of conventional MEA. Furthermore, the mass activity of inverse-opal MEA exhibited the highest value (43.5 A·mg⁻¹) that is reported to date. It was ascribed to the improvements in the electron transfer and surface area of the inverse-opal structure that resulted in increases in the utilization of the catalyst, and thereby reducing the IrO₂ loading. Overall, the new design including inverse-opal structure corresponds to a promising catalyst layer in PEMWE.

3.5. References

1. A. T. Marshall, S. Sunde, M. Tsyarkin, R. Tunold, Performance of a PEM water electrolysis cell using $\text{Ir}_x\text{Ru}_y\text{Ta}_z\text{O}_2$ electrocatalysts for the oxygen evolution electrode, *Int. J. Hydrogen Energy* 2007, **32**, 2320-2324.
2. S. Song, H. Zhang, X. Ma, Z. Shao, R. T. Baker, B. Yi, Electrochemical investigation of electrocatalysts for the oxygen evolution reaction in PEM water electrolyzers, *Int. J. Hydrogen Energy* 2008, **33**, 4955-4961.
3. J. Cheng, H. Zhang, G. Chen, Y. Zhang, Study of $\text{Ir}_x\text{Ru}_{1-x}\text{O}_2$ oxides as anodic electrocatalysts for solid polymer electrolyte water electrolysis, *Electrochim. Acta* 2009, **54**, 6250-6256.
4. V. K. Puthiyapura, M. Mamlouk, S. Pasupathi, B. G. Pollet, K. Scott, J. Physical and electrochemical evaluation of ATO supported IrO_2 catalyst for proton exchange membrane water electrolyser, *J. Power Sources* 2014, **269**, 451-460.
5. M. G. Chourashiya, A. Urakawa, Solution combustion synthesis of highly dispersible and dispersed iridium oxide as an anode catalyst in PEM water electrolysis, *J. Mater. Chem. A* 2017, **5**, 4774-4778.
6. E. Slavcheva, I. Radev, S. Bliznakov, G. Topalov, P. Andreev, E. Budevski, Sputtered iridium oxide films as electrocatalysts for water splitting via PEM electrolysis, *Electrochim. Acta* 2007, **52**, 3889-3894.
7. B. S. Lee, S. H. Ahn, H. Y. Park, I. Choi, S. J. Yoo, H. J. Kim, D. Hakensmeier, J. Y. Kim, S. Park, S. W. Nam, K. Y. Lee, J. H. Jang, Development of electrodeposited IrO_2 electrodes as anodes in polymer electrolyte membrane water electrolysis, *Appl. Catal. B: Environ.* 2015, **179**, 285-291.
8. A. Stein, B. E. Wilson, S. G. Rudisill, Design and functionality of colloidal-crystal-templated materials--chemical applications of inverse

- opals, *Chem. Soc. Rev.* 2013, **42**, 2763-2803.
9. H. Li, J. Wang, L. Yang, Y. Song, Superoleophilic and superhydrophobic inverse opals for oil sensors, *Adv. Funct. Mater.* 2008, **18**, 3258-3264.
 10. I. B. Burgess, L. Mishchenko, B. D. Hatton, M. Kolle, M. Lončar, J. Aizenberg, Encoding complex wettability patterns in chemically functionalized 3D photonic crystals, *J. Am. Chem. Soc.* 2011, **133**, 12430-12432.
 11. A. Mihi, M. E. Calvo, J. A. Anta, H. Míguez, Spectral response of opal-based dye-sensitized solar cells, *J. Phys. Chem. C* 2008, **112**, 13-17.
 12. T. Suezaki, P. G. O' Brien, J. I. L. Chen, E. Loso, N. P. Kherani, G. A. Ozin, Tailoring the electrical properties of inverse silicon opals - a step towards optically amplified silicon solar cells, *Adv. Mater.* 2009, **21**, 559-563.
 13. D.-Y. Kang, Y. Lee, C.-Y. Cho, J. H. Moon, Inverse opal carbons for counter electrode of dye-sensitized solar cells, *Langmuir* 2012, **28**, 7033-7038.
 14. D.-Y. Kang, Y. Lee, C.-Y. Cho, J. H. Moon, Highly ordered three-dimensional macroporous FePO₄ as cathode materials for lithium-ion batteries, *Electrochem. Commun.* 2008, **10**, 1587-1589.
 15. M. Kotobuki, Y. Isshiki, H. Munakata, K. Kanamura, All-solid-state lithium battery with a three-dimensionally ordered Li_{1.5}Al_{0.5}Ti_{1.5}(PO₄)₃ electrode, *Electrochim. Acta* 2010, **55**, 6892-6896.
 16. H. Munakata, M. Otani, Y. Katsuki, K. Kanamura, 3-dimensionally ordered macroporous Ni-YSZ for low temperature SOFC, *ECS Transactions* 2009, **25**, 1855-1860.
 17. O.-H. Kim, Y.-H. Cho, S. H. Kang, H. Y. Park, M. Kim, J. W. Lim, D. Y. Chung, M. J. Lee, H. Choe, Y.-E. Sung, Ordered macroporous platinum electrode and enhanced mass transfer in fuel cells using inverse opal

- structure, *Nature Commun.* 2013, **4**, 2473.
18. H. David, L. Zhu, S. Neepa, H. Yaowu, C. S. Peter, Finite size effects in ordered macroporous electrodes fabricated by electrodeposition into colloidal crystal templates, *J. Phys. Chem. C* 2007, **111**, 3308-3313.
 19. A. Mihi, C. Zhang, P. V. Braun, Transfer of preformed three-dimensional photonic crystals onto dye-sensitized solar cells, *Angew. Chem. Int. Ed. Engl.* 2011, **50**, 5712-5715.
 20. J. H. Cho, J. M. Kim, J. Prabhuram, S. Y. Hwang, D. J. Ahn, H. Y. Ha, S.-K. Kim, Fabrication and evaluation of membrane electrode assemblies by low-temperature decal methods for direct methanol fuel cells, *J. Power Sources* 2009, **187**, 378-386.
 21. H. J. Cho, H.-S. Jang, S. Lim, E. Cho, T.-H. Lim, I.-H. Oh, H. K. Kim, J. H. Jang, Development of a novel decal transfer process for fabrication of high-performance and reliable membrane electrode assemblies for PEMFCs, *Int. J. Hydrogen Energy* 2011, **36**, 12465-12473.
 22. S. Shahgaldi, I. Alaefour, G. Unsworth, X. Li, Development of a low temperature decal transfer method for the fabrication of proton exchange membrane fuel cells *Int. J. Hydrogen Energy* 2017, **42**, 11813-11822.
 23. G. H. Han, H.-J. Shin, E. Sungkim, S. Jinchae, J.-Y. Choi, Y. H. Lee, Poly(ethylene co-vinyl acetate)-assisted one-step transfer of ultra-large graphene, *Nano Brief Rep. Reviews*, 2011, **6**, 59-65
 24. H. Zhang, Q. Yan, Q. Xu, C. Xiao, X. Liang, A sacrificial layer strategy for photolithography on highly hydrophobic surface and its application for electrowetting devices, *Sci. Rep.* 2017, **7**, 3983.
 25. N. M. Pichugina, A. M. Kutepov, I. G. Gorichev, A. D. Izotov, B. E. Zaitsev, Dissolution kinetics of nickel(II) and nickel(III) oxides in acid media, *Theor. Found. Chem. Eng.* 2002, **36**, 485-494.

26. Y. Li, H. Jiang, W. Huang, H. Tian, Effects of peak current density on the mechanical properties of nanocrystalline Ni–Co alloys produced by pulse electrodeposition, *Appl. Surf. Sci.* 2008, **254**, 6865-6869.
27. M. Moravej, S. Amira, F. Prima, A. Rahem, M. Fiset, D. Mantovani, Effect of electrodeposition current density on the microstructure and the degradation of electroformed iron for degradable stents, *Mater. Sci. Eng.: B* 2011, **176**, 1812-1822.
28. D. F. Abbott, D. Lebedev, K. Waltar, M. Povia, M. Nachtegaal, E. Fabbri, C. Copéret, T. J. Schmidt, Iridium oxide for the oxygen evolution reaction: correlation between particle size, morphology, and the surface hydroxo layer from operando XAS, *Chem. Mater.* 2016, **28**, 6591-6604.
29. Z. Ren, S. Quan, J. Gao, W. Li, Y. Zhu, Y. Liu, B. Chai, Y. Wang, The electrocatalytic activity of IrO₂-Ta₂O₅ anode materials and electrolyzed oxidizing water preparation and sterilization effect, *RSC Adv.* 2015, **5**, 8778-8786.
30. X. Yang, Y. Li, L. Deng, W. Li, Z. Ren, M. Yang, X. Yang, Y. Zhu, Synthesis and characterization of an IrO₂-Fe₂O₃ electrocatalyst for the hydrogen evolution reaction in acidic water electrolysis, *RSC Adv.* 2017, **7**, 20252-20258.
31. H. Song, S. Oh, H. Yoon, K.-H. Kim, S. Ryu, J. Oh. Bifunctional NiFe inverse opal electrocatalysts with heterojunction Si solar cells for 9.54%-efficient unassisted solar water splitting, *Nano Energy* 2017, **42**, 1-7.
32. X. Huang, J. Chen, Z. Lu, H. Yu, Q. Yan, H. H. Hng, Carbon inverse opal entrapped with electrode active nanoparticles as high-performance anode for lithium-ion batteries, *Sci. Rep.* 2013, **3**, 2317.
33. A. C. Peterlevitz, P. W. May, R. L. Harniman, J. A. Jones, H. J. Ceragioli, H. Zanin, Fast electron transfer kinetics on novel interconnected

- nanospheres of graphene layers electrodes, *Thin Solid Films* 2016, **616**, 698-702.
34. X. Leimin, L. Shijun, Y. Lijun, L. Zhenxing, Investigation of a novel catalyst coated membrane method to prepare low-platinum-loading membrane electrode assemblies for PEMFCs, *Fuel Cells* 2009, **2**, 101-105.
 35. J. E. Park, S. Y. Kang, S.-H. Oh, J. K. Kim, M. S. Lim, C.-Y. Ahn, Y.-H. Cho, Y.-E. Sung, High-performance anion-exchange membrane water electrolysis, *Electrochim. Acta* 2019, **295**, 99-106.
 36. S. Trasatti, Physical electrochemistry of ceramic oxides, *Electrochem. Acta* 1991, **36**, 225-241.
 37. L. A. da Silva, V. A. Alves, M. A. P. da Silva, S. Trasatti, J. F. C. Boodts, Oxygen evolution in acid solution on IrO₂ + TiO₂ ceramic films. A study by impedance, voltammetry and SEM, *Electrochem. Acta* 1997, **42**, 271-281.
 38. M. Mandal, A. Valls, N. Gangnus, M. Secanell, Analysis of inkjet printed catalyst coated membranes for polymer electrolyte electrolyzers, *J. Electrochem. Soc.* 2018, **165**, F543-F552.
 39. G. Li, H. Yu, W. Song, M. Dou, Y. Li, Z. Shao, B. Yi, A hard-template method for the preparation of IrO₂, and its performance in a solid-polymer-electrolyte water electrolyzer, *ChemSusChem* 2012, **5**, 858-861.
 40. S. Siracusano, V. Baglio, S. A. Grigoriev, L. Merlo, V. N. Fateev, A. S. Aricò, The influence of iridium chemical oxidation state on the performance and durability of oxygen evolution catalysts in PEM electrolysis, *J. Power Sources* 2017, **366**, 105-114.

Chapter 4. Development of membrane-electrode assembly for high-performance anion-exchange membrane water electrolysis

4.1. Introduction

MEA was fabricated using the catalyst-coated substrate (CCS) and catalyst-coated membrane (CCM) methods.¹ In the CCS method, a catalyst layer is fabricated on the GDL substrate. After the catalyst slurry is sprayed on the GDL, the membrane is sandwiched between the catalyst-coated GDLs using hot-pressing. Hot-pressing is crucial for preparing high-performance MEAs as it can enhance the adhesion between the catalyst layer and the membrane, leading to increased ionic connection.² However, intense heat and pressure can cause structural changes in the MEA and GDL, thereby potentially degrading the cell performance.³ By contrast, in the CCM method, a catalyst layer is directly fabricated on a membrane without hot-pressing. The CCM method avoids the structural damage of the MEA and GDL, reduces ohmic resistance, and simplifies the fabrication process as it does not need any additional processes.⁴ The CCM method is considered more suitable than the CCS method for fabricating high-performance fuel cells.^{4,5} Therefore, water electrolysis with an MEA fabricated using the CCM method is expected to show higher performance. However, most studies of water electrolysis have used the CCS method for MEA fabrication.⁶⁻¹³

The operating conditions, especially the feeding condition and operating temperature, can affect the cell performance. First, the feeding condition is important for ionic conductivity. In the AEMWE, high OH⁻ ionic conductivity of

the AEM is important for supplying hydroxide ions at the anode. Hydroxide ions in the AEM are transported across water in the water channel formed by functional groups.¹⁴ Hydroxide ions are also transferred across the AEM by the electroosmotic flow of water.¹⁵ As hydroxyl ion transport is slower than proton transport,¹⁶ the AEM still shows poor ionic conductivity. To enhance its ionic conductivity, more water channels are formed in the membrane. However, excessive functional groups cause too much water uptake, thereby lowering the mechanical strength of the AEM.¹⁷ Thus, many studies of AEMWE have used a KOH solution instead of pure water as a reactant at the anode and cathode to increase the ionic conductivity of the AEM.⁸⁻¹¹ The operating temperature also greatly influences the cell performance. Electrocatalyst kinetics increase with temperature according to the Tafel equation.^{18,19} However, high-temperature operation can induce severe chemical damage in the AEM, leading to lower ionic conductivity. The optimal temperature, which is high enough to not damage the membrane, should be determined.

The investigation of MEA parameters is crucial to attain high performance. The ionomer plays an important role in forming ionic pathways between the membrane and the catalyst layer and as a binder to develop a durable catalyst layer.^{10,20} Nafion, a widely used proton exchange ionomer, is well known for its high proton conductivity and stability. Other stable, low-cost, and high-conductivity anion exchange ionomers have also been developed for AEMWE. Recent studies have applied various developed ionomers such as AS-4 ionomer (Tokuyama),²¹ I₂ ionomer (Acta Spa),¹³ and PTFE ionomer (a nonionic conductor)⁹ with their optimized contents. In other words, the ionomer content is examined to determine the optimal value. Furthermore, the GDL plays important roles in the mass transport of the reactant and product and in the electron pathway between the catalyst layer and the bipolar plates. In water electrolysis, mass transport

overpotential arises when the products (oxygen gases) are transported through GDLs.²² The GDL thickness is a crucial factor in reducing the contact and mass transport resistances. A thin GDL induces large contact resistance between the catalyst layer and the GDL; however, it leads to efficient mass transport owing to the absence of compression. A thicker GDL affords better contact and can thus reduce the ohmic resistance; however, it leads to increased mass transport resistance owing to compression. Therefore, the GDL thickness must be optimized to achieve high AEMWE performance. Finally, kinetically sluggish OER is the major limitation to achieving high performance. To enhance cell performance, the OER catalyst loading in the anode should be increased to increase the number of active sites. However, excess catalyst loading results in a thicker catalyst layer and thereby induces larger mass transport resistance. Thus, optimizing the catalyst loading is critical for enhancing performance.

Wang et al.²¹ first demonstrated water electrolysis using a solid-state membrane. They prepared an MEA with IrO₂ as the OER catalyst and Pt black as the HER catalyst by using the CCM method. They used A-201 and AS-4 (Tokuyama) as the AEM and anion-exchange ionomer, respectively. The thickness and equivalent weight of the anion exchange membrane were 28 μm and 590. The AEMWE showed current density of 399 $\text{mA}\cdot\text{cm}^{-2}$ at 1.8 V with deionized water of 3 $\text{ml}\cdot\text{min}^{-1}$. Zhuang et al.⁶ fabricated an MEA using a self-crosslinking quaternary ammonia polysulfone (xQAPS) membrane and xQAPS ionomer with the thickness of 25 μm and equivalent weight of 735. Ni-Fe and Ni-Mo were used as the anode and cathode catalyst, respectively. The MEA was prepared using the catalyst-coated substrate (CCS) method with hot-pressing. Current density of 580 $\text{mA}\cdot\text{cm}^{-2}$ was achieved at 1.9 V with pure water as the reactant. Comotti et al.⁷ used Acta 3030 (Cu-based material) and Acta 4030 (Ni-based material), both of which are non-PGM catalysts, as OER and HER catalysts for AEMWE, respectively.

Furthermore, they used polytetrafluoroethylene (PTFE) as a nonionic binder instead of an ionomer. The catalyst layer was fabricated using the CCS method. They achieved current density of $470 \text{ mA}\cdot\text{cm}^{-2}$ at 1.79 V with a carbonate/bicarbonate solution ($1\% \text{ K}_2\text{CO}_3/\text{KHCO}_3$). Jang et al.⁸ examined the effect of the hot-pressing condition and binder content on the fabrication process. They used A-201 and PTFE as the AEM and binder, respectively, and 0.5 M potassium hydroxide (KOH) solution as the reactant. The A-201 has thickness of $28 \text{ }\mu\text{m}$ and equivalent weight of 590. They found that hot-pressing using the CCS method led to reduced polarization resistance and, in turn, increased cell performance. Furthermore, they found that the binder content affected the ohmic and polarization resistances and that the optimal PTFE binder content was $9 \text{ wt}\%$. Jang et al.⁹ also inspected the reactant feed method to realize high-performance and durable AEMWE. They achieved high and durable AEMWE performance of $1070 \text{ mA}\cdot\text{cm}^{-2}$ at 1.8 V , the best performance reported thus far, under dry cathode operation; this was attributed to reduced ohmic and polarization resistances.

Studies of AEMWE have thus far used different AEMs, anion-exchange ionomers, and operating conditions. However, using FAA-3-50 and FAA-3-Br as the AEM and anion-exchange ionomer, respectively, is essential for improving AEMWE performance. In this study, we investigated the effect of the MEA fabrication method, operating conditions, and MEA parameters on the AEMWE performance. First, the MEA fabrication methods were examined to reduce the ohmic and mass transport resistances. Second, AEMWE was performed under various operating conditions (reactant type and cell temperature) to improve cell performance. Finally, MEA parameters such as ionomer content, type of GDL and OER catalyst loading were investigated. The optimization of AEMWE was evaluated using single-cell tests and electrochemical impedance spectroscopy (EIS).

4.2. Experimental section

4.2.1. AEMWE components and assembly

Figure 4.1 shows a schematic of the MEA in AEMWE. FAA-3-50 (Fumatech, Germany) was used as the AEM. The thickness and equivalent weight of the used AEM were 50 μm and 540, respectively. First, FAA-3-50 was soaked in 1 M of potassium hydroxide (KOH) solution for 1 h and then rinsed with deionized water. Then, MEAs were fabricated using the CCM method. In this study, we used IrO_2 (Surepure Chemetals, USA) and 40 wt% Pt/C (Johnson Matthey, UK) as commercial OER and HER catalysts, respectively, to investigate the parameters of a single-cell AEMWE excluding the effect of catalytic activity. The catalyst slurry was prepared using IrO_2 and 40 wt% Pt/C for the anode and cathode catalyst, respectively, ionomer (FAA-3-Br, Fumatech, Germany), isopropyl alcohol, and deionized water. Each catalyst ink was sprayed on the membrane, and dried for 24 hrs at room temperature. Then, a GDL was placed on both sides of the CCM. Titanium-based (Ti-GDL, CNL Energy, Korea) and carbon-based (C-GDL, JNTG Co., Korea) GDLs were used as the anode and cathode GDL, respectively. Three types of Ti-GDLs with different thicknesses were used: 250, 350 and 400 μm . The thicknesses of each C-GDL were 270 (JNTG20-A3), 320 (JNTG30-A3) and 420 μm (JNTG40-A3). The thickness of gasket used in this work was 250 μm . The active area was 5 cm^2 .

4.2.2. Electrochemical characterization

For AEMWE single-cell tests, titanium and graphite bipolar plates with a serpentine flow field were applied as the anode and cathode current collector, respectively. The prepared MEA was placed between two bipolar plates. Then, single-cells were assembled with the tightening torque of 80 kgf cm^{-2} . The single-cells were square-shaped with area of 5 cm^2 . DI water (only the effect of feed

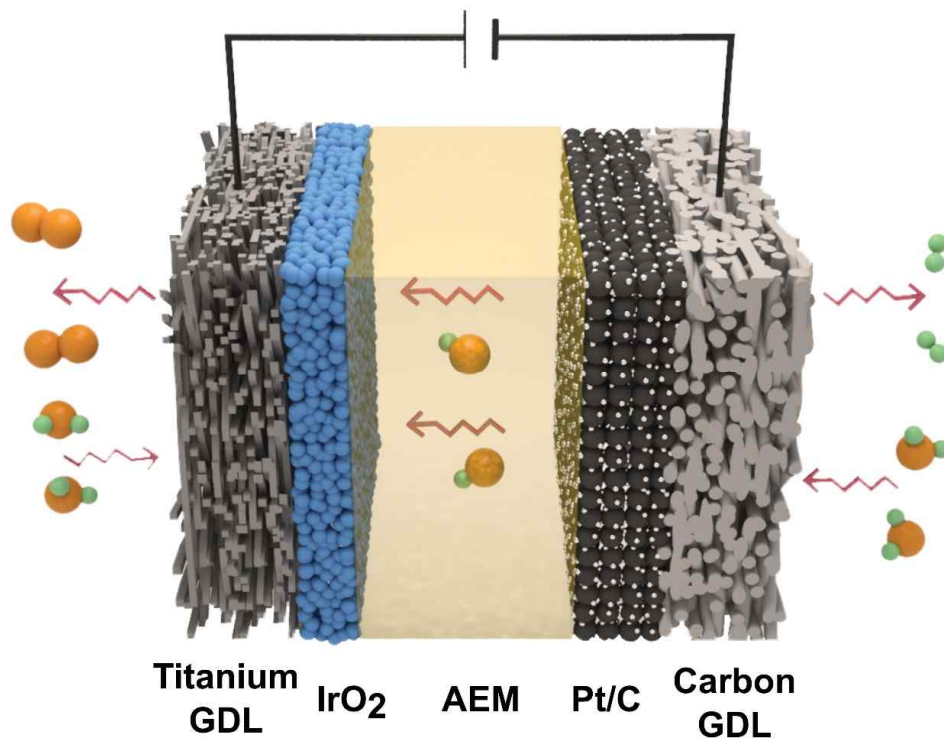


Figure 4.1 Schematic diagram of single-cell components in AEMWE.

conditions) and KOH solution (all investigations except the effect of feed conditions) preheated to 50°C were fed to the anode and cathode sides with flow rate of 1 (all investigations except the effect of reactant flow rates and temperature) or 2.5 (effect of temperature and optimized cell performance) ml·min⁻¹. The cell temperature was maintained at 50°C to avoid membrane degradation in all investigations except the effect of cell performance and optimized cell performance. The experimental conditions for each section are provided in the supporting information. The cell performance was determined using the voltage sweep method from 1.35 to 2.15 V at a scan rate of 2 mV·s⁻¹ using a potentiostat (ZAHNER-Elektrik GmbH & Co. KG, Germany). EIS (ZAHNER-Elektrik GmbH & Co. KG, Germany) was performed to examine the resistance of AEMWE at 1.9 V with amplitude of 50 mV and frequency range of 100 mHz to 100 kHz. The resistance with different GDL thicknesses was measured using EIS in N₂/N₂ atmosphere to compare the contact resistance of GDLs with different thicknesses. Only two GDLs (Ti-GDL and C-GDL) were assembled and operated at constant current of 100 mA.

4.2.3. Physical characterization

The MEA morphology was examined using field-emission scanning electron microscopy (FE-SEM; SUPRA 55VP, Carl Zeiss, Germany). The thickness of MEAs obtained using the CCS and CCM methods was measured using a thickness gauge (Mitutoyo No. 7301, Japan). The catalyst layer porosity was analyzed using mercury porosimetry (MicroActive AutoPore V 9600, Micromeritics Co.).

4.3. Results and Discussion

4.3.1. Effect of MEA fabrication method

In this study, we investigated the CCS and CCM methods for MEA fabrication to identify the optimal method from the viewpoint of AEMWE performance. Figure 4.2 shows polarization curves of MEAs fabricated using the CCS (with and without hot-pressing), and CCM methods. As shown in Figure 4.2a, the MEA fabricated using the CCS method without hot-pressing showed obviously low current density, indicating that AEMWE could not be performed properly. This is attributed to the high contact resistance between the membrane and the catalyst layer owing to the lack of hot-pressing. By contrast, the MEA fabricated using the CCS method with hot-pressing showed relatively higher performance. As shown in Figure 4.3, the cell performance of AEMWE increased with the increase in the hot-pressing temperature to 70 °C. However, higher temperatures (> 70 °C) caused the chemical damage of the membrane to the extent that the AEMWE could not be operated. Overall, the optimal hot-pressing temperature for achieving high performance was determined to be 70 °C. This result indicates that hot-pressing is essential in the CCS method to enhance the contact between the membrane and the catalyst layer and thus improve cell performance. Finally, the MEA fabricated using the CCM method showed the highest performance among all MEAs. Also, unlike the CCS method, the CCM method led to good repeatability of AEMWE performance (Figure 4.4).

Furthermore, to characterize the resistances in AEMWE, EIS was performed at 1.9 V (Figure 4.2b). The Nyquist plot obtained using EIS indicates the three different resistances in AEMWE: ohmic resistance, charge-transfer resistance, and mass transport resistance. Two overlapping arcs were observed in the Nyquist plot. The intercept in the high-frequency region represents the ohmic resistance, which consists of the ionic and electronic resistances. Furthermore, the arc in the d

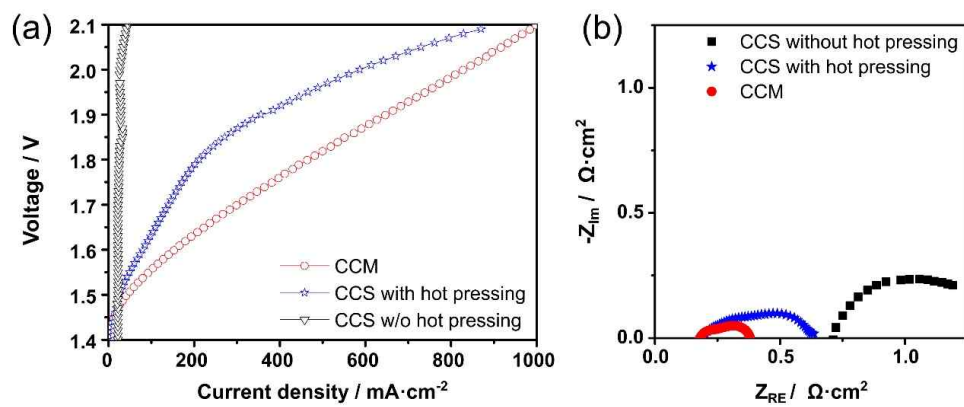


Figure 4.2 (a) Polarization curves and (b) Nyquist plots for AEMWE single cells with different fabrication processes: CCS without and with hot-pressing, and CCM at 50 °C. Nyquist plots were evaluated at 1.9 V. The feed condition was 1.0 KOH solution in both electrodes with flow rate of 1 ml·min⁻¹.

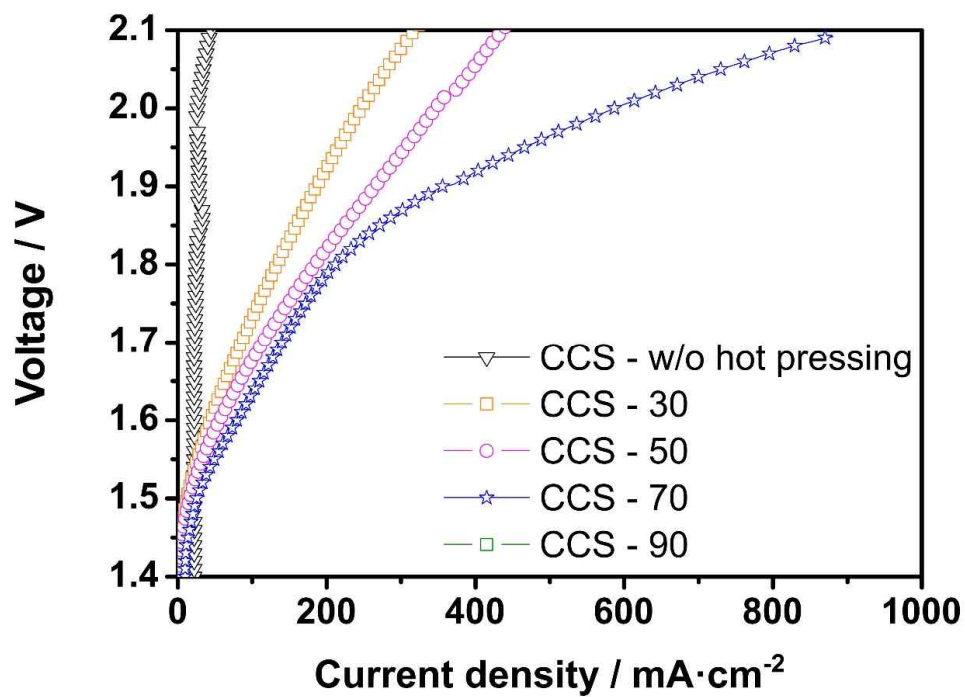


Figure 4.3. Polarization curves of AEMWEs prepared with different hot pressing conditions (no, 30, 50, 70, and 90 °C) of CCS method.

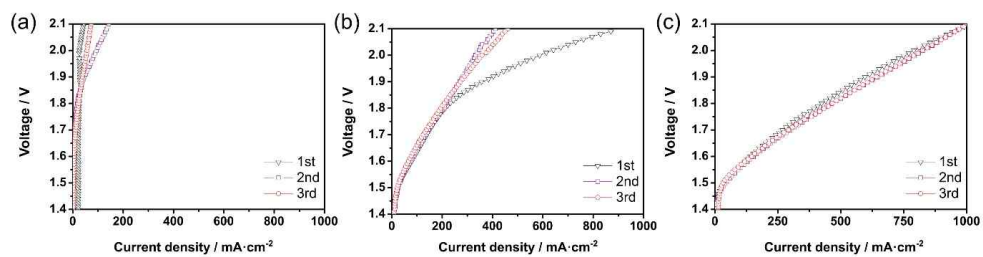


Figure 4.4 Polarization curves of AEMWE single cells with different fabrication processes: CCS without and with hot-pressing, and CCM.

high- and low-frequency regions indicates the charge-transfer resistance associated with the electrochemical reaction and the mass transport resistance related to the transport of reactant and product, respectively.²³ The CCS method without hot-pressing showed much higher ohmic resistance than the other fabrication methods; this resulted in low cell performance (Figure 4.2a). In addition, MEAs fabricated using the CCS method with hot-pressing and the CCM method had approximately same ohmic resistances. This result indicates that hot-pressing is important in the CCS method to ensure good contact between the catalyst layer and the membrane. However, the MEA fabricated using the CCS method with hot-pressing showed higher mass transport resistance, indicated by the arc in the low-frequency region. As shown in Figure 4.5, the thickness of the total MEA and GDL fabricated using the CCS and CCM methods was 540 and 810 μm , respectively, indicating that the CCS method with hot-pressing compressed the GDL. The compressed GDL caused changes in the pore structure, in turn resulting in increased mass transport resistance. By contrast, the MEA fabricated using the CCM method showed the lowest ohmic, charge transfer, and mass transport resistances. Therefore, the CCM method was considered the optimal MEA fabrication method for AEMWE. Only the CCM method is considered in the following sections.

4.3.2. Effect of reactants

The following four feed conditions were used: (1) feeding DI water only to cathode, (2) feeding DI water to both electrodes, (3) feeding 1.0 M KOH only to cathode, and (4) feeding 1.0 M KOH to both electrodes. Figure 4.6a shows the polarization curves with different feed conditions. First, the effect of KOH feed solution was examined with two different reactants (KOH solution and DI water). The use of DI water as a reactant (cases 1 and 2) resulted in unstable cell

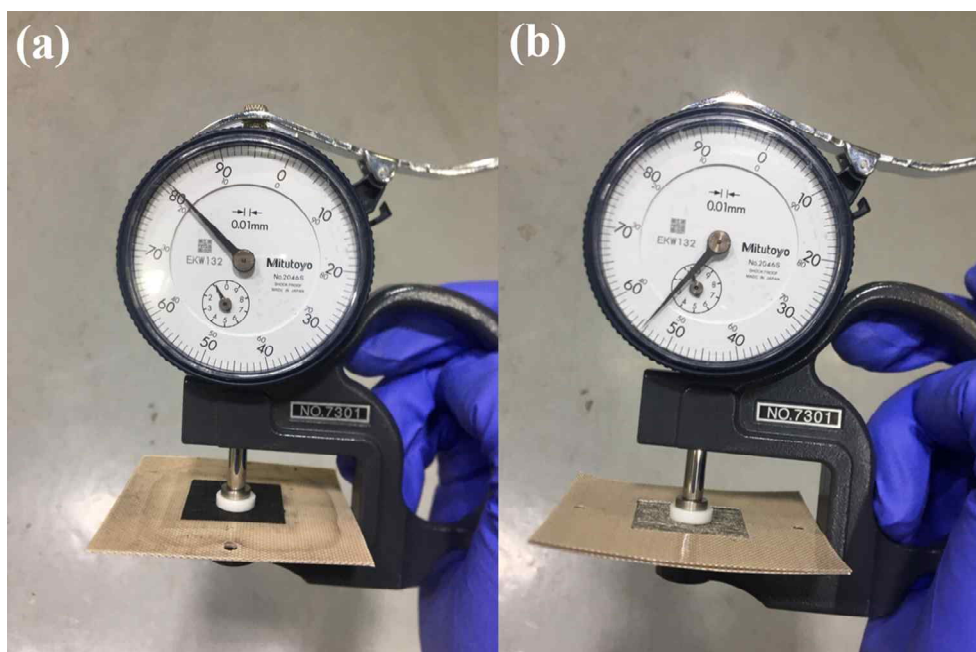


Figure 4.5 Photographs of thicknesses of two MEAs with different fabrication methods: (a) CCM and (b) CCS.

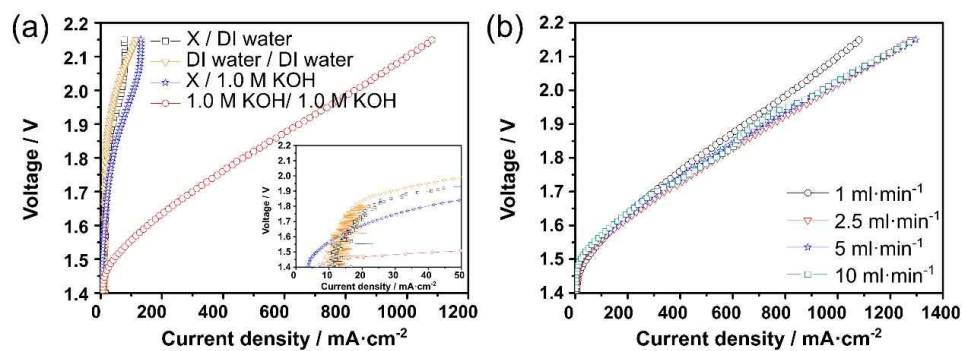


Figure 4.6 (a) Polarization curves for AEMWEs operated with different reactant feed methods (1–4), and (b) cell performance of AEMWEs with different reactant flow rates (1 M KOH) fed into both sides of electrode (1, 2.5, 5, and 10 ml·min⁻¹) at 50 °C.

performance in low-voltage regions (< 1.8 V). By contrast, the use of KOH solution as a reactant (cases 3 and 4) resulted in stable performance because it increased the ionic conductivity of AEM.

Additionally, we investigated the effect of feeding KOH solution at the anode and cathode to enhance the performance. In case 3 (feeding KOH solution only to cathode), the AEMWE showed stable but low performance ($69.3 \text{ mA}\cdot\text{cm}^{-2}$ at 1.9 V). By contrast, in case 4 (feeding KOH solution to both electrodes), the performance was enhanced by a factor of 9.4. Therefore, feeding KOH solution to the anode results in high performance. As discussed above, as hydroxide ions are oxidized to produce oxygen at the anode, they are considered anode reactants. Hydroxide ions supplied externally by the KOH solution promoted the OER at the anode, leading to increased overall performance. In other words, supplying KOH solution to both electrodes enhanced the ionic conductivity of AEM and directly supplied hydroxide ions at the anode, resulting in enhanced performance. Therefore, case 4 is considered the optimal feeding method. However, the KOH feed solution at the cathode can reduce the hydrogen purity owing to the high content of water.

We also evaluated the effect of reactant flow rates ($1, 2.5, 5,$ and $10 \text{ ml}\cdot\text{min}^{-1}$) to determine the optimal flow rate. The reactant in AEMWE is 1.0 M KOH solution, and cell performance can be enhanced with increased flow rate. Figure 4.6b shows the AEMWE cell performance with different 1.0 M KOH solution flow rates. When the flow rate was increased from 1 to $2.5 \text{ ml}\cdot\text{min}^{-1}$, the current density at 1.9 V was enhanced owing to the increased reactant in the catalyst layer. At flow rate of $2.5 \text{ ml}\cdot\text{min}^{-1}$, sufficient reactant was supplied and the cell performance saturated, and the performance was not enhanced further with increased flow rate. Therefore, $2.5 \text{ ml}\cdot\text{min}^{-1}$ is considered the optimal reactant flow rate.

4.3.3. Effect of cell temperature

Figure 4.7 shows the AEMWE performance evaluated at different operating temperatures (50, 60, and 70 °C). The current density at 1.9 V increased by a factor of 2.2 when the operating temperature was increased from 50 to 70 °C. To further examine the effect of operating temperature, EIS was conducted at 1.9 V. As shown in Fig. 4 (b), the charge transfer resistance decreased with increasing temperature. The ohmic resistance, indicated by the intercept in the high-frequency region, also decreased, indicating that ionic conductivity increased with temperature. This is consistent with the results of other AEMs such as R4-C12 and QPPO.²⁴ Therefore, 70°C is considered the optimal cell temperature to show high initial performance.

4.3.4. Effect of ionomer content

MEAs with different FAA-3-Br anion ionomer contents of 10, 20, and 30 wt% were prepared to determine the optimal content. As shown in Figure 4.8a, cell performance increased as the ionomer content increased from 10 to 20 wt. %. Furthermore, the Nyquist plot obtained using EIS showed that charge-transfer resistance decreased with increased ionomer content. This is attributed to the increased size of secondary pores in the catalyst layer caused by the high ionomer content that, in turn, improves reactant transport to active sites of catalysts. The ionomer content also affected the morphology of the catalyst layer in terms of secondary pore formation.²⁵ Figure 4.8b shows SEM images of catalyst layers with different ionomer contents. As the ionomer content increased from 10 to 30 wt%, larger secondary pores were formed. Furthermore, mercury porosimetry (Table 4.1) measurements showed that the porosity of the catalyst layer slightly increased with ionomer content, indicating that more pores were formed in the catalyst layer. By contrast, the performance for higher ionomer content of 30 wt. % was poorer than that for ionomer content of 20 wt%. Furthermore, the charge transfer, mass transport, and ohmic resistances all increased at ionomer content of 30 wt. %. This

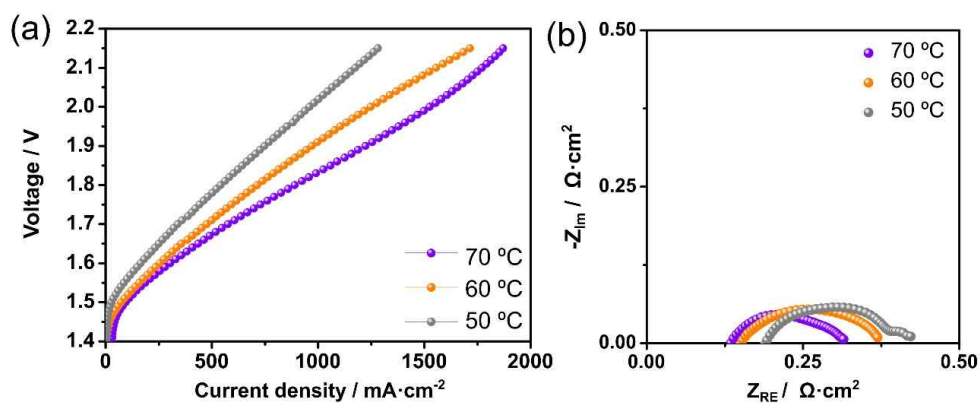


Figure 4.7 (a) Polarization curves and (b) Nyquist plots for AEMWEs operated at different cell temperatures (50, 60, and 70 °C). Nyquist plots were evaluated at constant voltage of 1.9 V. The feed condition was 1.0 KOH solution in both electrodes with flow rate of 2.5 ml·min⁻¹.

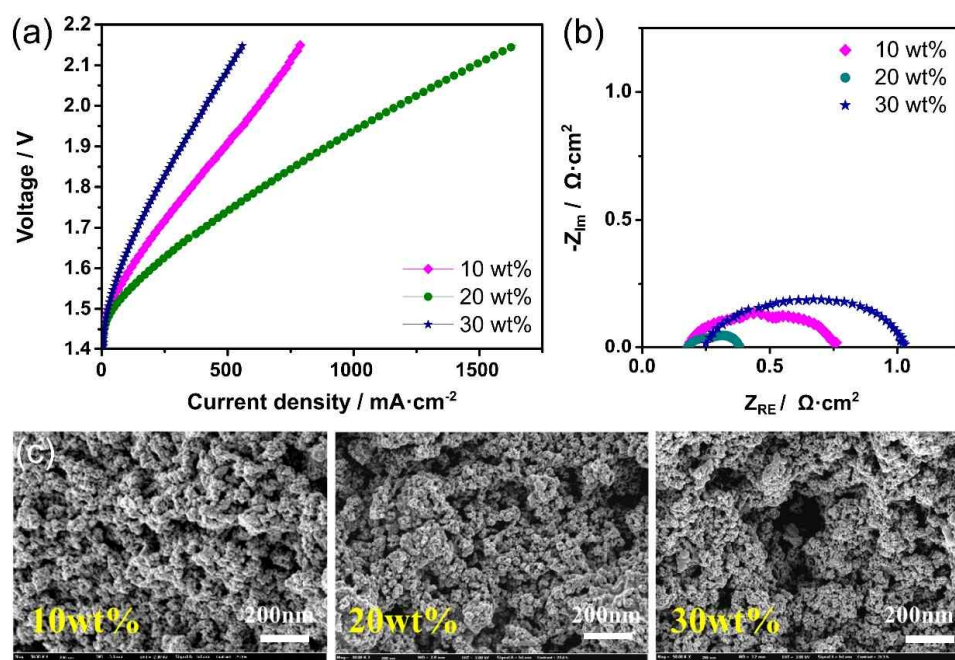


Figure 4.8 (a) Polarization curves and (b) Nyquist plots for AEMWEs with different ionomer contents (10, 20, and 30 wt. %) at 50 °C, and (c) FE-SEM images of MEAs fabricated using different ionomer contents. The feed condition was 1.0 KOH solution in both electrodes with flow rate of 1 ml·min⁻¹.

Table 4.1. Porosity of MEA with different ionomer contents measured by using mercury porosimetry

Ionomer content [wt.%]	10	20	30
Porosity [%]	76.9	77.7	78.5

is because excess ionomer content increased the number of covered active sites and detached some catalyst particles, thereby blocking the pathway of the reactant on the catalyst and inhibiting the electrical connection. In other electrochemical devices consisting of a polymer-electrolyte membrane, such as PEMFC and direct methanol fuel cell (DMFC), the ionomer content in the catalyst layer greatly influences the ionic conductivity as the ionomer plays a role in transporting ions to active sites of catalysts.²⁶ By contrast, the ionomer content in AEMWE does not depend on ionic conductivity because AEMWE is operated by feeding KOH solution to supply hydroxide ions in the catalyst layer. Therefore, the MEA with 20 wt% ionomer content showed the highest performance, indicating that its catalyst layer is optimal for achieving a trade-off between the active sites for the electrochemical reaction and the pore morphology.

4.3.5. Effect of GDL

To investigate the effect of GDL thickness on cell performance, the contact resistance was predicted indirectly by measuring the resistances of cells assembled using only GDLs with different thicknesses in nitrogen atmosphere. In nitrogen atmosphere, the resistance is associated with electrical conductivity and contact resistance. As the electrical conductivity of Ti-GDLs was the same, the resistance depends on the contact resistance. To examine the effect of GDL thickness on resistance, we chose a reference GDL with low thickness (in case of the the effect of Ti-GDL, the reference GDL was C-GDL with thickness of 270 μm , and conversely, the thickness of Ti-GDL was 250 μm). Figure 4.9a shows the total cell resistance with three Ti-GDLs. As shown in Figure 4.9a, the contact resistance decreased with an increase in the thickness of Ti-GDL. Figure 4.9b shows the total cell resistance with three C-GDLs. The Ti-GDL used had 250- μm thickness. The resistance of C-GDLs showed the same trend as that of Ti-GDL. As a result, the

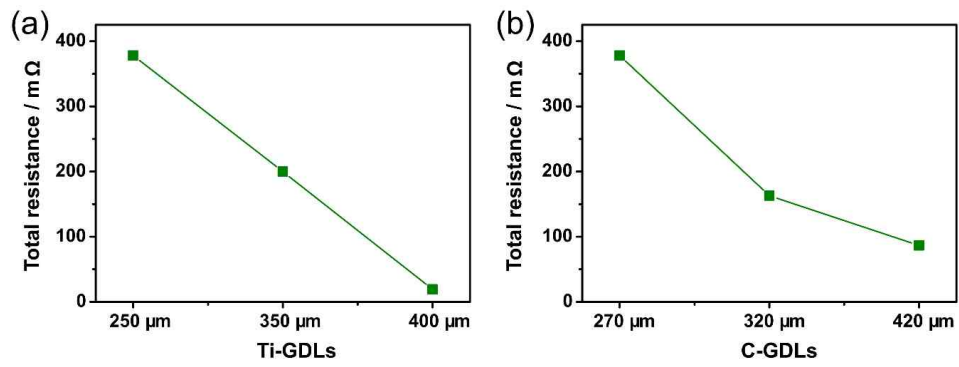


Figure 4.9 Total resistance with different (a) Ti-GDLs (The C-GDL used was 270 μm) and (b) C-GDLs. (The Ti-GDL used was 250 μm) in N₂/N₂ atmosphere.

contact resistance decreased with an increase in GDL thickness. It is expected that a thick GDL shows the highest performance.

Figure 4.10 shows AEMWEs with different Ti-GDL anode thicknesses (250, 350, and 400 μm) and C-GDL cathode thickness of 420 μm . Unexpectedly, the MEA with 350- μm -thick Ti-GDL showed the highest performance. As the gasket around the GDL had 250- μm thickness, the AEMWE with 250- μm -thick Ti-GDL showed low performance owing to the large charge transfer resistance and mass transport resistance; this is also confirmed by EIS measurements (Figure 4.11a). For 400- μm -thick Ti-GDL, the cell performance was lower than that for 350- μm -thick Ti-GDL because a thicker GDL caused compression during cell assembly, resulting in increased mass transport resistance (Figure 4.11a). Therefore, Ti-GDL with 350- μm thickness showed the highest performance. Figure 4.10b shows the AEMWE cell performance with different C-GDL cathode thicknesses (270, 320, and 420 μm). The cell performance increased with C-GDL thickness, and 420- μm -thick C-GDL resulted in the highest performance; this is consistent with the trend of contact resistance. Nyquist plots (Figure 4.11b) showed that increased C-GDL thickness led to decreased ohmic, charge transfer, and mass transport resistances. In this manner, Ti-GDL and C-GDL thicknesses are optimized to minimize the ohmic and mass transport resistances.

4.3.6. Effect of OER catalyst loading

We evaluated AEMWE with different anode catalyst loadings (1, 2, 4, and 6 $\text{mg}\cdot\text{cm}^{-2}$) using IrO_2 , a commercially used OER catalyst. Figure 4.12 shows that when catalyst loading increased from 1.0 to 4.0 $\text{mg}\cdot\text{cm}^{-2}$, the current densities at 1.9 V were enhanced by a factor of ~ 1.8 , which is attributed to the increased amount of active sites. Furthermore, AEMWE with catalyst loading of 6 $\text{mg}\cdot\text{cm}^{-2}$ showed lower performance than that with catalyst loading of 4 $\text{mg}\cdot\text{cm}^{-2}$. This is

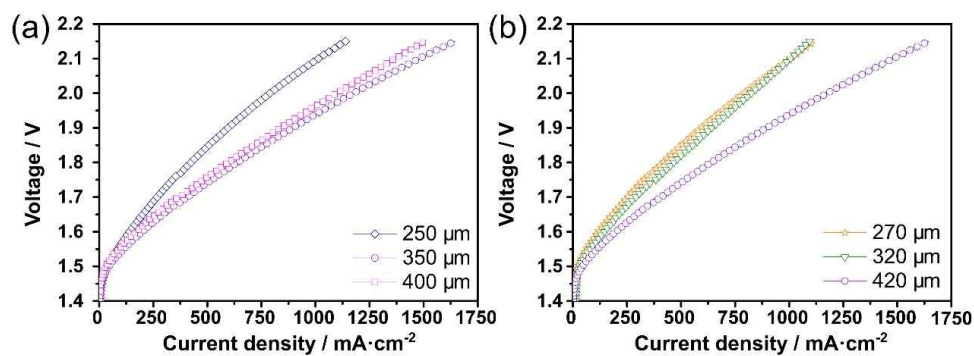


Figure 4.10 Polarization curves for single cells with different thickness of (a) Ti-GDLs and (b) C-GDLs at 50 °C. The feed condition was 1.0 KOH solution in both electrodes with flow rate of 1 ml·min⁻¹.

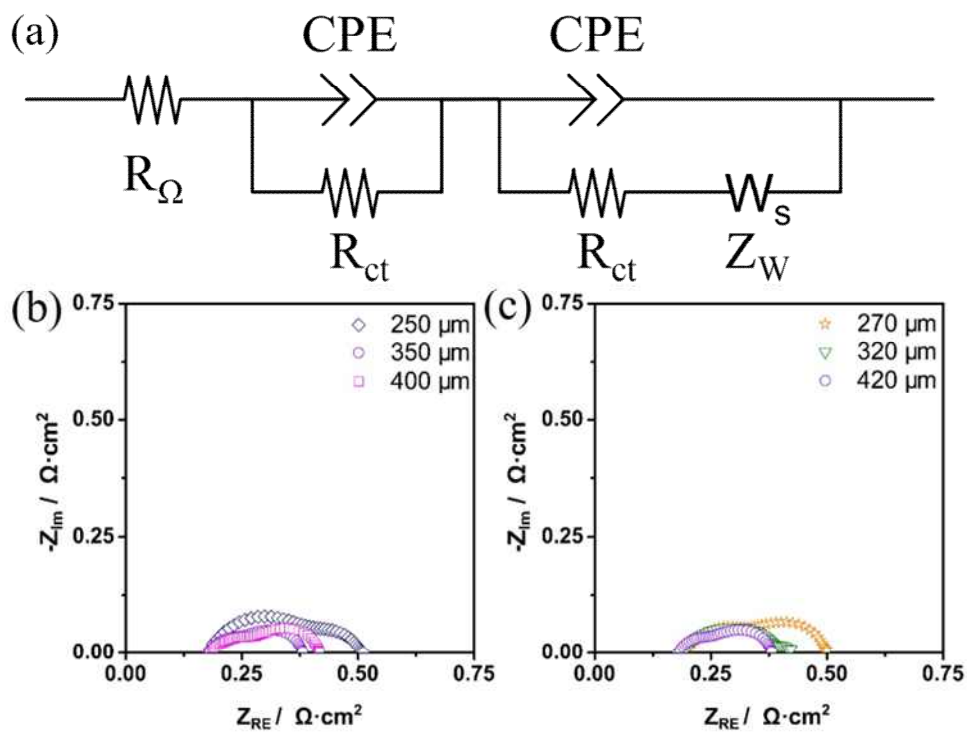


Figure 4.11 (a) Equivalent circuit model and Nyquist plots of AEMWEs with different (b) Ti-GDLs and (c) C-GDLs.

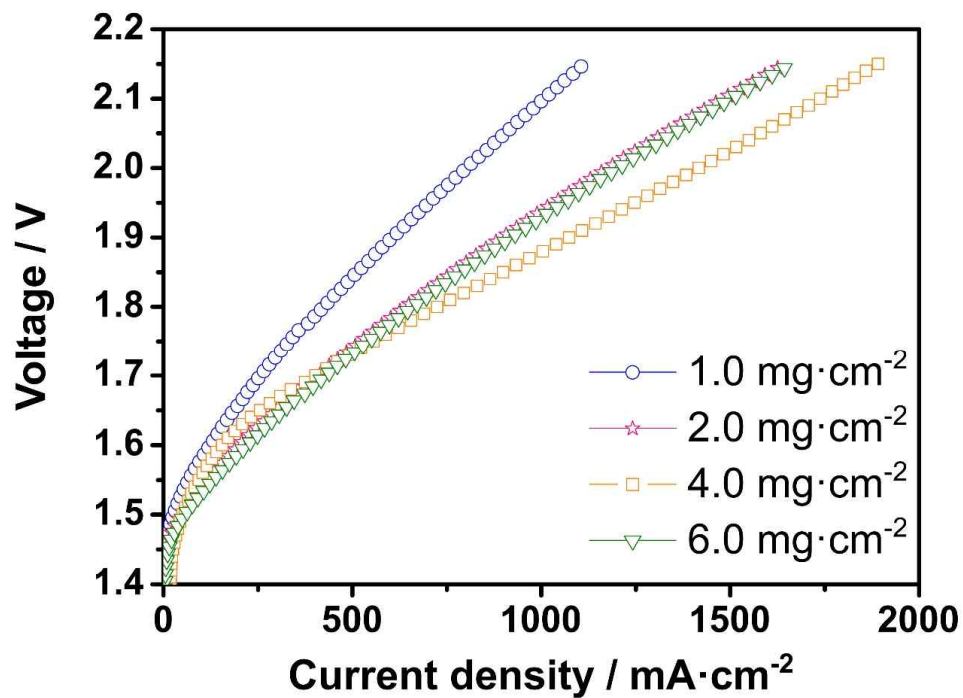


Figure 4.12 Polarization curves for AEMWEs with different IrO₂ catalyst loadings (1.0, 2.0, 4.0, and 6.0 mg·cm⁻²) in anode at 50 °C. Cathode catalyst loading was 40 wt% with 0.4 mg·cm⁻². The feed condition was 1.0 KOH solution in both electrodes with flow rate of 1 ml·min⁻¹.

because the thicker catalyst layer resulting from high catalyst loading causes mass transport resistance (Figure 4.13). Thus, the optimal catalyst loading was found to be $4 \text{ mg}\cdot\text{cm}^{-2}$; this value is suitable for balancing the trade-off between high catalytic activity and low mass transport resistance.

4.3.7. Optimized cell performance

Figure 4.14a shows the cell performance of AEMWE with the optimal fabrication method, operating conditions, and MEA parameters, as discussed above. When FAA-3-50 and FAA-3-Br were used as the AEM and anion-exchange ionomer, respectively, AEMWE showed current density of 1.15 and $1.5 \text{ A}\cdot\text{cm}^{-2}$ at 1.8 and 1.9 V , respectively. These are the highest values reported for AEMWE to date. Table 4.2 summarizes the AEMWE performance with different components and operating conditions reported to date.^{6-11,13,21} Many studies of AEMWE have used different types of catalysts, anion-exchange ionomers, and AEMs on MEAs to achieve high performance. They have also performed AEMWE under different operating conditions. Figure 4.14b shows that the AEMWE optimized in this study had the highest performance at 1.8 V . This is because we set suitable MEA parameters and operating conditions, used the CCM method instead of the CCS method for MEA fabrication, and used FAA-3-50 and FAA-3-Br as the anion-exchange ionomer and AEM, respectively, to enhance cell performance and minimize resistances despite the use of a commercial catalyst. Furthermore, although AEMWE performance is generally much lower than PEMWE performance, we achieved AEMWE performance that was $\sim 65\%$ of PEMWE performance, as shown in Figure 4.15. Thus, the optimized AEMWE is a practical device that exhibits outstanding performance.

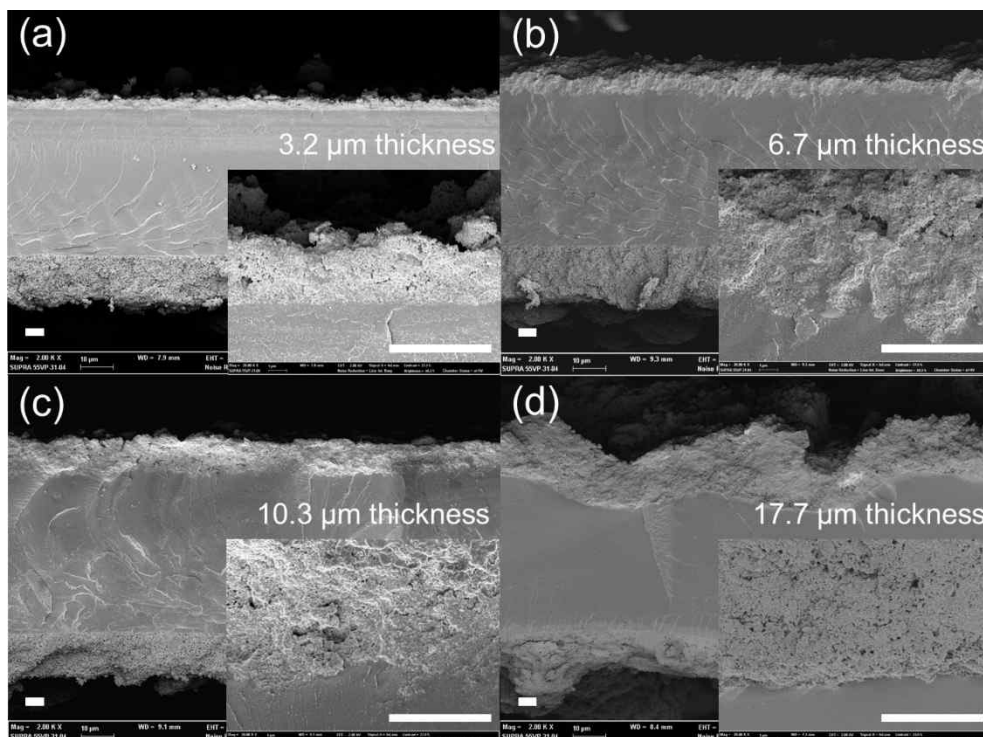


Figure 4.13 SEM cross section images of MEAs with different anode catalyst loadings of (a) 1 (b) 2 (c) 4 and (d) 6 $\text{mg}\cdot\text{cm}^{-2}$. The scale bar represents 5 μm .

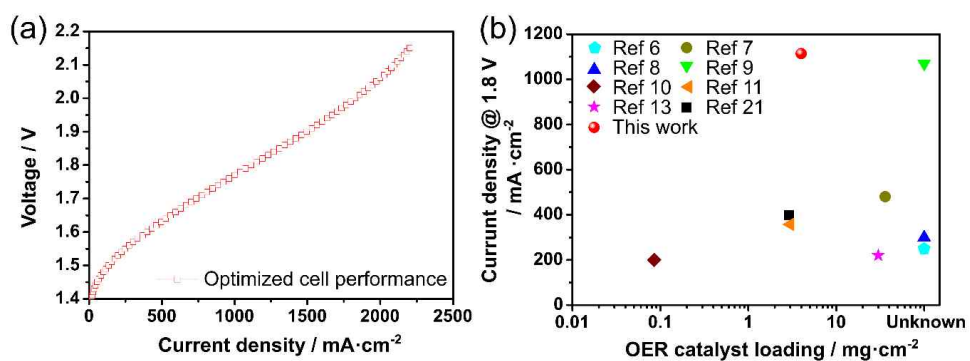


Figure 4.14 (a) Polarization curves for AEMWEs with optimized MEA fabrication method, operating conditions, and MEA parameters at 70 °C. The feed condition was 1.0 KOH solution in both electrodes with flow rate of 2.5 ml·min⁻¹. (b) Comparison of cell performance achieved in this study and those reported in literature.^{6-11,13,21}

Table 4.2. The summary of materials, components, cell operations, and performance of AEMWE reported in literature

Reference	Fabrication method	Membrane	Ionomer	Anode catalyst [mg·cm ⁻²]	Cathode catalyst [mg·cm ⁻²]	Cell temperature [°C]	Electrolyte	Performance [mA·cm ⁻²]
This work	CCM	FAA-3-50, FAA-3-Br, Fumatech	Fumatech	IrO₂ (4)	Pt/C (0.4)	70	1.0 M KOH	1500 (1.9 V)
[6]	CCS	Quaternary ammonia polysulfone (xQAPS)	xQAPS	Ni-Fe (-)	Ni-Mo (40)	70	Pure water	580 (1.9 V)
[7]	CCS	A-201, Tokuyama	PTFE	Acta 3030, Acta 4030, Acta (36)	Acta (7.4)	50	1% K ₂ CO ₃ /KHCO ₃	470 (1.79 V)
[8]	CCS	A-201, Tokuyama	PTFE	IrO ₂ (-)	Pt/C (-)	50	0.5 M KOH	299 (1.8 V)
[9]	CCS	A-201, Tokuyama	PTFE	IrO ₂ (-)	Pt/C (-)	50	0.5 M KOH	1070 (1.8 V)
[10]	CCS	A-201, Tokuyama	-	Ni (0.085)	Pt-Ni (0.047)	50	1.0 M KOH	250 (1.9 V)
[11]	CCS	YAB, Foma	PTFE	Ni ₁₂ P ₅ /Ni ₃ (PO ₄) ₂ -HS (3)	Ni ₁₂ P ₅ /Ni ₃ (PO ₄) ₂ -HS (3)	50	1M KOH	357.6 (1.8 V)

[13]	CCS	A-201, Tokuyama	I ₂ , Acta	Acta 3030,Acta 4030, Acta (30) Acta (7.4)	60	1% K ₂ CO ₃	500 (1.95 V)	
[21]	CCM	A-201, Tokuyama	AS-4, Tokuyama	IrO ₂ (2.9)	Pt black (3.2)	50	Deionized water	399 (1.8 V)

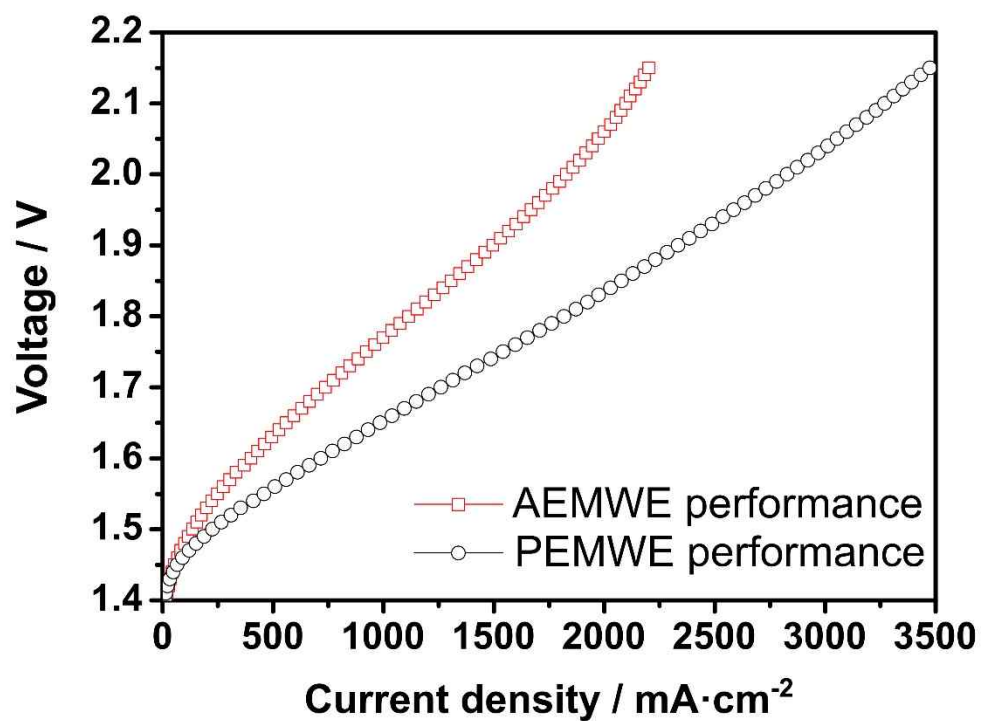


Figure 4.15 Comparison of cell performance in AEMWE and PEMWE with same MEA parameters and operating conditions.

4.4. Conclusions

We investigated the MEA fabrication method, MEA parameters, and operating conditions to achieve high AEMWE performance. Specifically, we achieved current density of 1.15 and 1.5 A·cm⁻² at 1.8 and 1.9 V, respectively; these are the highest values reported thus far. This enhancement is attributed to three main effects: (1) modified MEA fabrication method, (2) investigation and selection of optimized MEA parameters and operating conditions, and (3) the first application of a membrane-ionomer combination. Most AEMWE studies used the CCS method for MEA fabrication; however, we used the CCM method, leading to enhanced performance. Furthermore, optimizing the MEA parameters (i.e., determining the optimal MEA structure) and operating conditions enabled minimized ohmic, charge-transfer and mass transport resistance, leading to the increased performance. Finally, FAA-3-50 and FAA-3-Br were used for the first time as the AEM and ionomer, respectively, in AEMWE. Therefore, the investigation of parameters achieved high AEMWE performance. Nevertheless, further studies on the durability of AEMWE should be conducted because studies have reported that the AEM and ionomer developed thus far are weak, leading to low chemical stability.

4.5. References

1. S. Thanasilp, M. Hunsom, Effect of MEA fabrication techniques on the cell performance of Pt-Pd/C electrocatalyst for oxygen reduction in PEM fuel cell, *Fuel* 2010, **89**, 3847-3852.
2. W. Vielstich, H. Yokokawa, H. A. Gasteiger, Handbook of fuel cells: Fundamentals, technology and applications, John Wiley & Sons, 2009.
3. T. Frey, M. Linardi, Effects of membrane electrode assembly preparation on the polymer electrolyte membrane fuel cell performance, *Electrochimica Acta* 2004, **50**, 99-105.
4. X. Peng, T. Omasta, W. Rigdon, W. E. Mustain, Fabrication of high performing PEMFC catalyst-coated membranes with a low cost air-assisted cylindrical liquid jets spraying system, *J. Electrochem. Soc.* 2016, **163**, E407-E413.
5. X. Leimin, L. Shijun, Y. Lijun, L. Zhenxing, Investigation of a novel catalyst coated membrane method to prepare low-platinum-loading membrane electrode assemblies for PEMFCs, *Fuel Cells* 2009, **9**, 101-105.
6. L. Xiao, S. Zhang, J. Pan, C. Yang, M. He, L. Zhuang, J. Lu, First implementation of alkaline polymer electrolyte water electrolysis working only with pure water, *Energy & Environ. Sci.* 2012, **5**, 7869-7871.
7. C. C. Pavel, F. Cecconi, C. Emiliani, S. Santiccioli, A. Scaffidi, S. Catanorchi, M. Comotti, Highly efficient platinum group metal free based membrane-electrode assembly for anion exchange membrane water electrolysis, *Angew. Chem. Int. Ed. Engl.* 2014, **53**, 1378-1381.
8. M. K. Cho, H.-Y. Park, S. Choe, S. J. Yoo, J. Y. Kim, H.-J. Kim, D. Henkensmeier, S. Y. Lee, Y.-E. Sung, H. S. Park, J. H. Jang, Factors in electrode fabrication for performance enhancement of anion exchange membrane water electrolysis, *J. Power Sources* 2017, **347**, 283-290.

9. M. K. Cho, H.-Y. Park, H. J. Lee, H.-J. Kim, A. Lim, D. Henkensmeier, S. J. Yoo, J. Y. Kim, S.Y. Lee, H. S. Park, J. H. Jang, Alkaline anion exchange membrane water electrolysis: Effects of electrolyte feed method and electrode binder content, *J. Power Sources* 2018, **382**, 22-29.
10. S. H. Ahn, S. J. Yoo, H.-J. Kim, D. Henkensmeier, S. W. Nam, S.-K. Kim, J. H. Jang, Anion exchange membrane water electrolyzer with an ultra-low loading of Pt-decorated Ni electrocatalyst, *Appl. Catal. B: Environ.* 2016, **180**, 674-679.
11. J. Chang, Q. Lv, G. Li, J. Ge, C. Liu, W. Xing, Core-shell structured Ni₁₂P₅/Ni₃(PO₄)₂ hollow spheres as difunctional and efficient electrocatalysts for overall water electrolysis, *Appl. Catal. B: Environ.* 2017, **204**, 486-496.
12. Y. Leng, G. Chen, A. J. Mendoza, T. B. Tighe, M. A. Hickner, C. Y. Wang, Solid-state water electrolysis with an alkaline membrane, *J. Am. Chem. Soc.* 2012, **134**, 9054-9057.
13. I. Vincent, A. Kruger, D. Bessarabov, Development of efficient membrane electrode assembly for low cost hydrogen production by anion exchange membrane electrolysis, *Int. J. Hydrogen Energy* 2017, **42**, 10752-10761.
14. G. Yang, J. Hao, J. Cheng, N. Zhang, G. He, F. Zhang, C. Hao, Hydroxide ion transfer in anion exchange membrane: A density functional theory study, *Int. J. Hydrogen Energy* 2016, **41**, 6877-6884.
15. X. Ren, S. C. Price, A. C. Jackson, N. Pomerantz, F. L. Beyer, Highly conductive anion exchange membrane for high power density fuel-cell performance, *ACS Appl. Mater. Interfaces* 2014, **6**, 13330-13333.
16. T. P. Pandey, H. N. Sarode, Y. Yang, Y. Yang, K. Vezzù, V. D. Noto, S. Seifert, D. M. Knauss, M. W. Liberatore, A. M. Herring, A highly hydroxide conductive, chemically stable anion exchange membrane,

- poly(2,6 dimethyl 1,4 phenylene oxide)-b-poly(vinyl benzyl trimethyl ammonium), for electrochemical applications, *J. Electrochem. Soc.* 2016, **163**, H513-H520.
17. C. C. Pavel, F. Cecconi, C. Emiliani, S. Santuccioli, A. Scaffidi, S. Catanorchi, M. Comotti, Highly efficient platinum group metal free based membrane-electrode assembly for anion exchange membrane water electrolysis, *Ang. Chem. Int. Ed. Engl.* 2014, **53**, 1378-1381.
 18. Y.-H. Fang, Z.-P. Liu, Tafel kinetics of electrocatalytic reactions: From experiment to first-principles, *ACS Catalysis* 2014, **4**, 4364-4376.
 19. E. C. M. Tse, A. A. Gewirth, Effect of temperature and pressure on the kinetics of the oxygen reduction reaction, *J. Phys. Chem. A* 2015, **119**, 1246-1255.
 20. X. Wu, K. Scott, A non-precious metal bifunctional oxygen electrode for alkaline anion exchange membrane cells, *J. Power Sources* 2012, **206**, 14-19.
 21. Y. Leng, G. Chen, A. J. Mendoza, T. B. Tighe, M. A. Hickner, C.-Y. Wang, Solid-state water electrolysis with an alkaline membrane, *J. Am. Chem. Soc.* 2012, **134**, 9054-9057.
 22. Z. Kang, J. Mo, G. Yang, S. T. Retterer, D. A. Cullen, T. J. Toops, J. B. Green Jr, M. M. Mench, F.-Y. Zhang, Investigation of thin/well-tunable liquid/gas diffusion layers exhibiting superior multifunctional performance in low-temperature electrolytic water splitting, *Energy Environ. Sci.* 2017, **10**, 166-175.
 23. S. Siracusano, V. Baglio, N. Van Dijk, L. Merlo, A.S. Aricò, Enhanced performance and durability of low catalyst loading PEM water electrolyser based on a short-side chain perfluorosulfonic ionomer, *Applied Energy* 2017, **192**, 477-489.

24. J. Ran, L. Wu, B. Wei, Y. Chen, T. Xu, Simultaneous enhancements of conductivity and stability for anion exchange membranes (AEMs) through precise structure design, *Sci. Rep.* 2014, **4**, 6486.
25. S. J. Paddison, K. S. Promislow, Device and materials modeling in PEM fuel cells, Springer, 2009.
26. G. Li, P. G. Pickup, Ionic Conductivity of PEMFC Electrodes: Effect of Nafion Loading, *J. Electrochem. Soc.* 2003, **150**, C745-C752.

Chapter 5. Graphitic carbon nitride-carbon nanofiber as oxygen evolution reaction catalyst in anion-exchange membrane water electrolyzer

5.1. Introduction

Graphitic carbon nitride (g-CN) is a material that consists of carbon and nitrogen atoms, organized in a graphite-like framework.¹ Recently, g-CN has been shown to have active as an electrochemical catalyst owing to its high content of N.²⁻¹⁰ Furthermore, various approaches to enhancing the catalytic activities of g-CN-based materials as alternatives to noble metals for OER and ORR have been developed.^{4-7,10} One such approach involves the addition of a metal to g-CN to improve its catalytic activity. Jiang et al.⁷ investigated g-CN-supported single-atom transition metals (Pt, Pd, Co, Ni, Cu) as OER catalysts. Among the transition metals examined, Co exhibited the most outstanding activity. Qiao et al.¹⁰ reported the fabrication of Co-g-CN/carbon nanotube (CNT) materials as electrocatalysts for OER and ORR. Another approach is based on the formation of g-CN/carbon composite nanomaterials to address the drawbacks associated with g-CN. Sun et al.⁶ investigated the possibility that a g-CN nanosheets/graphene composite could exhibit OER activity as a result of the presence of pyridinic N active sites. The authors showed that the introduction of graphene into g-CN resulted in a catalyst with good durability and high activity. Qiao et al.⁵ reported that a g-CN/CNT three-dimensional porous composite exhibits high OER activity owing to the enhanced mass transport caused by the presence of CNTs. Guo et al.¹¹ showed that the

combination of g-CN with graphene nanosheets produced a metal-free ORR catalyst. Previously, we have synthesized a g-CN/carbon nanofiber (CNF) composite (g-CN-CNF) using a facile preparing method and utilized it in the fabrication of a practical proton-exchange membrane fuel cell (PEMFC) and anion-exchange membrane fuel cell (AEMFC).¹² We confirmed that the g-CN-CNF catalyst exhibits high catalytic activity for ORR in alkaline media and high performance in practical fuel cells, demonstrating thus the feasibility of its application in practical electrochemical devices.

Recently, the application of OER catalysts in practical devices has been reported to evaluate their performance of real device rather than that of half-cell test, rotating disk electrode (RDE) method. For AEMWE, few studies about the application of OER catalyst in full-cell system have been reported. So far, Co-,¹³ Ni-,^{14,15} and Cu-^{16,17} based catalyst have been proposed as OER catalyst in AEMWE. Scott et al.¹³ proposed Li-doped Co₃O₄ as OER catalyst and evaluated its performance in AEMWE single cell, exhibiting the current density of 300 mA·cm⁻² at 2.05 V. Xing et al.¹⁴ introduced core-shell structured Ni-based hollow sphere in AEMWE single cell, and showed the high performance of 357.6 mA·cm⁻² at 1.8V. That is, the carbonaceous material as OER catalyst in AEMWE single cell needs to be developed.

In the present work, we synthesized a carbonaceous material, g-CN-CNF, as a bifunctional catalyst for oxygen electrocatalysis, and tested its activity toward both ORR and OER in alkaline media. Various synthetic parameters (heat treatment temperature, and content of CNF) were investigated to achieve optimum cell performance. Catalytic activity and durability measurements were conducted using the RDE method. In addition, the AEMWE was prepared to investigate the possibility of g-CN-CNF application in practical electrochemical device. AEMWE was fabricated and evaluated to examine the practical OER performance. To the

best of our knowledge, this work represents the first application of a carbonaceous material as OER catalyst in practical AEMWE.

5.2. Experimental section

5.2.1. Fabrication of g-CN-CNF catalyst

The modified preparation procedure employed for the synthesis of g-CN-CNF was based on our previous work.¹² Melamine (1 eq.) was suspended in dimethylformamide (DMF) and subsequently added to *N,N*-diisopropylethylamine (Sigma Aldrich Co., USA). Cyanuric chloride (1 eq.) was added dropwise and the mixture was subsequently stirred for 1 h at 0 °C. The temperature was increased to room temperature and the solution was stirred for additional 18 h. An additional quantity of cyanuric chloride (1 eq.) was added dropwise and the solution was stirred for 1 h at 0 °C. Subsequently, the temperature was increased to room temperature and the solution was stirred for 7 h. In order to increase the conductivity of the catalyst, the CNF (Carbon Nanomaterial Technology Co., Korea) was added dropwise to the solution. The mass ratio of CNF was approximately 30, 50, and 70 wt. % relative to total mass to examine the optimal content of CNF in g-CN-CNF. To remove any trace metal residues on the surface, the CNF was treated with acid (4 M H₂SO₄:4 M HNO₃, 3:1, v:v) for 7 h at 90 °C before its addition to the solution. The mixture was refluxed for 24 h at 150 °C under argon atmosphere. The precipitate was filtered and washed with ethanol. The prepared catalyst was dried using oven at 105 °C. For pyrolysis, the synthesized g-CN-CNF was heated to a certain temperature under an argon atmosphere for 7 h and maintained at the target level for 30 min. Three temperatures (700, 800, and 900 °C) were examined in order to determine the optimal temperature.

5.2.2. Physical characterizations of g-CN-CNFs

The synthesized g-CN was confirmed by examining the Fourier transform infrared (FT-IR) using FT-IR spectrophotometer (Nicolet 6700, Thermo Scientific, Germany). The morphology of g-CN-CNF catalyst was characterized by using

field-emission scanning electron microscope (FE-SEM; SUPRA 55VP, Carl Zeiss, Germany). X-ray diffraction (XRD) spectra of prepared catalysts were measured using X-ray diffractometer (D/MAX-2500/PC, Rigaku Co.). The element composition of g-CN-CNFs was evaluated using X-ray photonic spectroscopy (XPS, SIGMA PROBE, Thermo, UK). Raman spectra of prepared catalysts were obtained with a Raman spectrometer (LabRAM HV Evolution, Horiba, Japan). CHN elemental analyzer (Flash1112, Thermo Fisher Scientific, Germany) was used to observe the nitrogen content of catalysts. Nitrogen sorption isotherms of catalysts were measured using BET-Surface area analyzer (ASAP2000, Micromeritics, USA). Pore size distributions of catalyst layers with g-CN-CNF-800 and IrO₂ were analysed using by mercury porosimetry (MicroActive AutoPore V 9600, Micromeritics Co.)

5.2.3. Electrochemical characterization of g-CN-CNF

The half-cell experiments were performed with an Autolab potentiostat in the form of a three-electrode cell at 25 °C. We used glassy carbon electrode and saturated Ag/AgCl as the counter and the reference electrode, respectively. For the fabrication of the ink, 5 mg of the catalysts were mixed and sonicated with 30 µL of 5 wt. % Nafion ionomer and 700 µL of isopropanol. We loaded 20 µL of the ink onto a glassy carbon electrode. As standard materials, IrO₂ (Alfa Aesar Co., USA) were used. The densities of the loaded ink were 800 µg/cm² for g-CN-CNF materials and 400 µg/cm² for standard materials. The hydrogen oxidation reaction was performed to convert the measured potential to a reversible hydrogen electrode (RHE). During linear sweep voltammetry (LSV) for OER, the rotating disk electrode (RDE) was scanned at a rate of 10 mV/s in an O₂-saturated 0.1-M KOH solution at a rotating speed of 1600 rpm. OER LSV curves were iR-corrected. A collection efficiency of 0.37 and a ring voltage of 1.2 V versus RHE were used to

obtain electron transfer numbers and peroxide yields. Durability test for OER were performed in O₂-saturated electrolyte at a rotating speed of 1600 rpm using chronoamperometry with a voltage of 1.6 V versus RHE, respectively.

5.2.4. AEMWE Cell Test

In order to examine the OER activity of the synthesized catalyst, the AEMWE performance was evaluated. The single cell consists of a membrane-electrode assembly (MEA), gas diffusion layer (GDL), and bipolar plates. The MEA was fabricated using the catalyst-coated membrane (CCM) method with an active area of 5 cm². In the present work, Fumapem FAA-3-50 (FuMA-Tech Inc., Germany) was used as the anion-exchange membrane, and 40 wt. % Pt/C (Johnson Matthey Co. UK) with a loading of 0.4 mg·cm⁻² was used as the HER catalyst. The g-CN-CNF-800 and commercial IrO₂ (Alfa Aesar Co., USA) were used as the OER catalyst. The ionomer (Fumion, FuMA-Tech Inc., Germany) contents of anode and cathode were 20 and 30 wt. %, respectively. The cell temperature was set to 60 °C, and 1.0 M KOH solution was fed into the anode and cathode at a rate of 1 mL·min⁻¹.¹⁸ Before the operation, 1.0 M KOH solution was allowed to flow for 10 min to supply reactants in entire catalyst layer. The cell voltage was applied from 1.35 V to 2.15 V with an interval of 0.05 V to evaluate the cell performance. The electrochemical impedance spectroscopy (EIS, ZAHNER-elektrik GmbH & Co. KG, Germany) analysis was performed at a constant voltage of 1.9 V to characterize the ohmic and charge transfer resistances. The frequency ranged from 100 mHz to 100 kHz during this measurement.

5.3. Results and Discussion

5.3.1. Characterization of the synthesized g-CN-CNFs

The synthetic procedure for the preparation of the g-CN-CNF catalyst involved three main steps (Figure 5.1): (i) the fabrication of g-CN using cyanuric chloride and melamine via a stepwise synthesis, (ii) the addition of CNFs, which were treated with acid, to g-CN to increase the catalyst conductivity and prepare porous electrode, (iii) heat treatment (HT) of the resulting g-CN-CNF at 700, 800, or 900 °C under Ar atmosphere for pyrolysis. This process afforded different g-CN-CNF materials that allowed the optimal HT temperature to be determined. The g-CN-CNFs subjected to different HT temperatures are referred to as g-CN-CNF-T, where T presents the temperature (noHT, 700, 800, and 900 °C). Additionally, several g-CN-CNFs were prepared with different wt. % of CNFs (30, 50, and 70 wt. %) at the optimal HT temperature of 800 °C. The prepared catalysts are referred to as g-CN-CNF-Nwt, where N represents the wt. % content of CNFs (30, 50, and 70 wt. %)

As shown in the SEM image of g-CN (Figure 5.2a and b), the synthesized g-CN particles were agglomerated. The specific surface area of g-CN was determined to be $66.69 \text{ m}^2 \cdot \text{g}^{-1}$ using the Brunauer–Emmett–Teller (BET) method (Figure 5.3a). In addition, the average pore diameter was calculated to be approximately 8.7 nm via Barrett–Joyner–Halenda (BJH) adsorption (Figure 5.3b).

The SEM images (Figure 5.4a and b) showed that the g-CN-CNF was combined with g-CN and CNF. When compared to the g-CN particles shown in Figure 5.2a and b, the g-CN nanoparticles in the g-CN-CNF material were uniformly dispersed with CNF, indicating the successful deposition of g-CN on CNF. As displayed in Figure 5.4c, TEM also showed that the CNFs were surrounded by g-CN particles. EDS mapping (Figure 5.4d–g) confirmed the homogeneous distributions of C, N, and O atoms in g-CN-CNF, indicating that N

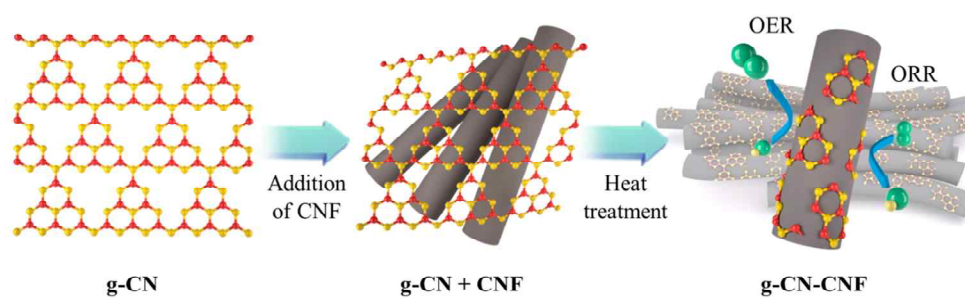


Figure 5.1 (a) Schematic diagram showing the preparation of the g-CN-CNF catalyst.

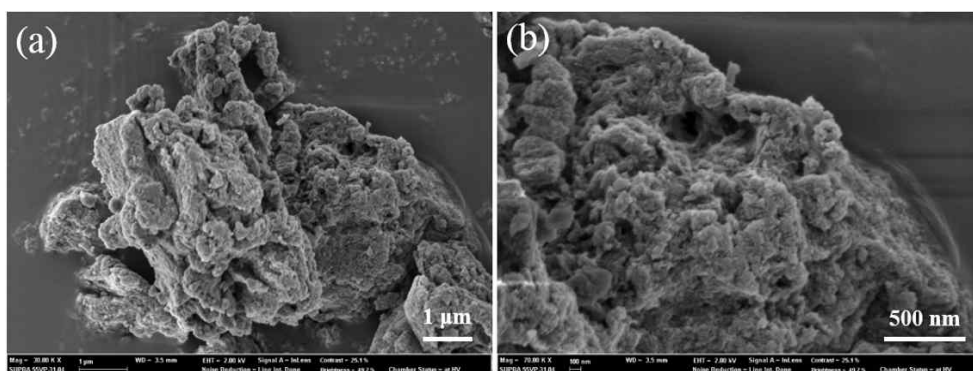


Figure 5.2 (a-b) SEM images of the synthesized g-CN.

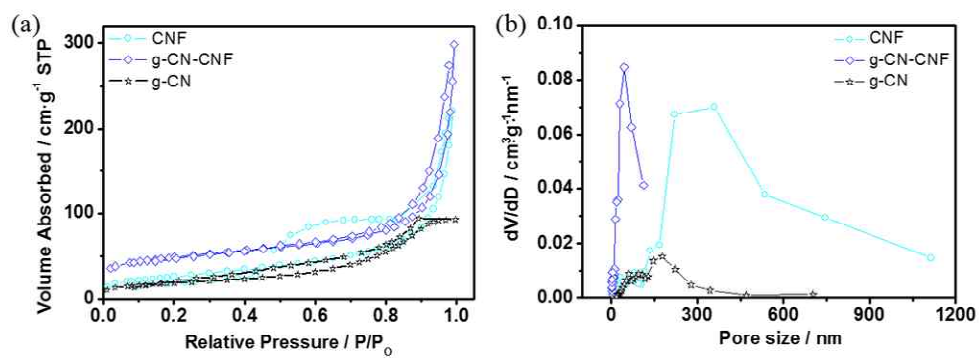


Figure 5.3 (a) nitrogen adsorption isotherms and (b) pore size distribution of g-CN, g-CN-CNF-800, and CNF.

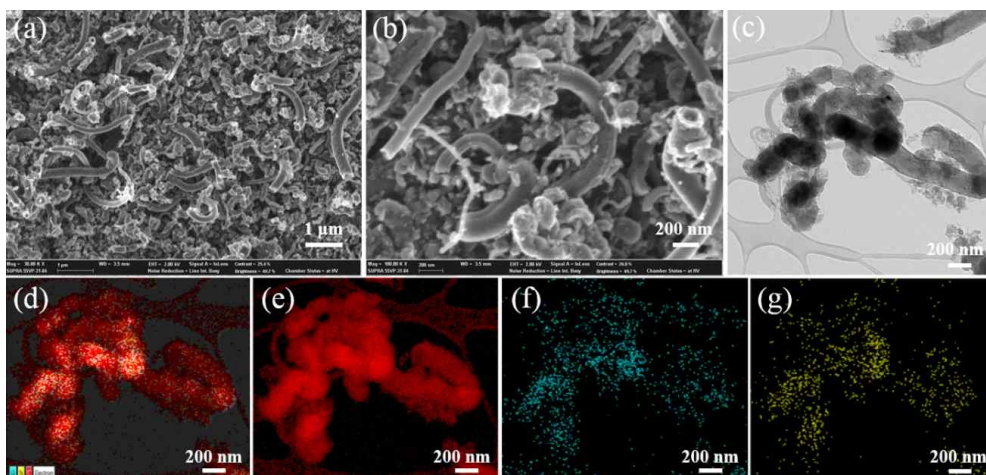


Figure 5.4 (a,b) SEM images, (c) TEM image, and (d–g) EDX elemental mapping of g-CN-CNF electrocatalyst: (e) C atom, (f) O atom, and (g) N atom.

atoms were uniformly dispersed in g-CN-CNF. The BET surface area of g-CN-CNF ($171.63 \text{ m}^2 \cdot \text{g}^{-1}$) was considerably higher than that of g-CN ($66.69 \text{ m}^2 \cdot \text{g}^{-1}$). Further, the N adsorption isotherm of g-CN-CNF exhibited a rapid increase in high relative pressure ($P/P_0 > 0.9$), suggesting the presence of secondary pores (Figure 5.3a).¹⁹ Moreover, the pore volume between 1.7 nm and 300 nm, and average pore diameter were determined using the BJH method to be $0.43 \text{ cm}^3 \cdot \text{g}^{-1}$ and 17 nm, respectively (Figure 5.3b).

Figure 5.5a shows the X-ray diffraction (XRD) patterns of the synthesized g-CN-CNF-T materials. These patterns show that as the HT temperature was increased from 700 to 900 °C, the peak intensity increased, indicating increased degree of graphitization. In addition, all the materials exhibited XRD patterns that were more similar to that of CNF, rather than the XRD pattern of g-CN. As shown in Figure 5.5b, the Raman spectra of all samples exhibited two distinct peaks at approximately 1345 and 1580 cm^{-1} . The D band observed at 1345 cm^{-1} is associated with disordered carbon, whereas the G band at 1580 cm^{-1} is related to the graphitization.²⁰ In addition to the XRD patterns, the Raman spectra showed that the I_D/I_G ratio of the g-CN-CNF-T materials decreased as the HT temperature was increased, leading to increased degree of graphitization.

X-ray photoelectron spectroscopy (XPS) was used to investigate the surface composition of each g-CN-CNF-T. The XPS survey spectra reveal the presence of C, N, and O (Figure 5.6). While g-CN-CNF-noHT exhibited four peaks for C–C (284.6 eV), C–O/C–N (285.7 eV), C=O/C=N (287.9 eV), and O–C=O (288.91 eV) species,^{21,22} other g-CN-CNF-T materials subjected to HT showed three distinct peaks, i.e., the peak arising from O–C=O species was missing (Figure 5.7)). In addition, the intensity of the peak associated with C–C species of g-CN-CNF-T increased as the HT temperature increased. These changes can be attributed to the decrease in the content of O atoms after pyrolysis. Furthermore, the presence

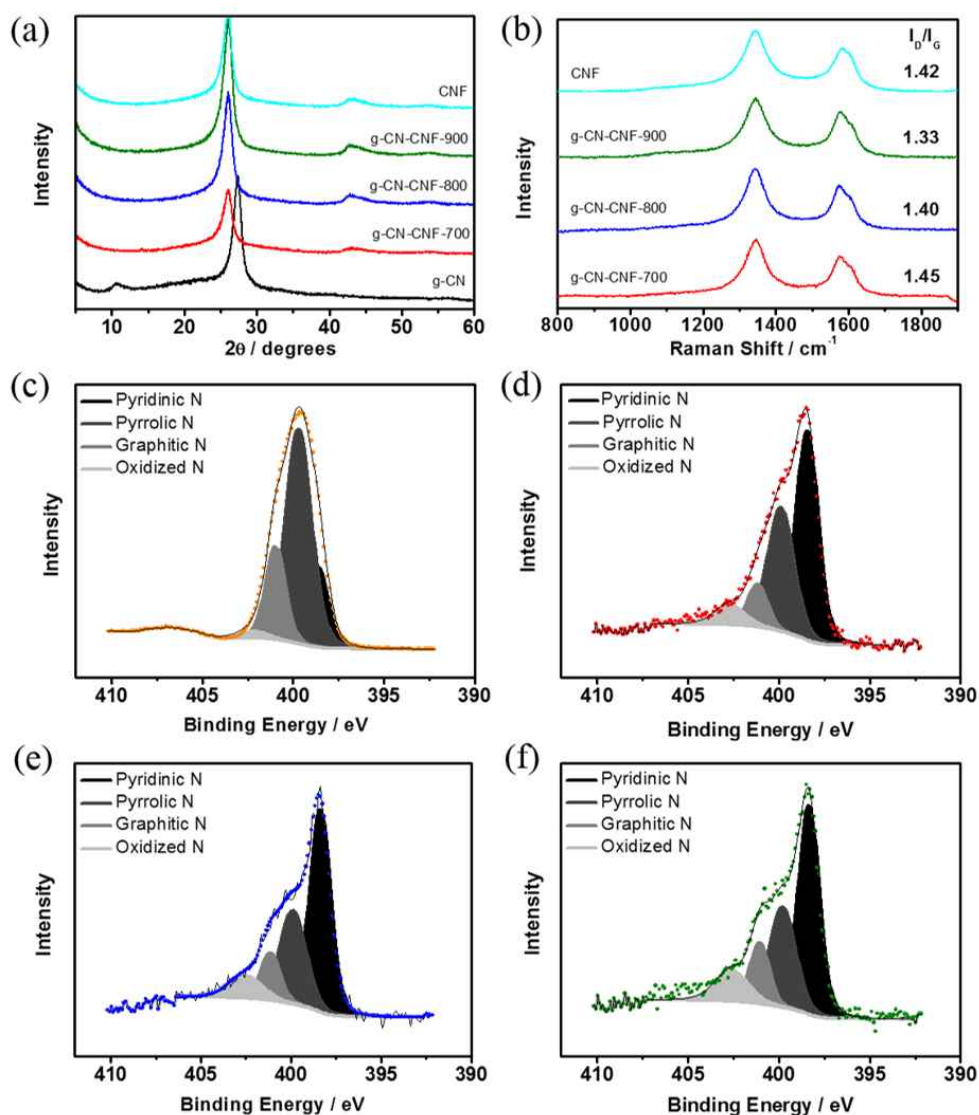


Figure 5.5 (a) XRD patterns of g-CN, g-CN-CNF-T and CNF materials. (b) Raman spectra of g-CN-CNF-T and CNF materials. N 1s XPS spectra of (c) g-CN-CNF-noHT, (d) g-CN-CNF-700, (e) g-CN-CNF-800, and (f) g-CN-CNF-900.

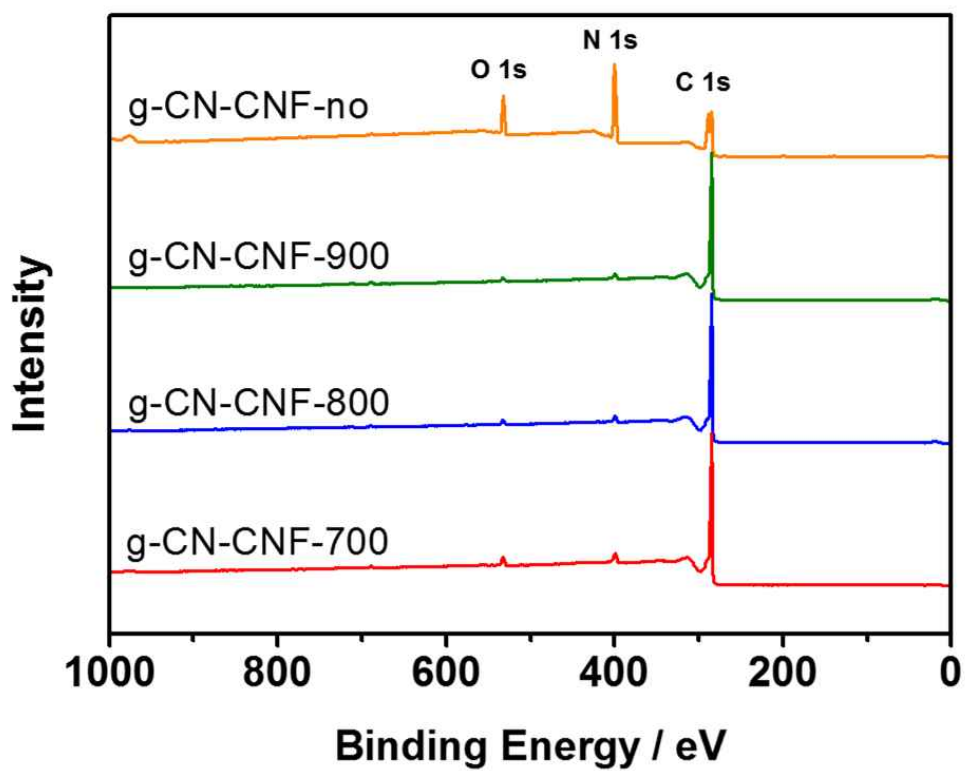


Figure 5.6 XPS survey spectra of g-CN-CNF-T materials.

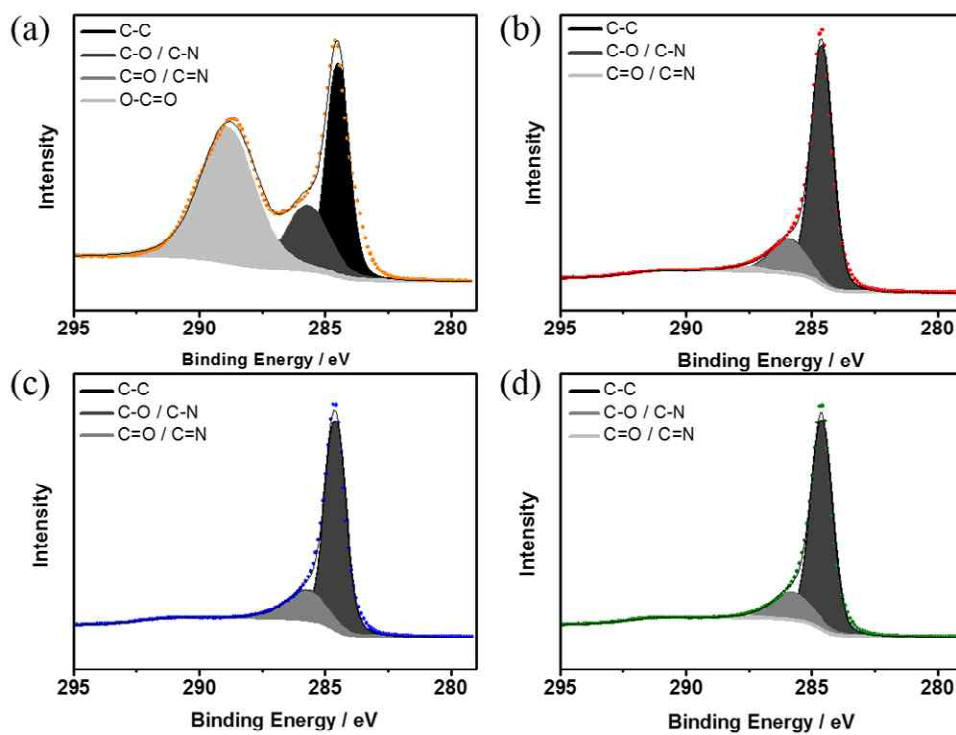


Figure 5.7 C 1s XPS spectra of g-CN-CNF-T materials ((a): g-CN-CNF-no, (b): g-CN-CNF-700, (c) g-CN-CNF-800, and (d) g-CN-CNF-900).

of the peaks related to the C–O/C–N and C=O/C=N species indicates that the N atoms from g-CN, which could serve as active sites for oxygen electrocatalysis, were successfully doped into CNF. Figure 5.4c–f shows the XPS spectra of N 1s of g-CN-CNF-Ts. The deconvolution of the peaks observed revealed four types of N configurations—pyridinic (398.6 eV), pyrrolic (399.89 eV), graphitic (401.1 eV), and oxidized N (402.6 eV). Unlike g-CN-CNF-noHT, which was mainly comprised of pyrrolic N, the other g-CN-CNF-T materials contained high contents of pyridinic N (Table 5.1). The atomic percentages of pyridinic N in the g-CN-CNF-T materials (noHT, 700, 800, and 900 °C) were 17.30, 49.79, 50.64, and 47.77%, respectively. The percentages of graphitic N for the same four g-CN-CNF-Ts were 17.30, 9.18, 11.28, and 12.85%, respectively. Among the g-CN-CNF-Ts examined, g-CN-CNF-800 displayed the largest percentage of nitrogen atoms in pyridinic and graphitic configurations (61.92%), which are known to be active sites for oxygen electrocatalysis.²³⁻²⁵ It is expected therefore that the increased levels of pyridinic and graphitic N will manifest in enhanced catalytic activity. In addition, the N contents of the g-CN-CNF-T materials were confirmed by elemental analysis (Table 5.1). The N contents of g-CN-CNF-noHT, g-CN-CNF-700, g-CN-CNF-800, and g-CN-CNF-900 were 21.74, 3.15, 2.53, and 0.9 wt. %, respectively. The N contents of g-CN-CNF-700, -800, and -900 (2–3 wt. %) were much lower than that of g-CN-CNF-noHT (21.74 wt. %), indicating that a significant proportion of N atoms was lost during the high temperature pyrolysis. As a result, the g-CN-CNF-700 has the largest N content among g-CN-CNF-T materials with HT.

The series of g-CN-CNF-Nwt materials (CNFs: 30, 50, and 70 wt. % of total mass) were characterized to examine the effect of the wt. % contents of g-CN and CNF (Figure 5.8 and 5.9). All the g-CN-CNF-T materials, which were discussed earlier on, were prepared using g-CN = 50 wt. % and CNF = 50 wt. %. To determine the optimal CNF content in g-CN-CNF, the g-CN-CNF-Nwt

Table 5.1. Summary of nitrogen properties, binding energy, content of g-CN-CNF-T materials.

		Pyridinic N	Pyrrolic N	Graphitic N	Oxidized N	N content
g-CN-CNF-no	Binding E (eV)	398.60	399.70	400.98	402.10	21.74
	Atomic ratio (at.%)	17.30	60.64	17.30	1.98	
g-CN-CNF-700	Binding E (eV)	398.44	399.89	401.17	402.70	3.15
	Atomic ratio (at.%)	49.79	34.60	9.18	6.43	
g-CN-CNF-800	Binding E (eV)	398.83	399.89	401.14	402.50	2.53
	Atomic ratio (at.%)	50.64	29.15	11.28	8.94	
g-CN-CNF-900	Binding E (eV)	398.35	399.80	401.06	402.60	2.56
	Atomic ratio (at.%)	47.77	28.24	12.85	11.14	

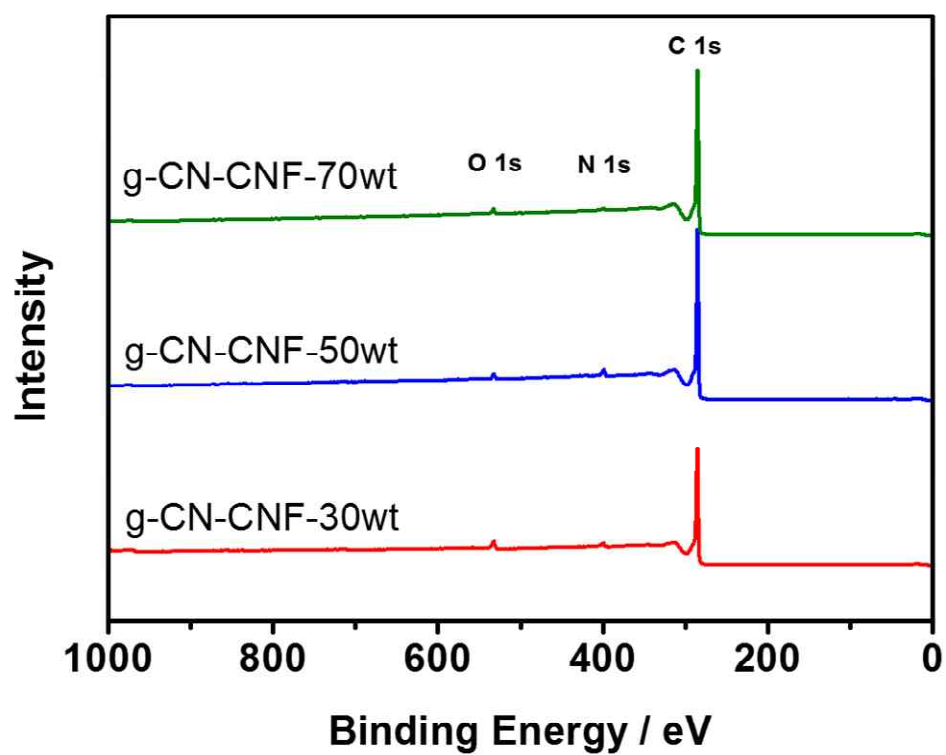


Figure 5.8 XPS survey spectra of g-CN-CNF-Nwt materials.

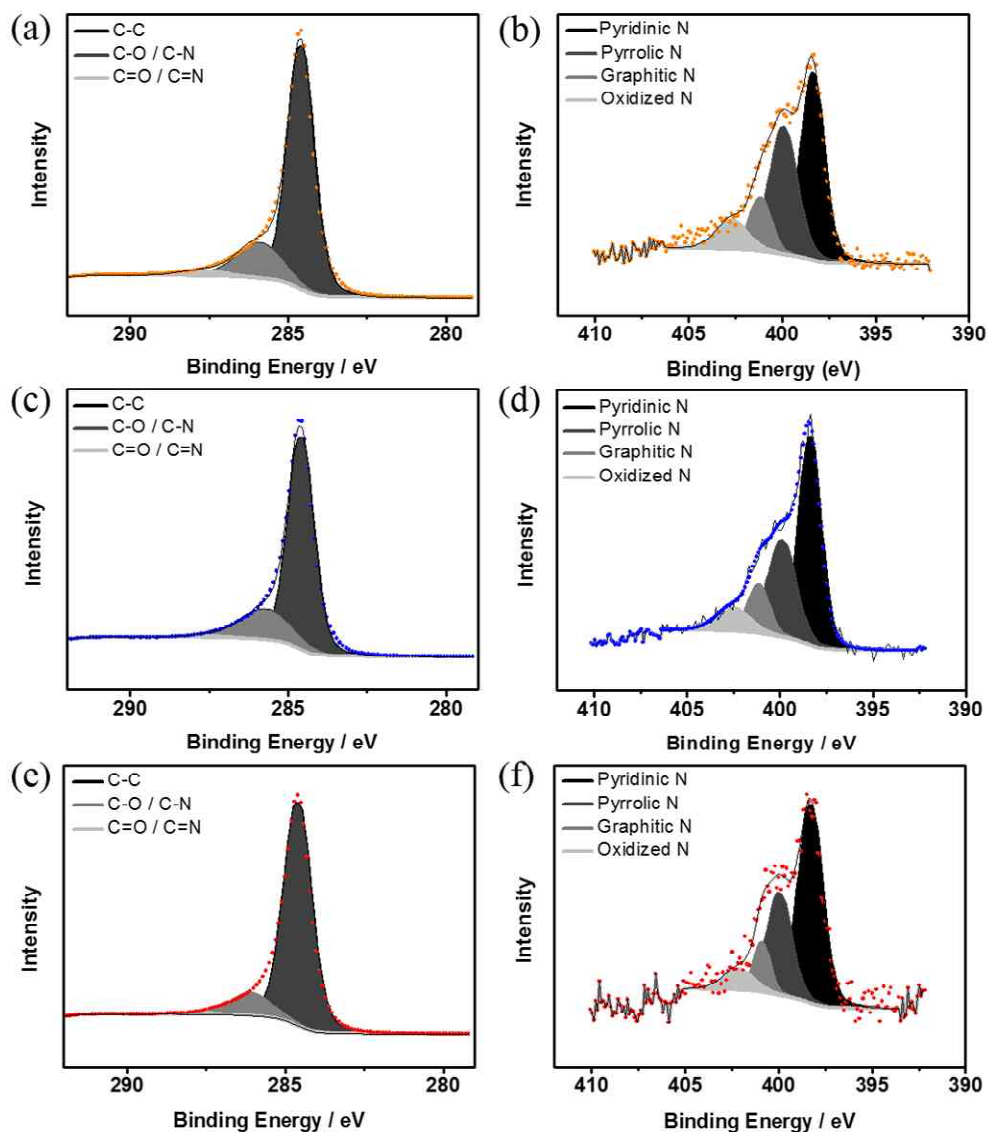


Figure 5.9 XPS spectra of g-CN-CNF-Nwt materials: (a) C 1s and (b) N 1s of g-CN-CNF-30wt, (c) C 1s and (d) N 1s of g-CN-CNF-50wt, (e) C 1s and (f) N 1s of g-CN-CNF-70wt.

materials were synthesized at the HT temperature of 800 °C. Table 5.2 summarizes the N contents, properties, and binding energies of the various g-CN-CNF-Nwt materials prepared. While the sum of the atomic percentage contents of pyridinic N and graphitic N increased as the wt. % of CNF (55.33, 61.92, and 64.21 at. %) increased, the total N content was the largest for the g-CN-CNF-50wt sample. The differences in the N contents of the g-CN-CNF-Nwt materials are ascribed to the changes in the quantities of g-CN and CNF employing during the preparation of the samples. During pyrolysis, the decomposed g-CNs were deposited on CNFs, serving thus as the N source in CNFs. When the wt. % content of g-CN was lower than that of CNF, the small amount of g-CN deposited resulted in reduced N content. By contrast, when the wt. % content of g-CN was higher than that of CNF, the insufficient amount of CNFs, which act as the substrate, resulted in the reduced overall N content in the sample. As a consequence, the sample prepared at 50 wt. % of both g-CN and CNFs was determined to be optimal for achieving high N content. The g-CN-CNF-50wt material has the highest contents of pyridinic and graphitic Ns of all the catalysts examined, and is thus expected to exhibit the highest catalytic activity. As shown in Figure 5.10a, the BET surface areas of g-CN-CNF-30wt, g-CN-CNF-50wt, and g-CN-CNF-70wt were 179.5, 171.6, and 156.56 m²·g⁻¹, respectively, indicating that the specific surface area decreased with increasing content of CNFs. By contrast, the pore volumes for these samples were determined to be 0.349, 0.433, and 0.354 cm³·g⁻¹. Taken together, the optimal content of CNFs is confirmed to be 50 wt. % based on the high N content and pore volume.

5.3.2. Electrochemical characterization of the synthesized g-CN-CNFs

The results of the electrochemical analyses using a half-cell configuration are summarized in Figure 5.11. Figure 5.11a shows the OER LSV curves of g-CN-CNF-T materials after iR compensation. As observed for the ORR performances,

Table 5.2. Summary of nitrogen properties, binding energy, content of g-CN-CNF-N wt materials.

		Pyridinic N	Pyrrolic N	Graphitic N	Oxidized N	N content
g-CN-CNF-30 wt	Binding E (eV)	398.36	399.93	401.16	402.70	1.98
	Atomic ratio (at.%)	43.77	35.15	11.56	9.53	
g-CN-CNF-50 wt	Binding E (eV)	398.83	399.89	401.14	402.50	2.53
	Atomic ratio (at.%)	50.64	29.15	11.28	8.94	
g-CN-CNF-70 wt	Binding E (eV)	398.29	399.96	400.90	402.14	1.05
	Atomic ratio (at.%)	54.9	28.16	9.31	7.64	

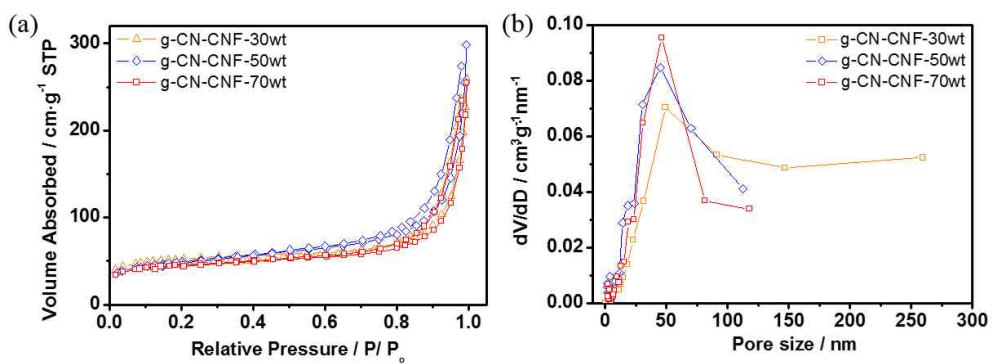


Figure 5.10 (a) nitrogen adsorption isotherms and (b) pore size distributions of g-CN-CNF-N wt materials.

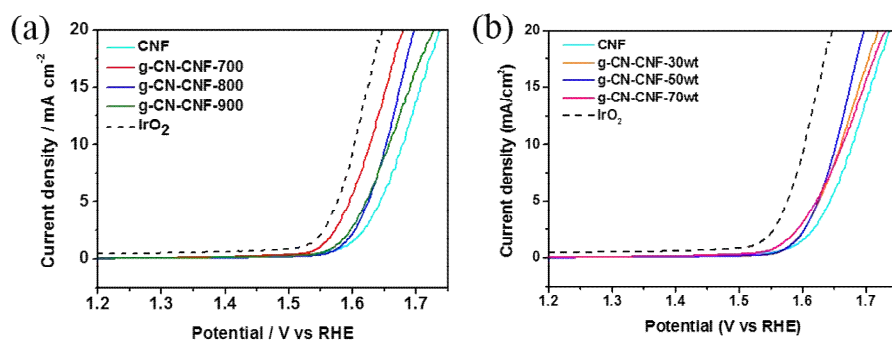


Figure 5.11 (a) Linear sweep voltammogram curves of (a) g-CN-CNF-T materials and (b) g-CN-CNF-Nwt materials for OER at a scanning rate of 10 mV/s with iR correction.

the g-CN-CNF-T materials exhibited improved OER activities when compared to that of CNF. The g-CN-CNF-700 displayed the best performance with an overpotential of 398 mV at $10 \text{ mA}\cdot\text{cm}^{-2}$, followed by an overpotential of 422 mV for g-CN-CNF-800 and 427 mV for g-CN-CNF-900. Among g-CN-CNF-T materials, g-CN-CNF-700 exhibited the best performance. However, g-CN-CNF-700 had low durability, indicating that g-CN-CNF-800 shows high and durable performance. The excellent catalytic performance of g-CN-CNF-800 is the result of adequate degree of graphitization and the presence of sufficient active sites, derived from abundant graphitic N and pyridinic N.^{27,29} In detail, pyridinic N can attract electrons from the surrounding carbon, thereby helping to adsorb hydroxyl ions and increasing OER performance.²⁸ Additionally, the catalytic activities of g-CN-CNF-Nwt materials were investigated to ascertain the optimum ratio of g-CN and CNF. As shown in Figure 5.11b, g-CN-CNF-50wt displayed better activity compared other g-CN-CNF-Nwt materials.

5.3.3. AEMWE performance

As illustrated in Figure 5.12a, an AEMWE with g-CN-CNF-800 as the anode and Pt/C as the cathode was fabricated to evaluate its OER activity for practical use. Figure 5.12b shows the changes in the cell performance of AEMWE as a function of the catalyst loading (2, 4, 6, and $8 \text{ mg}\cdot\text{cm}^{-2}$). As the catalyst loading was increased from 2 to 4, and subsequently to $6 \text{ mg}\cdot\text{cm}^{-2}$, the cell performance improved as a result of the increased number of active sites (223, 352, and $640 \text{ mA}\cdot\text{cm}^{-2}$, respectively). However, the cell performance at the highest catalyst loading ($8 \text{ mg}\cdot\text{cm}^{-2}$) decreased from $734 \text{ mA}\cdot\text{cm}^{-2}$ ($6 \text{ mg}\cdot\text{cm}^{-2}$) to $380 \text{ mA}\cdot\text{cm}^{-2}$ as a result of the thicker catalyst layer. Therefore, AEMWE exhibited the best performance, i.e., a current density of $734 \text{ mA}\cdot\text{cm}^{-2}$ at 1.9 V, when the catalyst loading was $6 \text{ mg}\cdot\text{cm}^{-2}$. Furthermore, g-CN-CNF-700 exhibited an outstanding

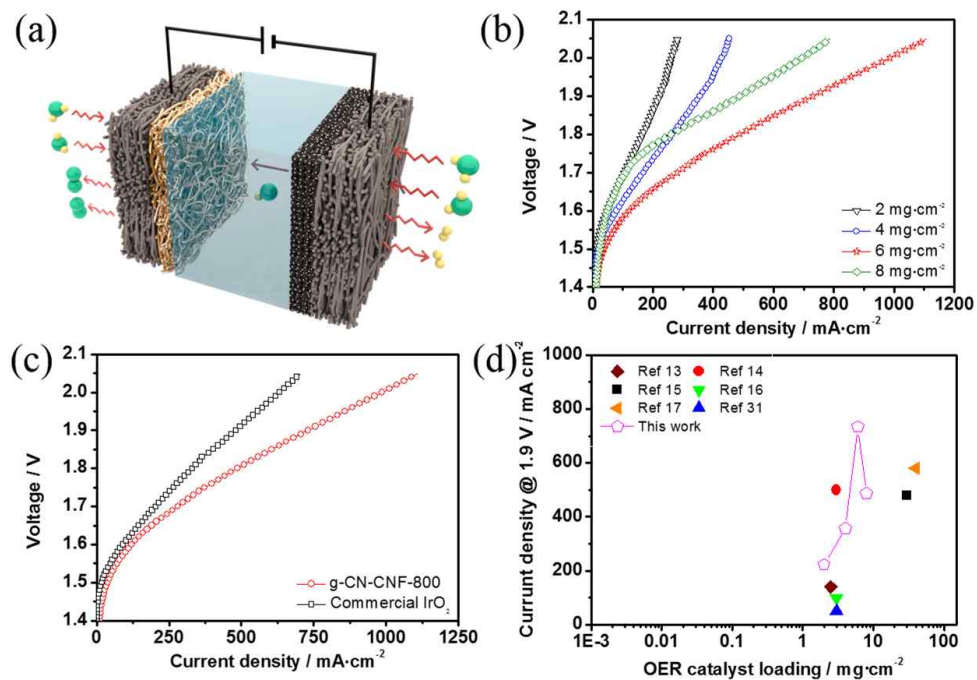


Figure 5.12 (a) Schematic diagram of AEMWE single cell with g-CN-CNF-800 as the anode catalyst. (b) Polarization curves obtained for AEMWE with different anode catalyst loadings. (c) Cell performance of AEMWE with g-CN-CNF-800 and commercial IrO₂. (d) The comparison of cell performances (current densities at 1.9 V) reported in literature^{13-17,31} and in this work (full symbols: non-noble metals as OER catalysts, open symbols: carbon-based material as OER catalyst).

performance when compared to commercial IrO₂ despite the fact that it is based on a carbonaceous material, and not a noble metal (Figure 5.12c). The current density of g-CN-CNF-800 at 1.9 V was 53% higher than that of IrO₂. Additionally, EIS was used to investigate the resistances in AEMWE.³⁰ As shown in Figure 5.13, the g-CN-CNF-800 showed similar ohmic resistance, and smaller charge transfer resistance when compared to IrO₂. Although the g-CN-CNF-800 was thicker (40 μm) than IrO₂ (2 μm), its high conductivity resulted in similar ohmic resistance. In addition, as shown in Figure 5.14, the portion of secondary pores in catalyst layer with g-CN-CNF was higher than that with IrO₂. The porosity of g-CN-CNF-800 was 78.54%, which is higher than IrO₂ (64.01%). The larger size and higher portion of the secondary pores in the g-CN-CNF catalyst layer resulted in improved interfacial reaction kinetics and mass transport, leading thus to a smaller charge transfer resistance despite the lower catalytic activity, as shown in Figure 5.15. Figure 5.12d compares the cell performances of several non-noble catalysts reported in the literature (full symbols)^{13-17,31} with the performance of the carbonaceous catalysts synthesized in this work (open symbols). To the best of our knowledge, this comparison suggests that g-CN-CNF-800 exhibits the highest performance for AEMWE reported to date. Furthermore, no studies have examined the possibility of applying carbonaceous materials as OER catalysts in practical AEMWEs. The results obtained here demonstrated that g-CN-CNF-800 displays notable potential as a catalyst for OER in practical AEMWE.

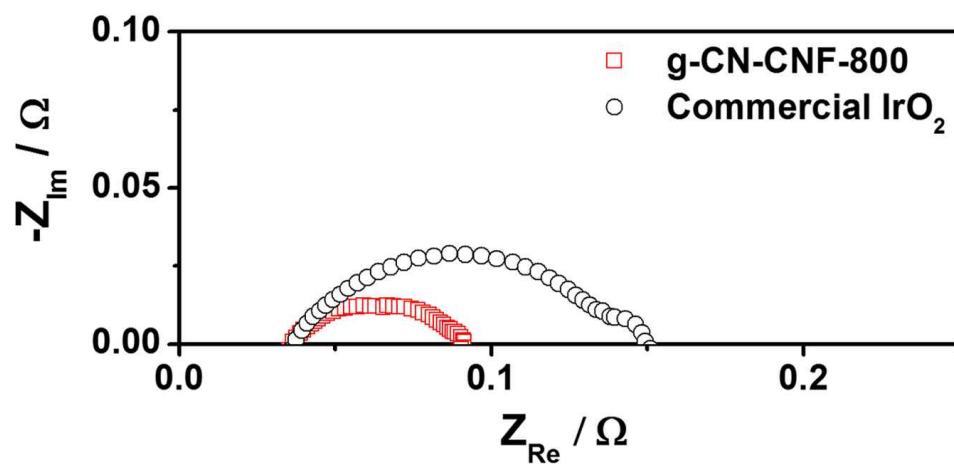


Figure 5.13 Nyquist plots of AEMWE with g-CN-CNF-800 and IrO_2 electrocatalyst obtained at 1.9 V.

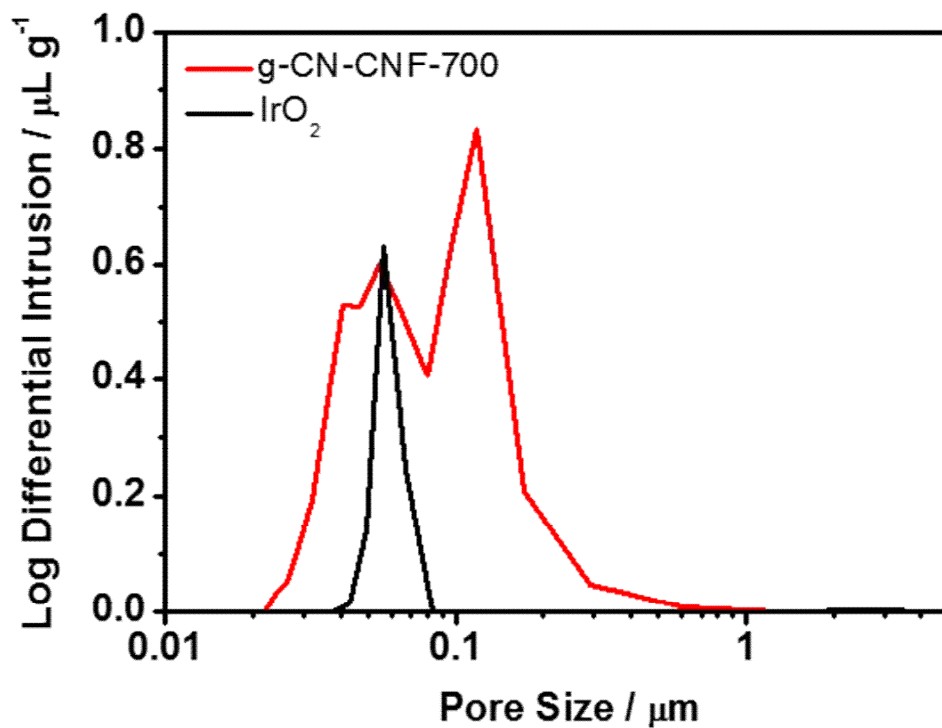


Figure 5.14 Pore size distributions of catalyst layers with g-CN-CNF-800 and IrO₂ measured by mercury porosimetry.

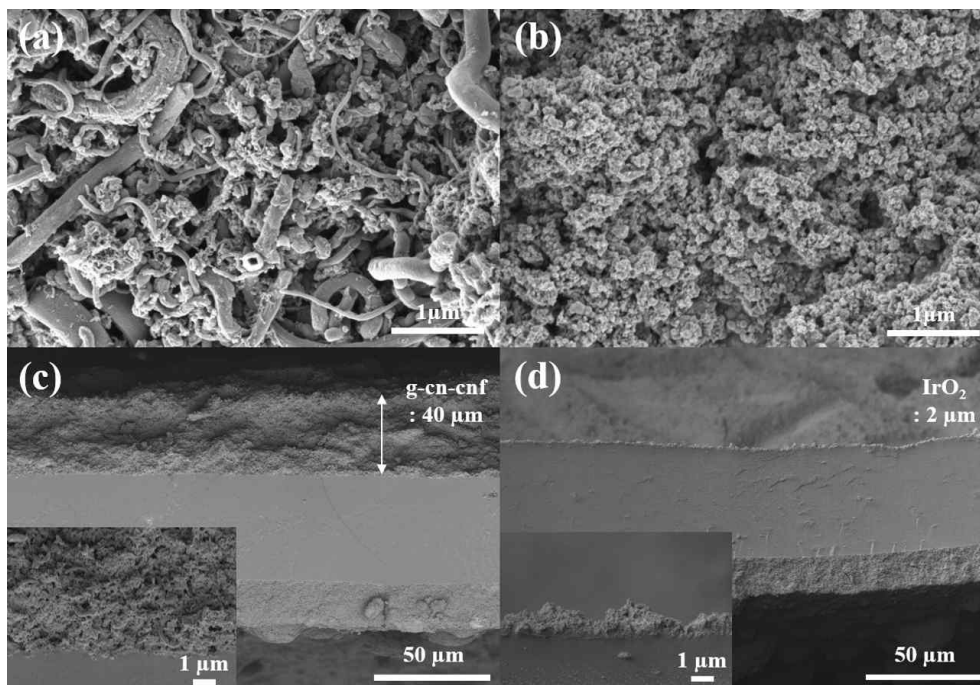


Figure 5.15 SEM images of MEA of AEMFCs: top view of catalyst layer of (a) g-CN-CNF-800 and (b) Pt/C. Cross-section view of MEA with (c) g-CN-CNF-800 and (d) Pt/C.

5.4. Conclusions

In this work, we successfully synthesized g-CN-CNF and evaluated its applicability as OER catalyst in AEMWE. The pyrolysis temperatures, and the ratios of g-CN to CNF were investigated to exhibit high catalyst activity. The optimized g-CN-CNF catalyst showed catalytic activity toward OER as a result of the synergistic effect of g-CN and CNF. The catalytic activity is ascribed to the formation of active sites by the decomposition of g-CN and the enhanced electrical conductivity of the substrate following the pyrolysis. The synthesized g-CN-CNF catalyst was applied to anode of AEMWE in order to examine their practical performance. Examination of AEMWE revealed high performance of $737 \text{ mA}\cdot\text{cm}^{-2}$ at 1.9 V, and represents the first application of a carbonaceous catalyst to practical AEMWE and the best performance reported to date. In addition, the AEMWE having g-CN-CNF exhibited higher performance and smaller charge-transfer resistance. It is the effect of higher portion of secondary pores in catalyst layer. Therefore, g-CN-CNF is a suitable candidate for the preparation of carbonaceous OER catalysts that can be applied in AEMWE

5.5. References

1. J. Zhu, P. Xiao, H. Li, S.A.C. Carabineiro, Graphitic carbon nitride: synthesis, properties, and applications in catalysis, *ACS Appl. Mater. Interfaces* 2014, **6**, 16449–16465.
2. A. Thomas, A. Fischer, F. Goettmann, M. Antonietti, J.-O. Müller, R. Schlögl, J.M. Carlsson, Graphitic carbon nitride materials: variation of structure and morphology and their use as metal-free catalysts, *J. Mater. Chem.* 2008, **18**, 4893–4908.
3. K. Kwon, Y. J. Sa, J. Y. Cheon, S. H. Joo, Ordered mesoporous carbon nitrides with graphitic frameworks as metal-free, highly durable, methanol-tolerant oxygen reduction catalysts in an acidic medium, *Langmuir* 2012, **28**, 991–996.
4. Y. Zheng, J. Liu, J. Liang, M. Jaroniec, S.Z. Qiao, Graphitic carbon nitride materials: controllable synthesis and applications in fuel cells and photocatalysis, *Energy Environ. Sci.* 2012, **5**, 6717–6731.
5. T. Y. Ma, S. Dai, M. Jaroniec, S. Z. Qiao, Graphitic carbon nitride nanosheet-carbon nanotube three-dimensional porous composites as high-performance oxygen evolution electrocatalysts, *Angew. Chem. Int. Ed.* 2014, **53**, 7281–7285.
6. J. Tian, Q. Liu, A. M. Asiri, K. A. Alamry, X. Sun, Ultrathin graphitic C₃N₄ nanosheets/graphene composites: efficient organic electrocatalyst for oxygen evolution reaction, *ChemSusChem* 2014, **7**, 2125–2130.
7. X. Li, P. Cui, W. Zhong, J. Li, X. Wang, Z. Wang, J. Jiang, Graphitic carbon nitride supported single-atom catalysts for efficient oxygen evolution reaction, *Chem. Commun.* 2016, **52**, 13233–13236.
8. N. Mansor, T. S. Miller, I. Dedigama, A. B. Jorge, J. Jia, V. Brázdová, C. Mattevi, C. Gibbs, D. Hodgson, P. R. Shearing, C. A. Howard, F. Corà, M.

- Shaffer, D. J. L. Brett, P. F. McMillan, Graphitic carbon nitride as a catalyst support in fuel cells and electrolyzers, *Electrochim. Acta* 2016, **222**, 44–57.
9. W.-J. Ong, L.-L. Tan, Y. H. Ng, S.-T. Yong, S.-P. Chai, Graphitic carbon nitride (g-C₃N₄)-based photocatalysts for artificial photosynthesis and environmental remediation: are we a step closer to achieving sustainability? *Chem. Rev.* 2016, **116**, 7159–7329.
 10. Y. Zheng, Y. Jiao, Y. Zhu, Q. Cai, A. Vasileff, L. H. Li, Y. Han, Y. Chen, S.-Z. Qiao, Molecule-level g-C₃N₄ coordinated transition metals as a new class of electrocatalysts for oxygen electrode reactions, *J. Am. Chem. Soc.* 2017, **139**, 3336–3339.
 11. K. Qiu, Z. X. Guo, Hierarchically porous graphene sheets and graphitic carbon nitride intercalated composites for enhanced oxygen reduction reaction, *J. Mater. Chem. A* 2014, **2**, 3209–3215.
 12. O.-H. Kim, Y.-H. Cho, D.Y. Chung, M.J. Kim, J.M. Yoo, J.E. Park, H. Choe, Y.-E. Sung, Facile and gram-scale synthesis of metal-free catalysts: toward realistic applications for fuel cells, *Sci. Rep.* 2015, **5**, 8376.
 13. X. Wu, K. Scott, A Li-doped Co₃O₄ oxygen evolution catalyst for non-precious metal alkaline anion exchange membrane water electrolyzers, *Int. J. Hydrogen Energy* 2013, **38**, 3123–3129.
 14. J. Chang, Q. Lv, G. Li, J. Ge, C. Liu, W. Xing, Core-shell structured Ni₁₂P₅/Ni₃(PO₄)₂ hollow spheres as difunctional and efficient electrocatalysts for overall water electrolysis, *Appl. Catal., B.* 2017, **204**, 486–496.
 15. I. Vincent, A. Kruger, D. Bessarabov, Development of efficient membrane electrode assembly for low cost hydrogen production by anion

- exchange membrane electrolysis, *Int. J. Hydrogen Energy* 2017, **42**, 10752–10761.
16. X. Wu, K. Scott, A polymethacrylate-based quaternary ammonium OH⁻ ionomer binder for non-precious metal alkaline anion exchange membrane water electrolyzers, *J. Power Sources* 2012, **214**, 124–129.
 17. L. Xiao, S. Zhang, J. Pan, C. Yang, M. He, L. Zhuang, J. Lu, First implementation of alkaline polymer electrolyte water electrolysis working only with pure water, *Energy Environ. Sci.* 2012, **5**, 7869–7871.
 18. M. K. Cho, H.-Y. Park, S. Choe, S. J. Yoo, J. Y. Kim, H.-J. Kim, D. Henkensmeier, S. Y. Lee, Y.-E. Sung, H. S. Park, J. H. Jang, Factors in electrode fabrication for performance enhancement of anion exchange membrane water electrolysis, *J. Power Sources* 2017, **347**, 283–290.
 19. C. Hu, L. Dai, Multifunctional carbon-based metal-free electrocatalysts for simultaneous oxygen reduction, oxygen evolution, and hydrogen evolution, *Adv. Mater.* 2017, **29**, 1604942.
 20. S. M. Hafiz, R. Ritikos, T. J. Whitcher, N. Md. Razib, D. C. S. Bien, N. Chanlek, H. Nakajima, T. Saisopa, P. Songsiriritthigul, N. M. Huang, S. A. Rahman, A practical carbon dioxide gas sensor using room-temperature hydrogen plasma reduced graphene oxide, *Sens. Actuators B Chem.* 2014, **193**, 692–700.
 21. X. Li, Y. Fang, X. Lin, M. Tian, X. An, Y. Fu, R. Li, J. Jin, J. Ma, MOF derived Co₃O₄ nanoparticles embedded in N-doped mesoporous carbon layer/MWCNT hybrids: extraordinary bi-functional electrocatalysts for OER and ORR, *J. Mater. Chem. A* 2015, **3**, 17392–17402.
 22. X. Liu, W. Zhou, L. Yang, L. Li, Z. Zhang, Y. Ke, S. Chen, Nitrogen and sulfur co-doped porous carbon derived from human hair as highly

- efficient metal-free electrocatalysts for hydrogen evolution reactions, *J. Mater. Chem. A* 2015, **3**, 8840–8846.
23. T. Sharifi, G. Hu, X. Jia, T. Wågberg, Formation of active sites for oxygen reduction reactions by transformation of nitrogen functionalities in nitrogen-doped carbon nanotubes, *ACS Nano* 2012, **6**, 8904–8912.
24. T. Xing, Y. Zheng, L. H. Li, B. C. C. Cowie, D. Gunzelmann, S. Z. Qiao, S. Huang, Y. Chen, Observation of active sites for oxygen reduction reaction on nitrogen-doped multilayer graphene, *ACS Nano* 2014, **8**, 6856–6862.
25. S. N. Faisal, E. Haque, N. Noorbehesht, W. Zhang, A. T. Harris, T. L. Church, A. I. Minett, Pyridinic and graphitic nitrogen-rich graphene for high-performance supercapacitors and metal-free bifunctional electrocatalysts for ORR and OER, *RSC Adv.* 2017, **7**, 17950–17958.
26. Q. Wang, L. Shang, R. Shi, X. Zhang, Y. Zhao, G. I. N. Waterhouse, L.-Z. Wu, C.-H. Tung, T. Zhang, NiFe layered double hydroxide nanoparticles on Co,N-codoped carbon nanoframes as efficient bifunctional catalysts for rechargeable zinc–air batteries, *Adv. Energy Mater.* 2017, **7**, 1700467.
27. J. Zhang, Z. Zhao, Z. Xia, L. Dai, A metal-free bifunctional electrocatalyst for oxygen reduction and oxygen evolution reactions, *Nature Nanotechnol.* 2015, **10**, 444–452.
28. C.-Y. Su, H. Cheng, W. Li, Z.-Q. Liu, N. Li, Z. Hou, F.-Q. Bai, H.-X. Zhang, T.-Y. Ma, Atomic modulation of FeCo–nitrogen–carbon bifunctional oxygen electrodes for rechargeable and flexible all-solid-state zinc-air battery, *Adv. Energy Mater.* 2017, **7**, 1602420.
29. B. Li, S.-W. Chien, X. Ge, J. Chai, X.-Y. Goh, K.-T. Nai, T. S. Andy Hor, Z. Liu, Y. Zong, Ni/NiO_x-decorated carbon nanofibers with enhanced

- oxygen evolution activity for rechargeable zinc-air batteries, *Materials Chemistry Frontiers*, 2017, **1**, 677-682.
30. J. S. Yi, T.-w. Song, Performance characterization of PEM fuel cells using AC impedance spectroscopy: I. model-based analysis, *J. Electrochem. Soc.* 2012, **160**, F141–F152.
31. Y.-C. Cao, X. Wu, K. Scott, A quaternary ammonium grafted poly vinyl benzyl chloride membrane for alkaline anion exchange membrane water electrolyzers with no-noble-metal catalysts, *Int. J. Hydrogen Energy* 2012, **37**, 9524–9528.

국문초록

수소는 에너지 밀도가 높고 이산화탄소 배출이 없는 환경 친화적이기 때문에 최근 청정에너지 원으로써 각광받고 있다. 수소 에너지원은 연료전지를 통해 전기를 생산해낼 수 있는 물질이다. 연료전지는 화학에너지를 전기에너지로 직접적으로 변환시키는 에너지 변환 장치로, 다양한 종류의 연료전지 중에 고분자 전해질 막 연료전지는 높은 성능과 낮은 구동조건등의 장점을 가지고 있어 많이 개발중인 장치이다. 이렇게 연료로 사용되는 수소는 수전해 장치를 통해 생산될 수 있다. 현재까지는 알칼리 수전해 장치가 널리 사용되고 있지만 다양한 단점을 가지고 있다. 단점을 보완하기 위해 효율이 높고 고순도의 수소를 생산할 수 있는 고분자 전해질 막 수전해가 대체 수전해 장치로 개발중인 장치이다.

연료전지나 수전해와 같은 전기화학 에너지 변환 장치는 구성요소들의 기공구조가 장치의 성능에 큰 영향을 끼치기 때문에 기공구조 개발이 중요하다. 장치 내에서 전기화학 반응에 참여하는 촉매는 광범위한 연구들을 통해 촉매 활성이 급격하게 향상되었다. 하지만, 개발된 촉매들의 실제 장치 성능은 크게 향상되지 못하여 연료전지나 수전해 개발에 걸림돌이 되고 있는 실정이다. 이는 장치 내의 반응물과 생성물의 물질 전달이 원활히 진행되지 않아 촉매의 반응을 방해하기 때문이다. 그러므로 구성요소 내의 기공구조 연구를 통해 촉매의 산소 환원 반응 또는 산소 발생 반응이 잘 일어나게 하는 적합한 기공구조를 찾는 것이 필요하다.

1 장에서는 연료 전지와 수전해 장치를 간략하게 소개한다. 연료 전지와 수전해의 종류, 특징, 구성 요소 및 성능에 대해 다루었다.

2 장에서는 고분자 전해질 막 연료 전지 (PEMFC)의 가스유로에 다공성 유동장을 적용하여 반응물과 생성물의 물질 전달을 향상시켰다.

가스 유로은 촉매 층에 반응물을 공급하고 생성된 물을 제거하는 중요한 구성요소이다. 최근 금속 폼이 기공구조로 이루어져 있어 다공성 가스 유로로 많이 적용되고 있다. 그러나 이 폼의 구조에 관한 연구에 관한 연구는 거의 보고되지 않았기 때문에 다양한 종류의 구리 폼을 적용하여 고성능을 나타내는 최적의 구조를 얻고자 연구를 진행하였다. 최적화된 구리 폼을 적용한 연료전지는 상압 조건에서 현재까지 보고된 최고 성능을 구현하였고, 기존에 사용되는 가스 유로에 비해 2 배의 성능 향상을 보였다. 이는 구리 폼 내부에서 생성된 압력과 물질 전달의 향상으로 인한 성능증가로 판단된다.

3 장에서는 역 오팔 (inverse-opal) 구조를 갖는 다공성 전극을 양성자 교환막 수전해 (PEMWE)에 적용하여 이리듐 옥사이드 촉매의 사용을 줄였다. 수전해에 사용되는 촉매는 매우 비싸기 때문에 수전해 장치 비용이 매우 비싸다. 이 비싼 촉매를 줄이기 위해서는 다공성 전극구조가 필요하다. 역 오팔 구조는 정렬되고 상호연결되어 있는 기공구조를 가지는 물질로, 표면적이 크기 때문에 기존 수전해보다 높은 성능을 나타내었다. 또한, 역 오팔 수전해는 촉매 로딩량이 매우 낮기 때문에 단위 질량 당 촉매의 성능이 현재까지 가장 높은 수치를 나타내었다. 이것은 역 오팔 구조가 촉매의 활용도를 높였기 때문으로 볼 수 있다.

4 장에서 음이온 교환막 수전해 (AEMWE) 내 막-전극 접합체의 매개 변수와 작동 조건을 최적화하여 고성능을 달성하였다. 양성자 교환막으로 구성된 PEMWE 와 달리, AEMWE 는 음이온 교환막 개발이 많이 이루어져 있지 않아 AEMWE 연구가 더딘 실정이다. 특히, 막-전극 접합체에 관한 보고된 연구는 거의 없다. 따라서 AEMWE 에서의 고효율 막-전극 접합체의 개발은 수전해 성능 향상에 매우 중요하다. 최적화 연구를 진행한 결과는 개발된 AEMWE 성능은 현재 보고된 다른 연구들 중 가장 높은 성능을 나타냄을 보여주었다.

5 장에서는 다공성 전극을 만들기 위해 탄소 질화물-탄소나노섬유 (g-CN-CNF) 복합체를 AEMWE 에 산소 발생 반응 촉매로 사용하였다. 탄소나노섬유를 도입함으로써 촉매층 내의 기공구조의 크기와 비율을 증가시킴으로써 다공성 전극을 제조하였다. g-CN-CNF 촉매는 N 과 C 로 이루어진 탄소 질화물과 탄소나노섬유를 혼합한 복합체로, 탄소 물질이 실제 AEMWE 에 적용된 최초의 연구이다. g-CN-CNF 는 피리딘과 그래피틱 질소 함량이 높기 때문에 삼전극 실험에서 산소 발생 반응의 높은 활성을 보였다. 또한, g-CN-CNF 촉매를 사용한 AEMWE 는 뛰어난 수전해 성능을 나타내었고, 이는 다공성 구조 적용에 따른 결과로 판단된다.

주요어: 고분자 전해질 막 연료전지, 양이온 교환막 수전해, 음이온 교환막 수전해, 기공구조.

학번: 2016-30224

List of publications (SCI)

1st or co-1st author

1. Sungjun Kim[†], Ji Eun Park[†], Wonchan Hwang, Yong-Hun Cho, Yung-Eun Sung, A hierarchical cathode catalyst layer architecture for improving the performance of direct methanol fuel cell, *Applied Catalysis B: Environmental* 2017, **209**, 91-97.
2. Ji Eun Park[†], Jongkoo Lim[†], Sungjun Kim, Insoo Choi, Chi-Yeong Ahn, Wonchan Hwang, Myung Su Lim, Yong-Hun Cho, Yung-Eun Sung, Enhancement of mass transport in fuel cells using three-dimensional graphene foam as flow field, *Electrochimica Acta* 2018, **265**, 488-496.
3. Ji Eun Park[†], Mi-Ju Kim[†], Myung Su Lim, Sun Young Kang, Jong Kwan Kim, Seung-Hyeon Oh, Min Her, Yong-Hun Cho, Yung-Eun Sung, Graphitic carbon nitride-carbon nanofiber as oxygen catalyst in anion-exchange membrane water electrolyzer and rechargeable metal-air cells, *Applied Catalysis B: Environmental* 2018, **237**, 140-148.
4. Ji Eun Park[†], Myung Su Lim[†], Jong Kwan Kim, Hee Ji Choi, Yung-Eun Sung, Yong-Hun Cho, "Optimization of cell components and operating conditions in primary and rechargeable zinc-air battery" *Journal of Industrial and Engineering Chemistry* 2019, **69**, 161-170.
5. Ji Eun Park[†], Sun Young Kang[†], Seung-Hyeon Oh, Jong Kwan Kim, Myung Su Lim, Chi-Yeong Ahn, Yong-Hun Cho, Yung-Eun Sung, High-performance anion-

exchange membrane water electrolysis, *Electrochimica Acta* 2019, **295**, 99-106.

6. Ji Eun Park, Sungjun Kim, Ok-Hee Kim, Chi-Yeong Ahn, Mi-Ju Kim, Sun Young Kang, Tae Il Jeon, Jae-Goo Shim, Dong Woog Lee, Ji Hyun Lee, Yong-Hun Cho, Yung-Eun Sung, Ultra-low loading of IrO₂ with an inverse-opal structure in polymer-exchange membrane water electrolysis, *Nano Energy* 2019, **58**, 158-166.

7. Mi-Ju Kim[†], Ji Eun Park[†], Sungjun Kim, Myung Su Lim, Aihua Jin, Ok-Hee Kim, Min Jeong Kim, Kug-Seung Lee, Jinsoo Kim, Seung-Soo Kim, Yong-Hun Cho, Yung-Eun Sung, Biomass-derived air cathode materials: Pore-controlled S, N-co-doped carbon for fuel cells and metal-air batteries, *ACS Catalysis* 2019, **9**, 3389-3398.

8. Ji Eun Park[†], Hyunjoon Lee[†], Seung-Hyeon Oh, Sun Young Kang, Insoo Choi, Yong-Hun Cho, Yung-Eun Sung, Electrodeposited mesh-type dimensionally stable anode for oxygen evolution reaction in acidic and alkaline media, *Chemical Engineering Science* 2019, **206**, 424-431.

9. Ji Eun Park[†], Wonchan Hwang[†], Myung Su Lim, Sungjun Kim, Chi-Yeong Ahn, Ok-Hee Kim, Jae-Goo Shim, Dong Woog Lee, Ji Hyun Lee, Yong-Hun Cho, Yung-Eun Sung, Achieving breakthrough performance caused by optimized metal foam flow field in fuel cells, *International Journal of Hydrogen Energy* 2019, In press.

Co-author

1. Ok-Hee Kim, Yong-Hun Cho, Dong Young Chung, Min Jeong Kim, Ji Mun Yoo, Ji Eun Park, Heeman Choe & Yung-Eun Sung, Facile and Gram-scale Synthesis of Metal-free Catalysts: Toward Realistic Applications for Fuel Cells, *Scientific Reports* 2015, **5**, 8376.
2. Chi-Yeong Ahn, Myung Su Lim, Wonchan Hwang, Sungjun Kim, Ji Eun Park, Jongkoo Lim, Insoo Choi, Yong-Hun Cho, Yung-Eun Sung, Effect of Porous Metal Flow Field in Polymer Electrolyte Membrane Fuel Cell under Pressurized Condition, *Fuel Cells* 2017, **17**, 652-661.
3. Chi-Yeong Ahn, Wonchan Hwang, Hyunjoon Lee, Sungjun Kim, Ji Eun Park, Ok-Hee Kim, Min Her, Yong-Hun Cho, Yung-Eun Sung, Effect of N-doped carbon coatings on the durability of highly loaded platinum and alloy catalysts with different carbon supports for polymer electrolyte membrane fuel cells, *International Journal of Hydrogen Energy* 2018, **43**, 10070-10081.
4. Mihwa Choi, Jong Kwan Kim, Jungsuk Kim, Seugran Yang, Ji Eun Park, Ok-Hee Kim, Yong-Hun Cho, PtRu/C catalyst slurry preparation for large-scale decal transfer with high performance of proton exchange membrane fuel cells, *RSC Advances* 2018, **63**, 36313-36322.